

MODELLING ICE FABRIC EVOLUTION AND ITS EFFECT ON VISCOUS ANISOTROPY

DANIEL HARRY MARK RICHARDS

Supervisors:

Dr. Sam Pegler
Prof. Sandra Piazzolo
Dr. Oliver Harlen

*A thesis submitted in accordance with the requirements
for the degree of Doctor of Philosophy*

THE UNIVERSITY OF LEEDS
Centre for Doctoral Training in Fluid Dynamics
School of Computing

November 2021

INTELLECTUAL PROPERTY

The candidate confirms that the work submitted is his own, except where work which has formed part of jointly authored publications has been included. The contribution of the candidate and the other authors to this work has been explicitly indicated below. The candidate confirms that appropriate credit has been given within the thesis where reference has been made to the work of others.

During this PhD I have published one paper entitled *The evolution of ice fabrics: A continuum modelling approach validated against laboratory experiments* (Richards et al., 2021b) published in February 2021 in *Earth and Planetary Science Letters*. I was the first author for this paper, with Samuel S. Pegler, Sandra Piazzolo and Oliver G. Harlen as co-authors. I was responsible for the manuscript, figures and numerical code and analysis with the other authors providing supervision and editing. Further anonymous reviewers provided helpful suggestions as well. I also have a paper in open review entitled *Ice fabrics in two-dimensional flows: beyond pure and simple shear* (Richards et al., 2021a) in *The Cryosphere*. I was the first author for this submission, with Samuel S. Pegler and Sandra Piazzolo as co-authors. I was responsible for writing the manuscript, numerical code, producing the figures and performing the analysis with the other authors providing supervision and editing. Further Maurine Montagnat, Fabien Gillet-Chaulet and an anonymous reviewer provided helpful suggestions as well. Both of these papers have been extensively used in this thesis.

In chapter 2, section 2.1.1 is based on work from section 1. of Richards et al. (2021b), as well as some work from Richards et al. (2021a). Furthermore, sections 2.1.2 and 2.1.3 are based on work from Richards et al. (2021a). section 2.2.1 is includes some work from both Richards et al. (2021a,b).

Chapter 3 is based almost entirely on Richards et al. (2021b), with the exception of extensions, particularly in section 3.3. Furthermore section 3.2 is taken from Richards et al. (2021a).

Chapter 4 is based entirely on Richards et al. (2021a), with parts taken out to avoid repetition.

Chapter 5 is written as a draft for a scientific manuscript to be submitted to *Cryosphere* or a similar international journal and has been developed in collaboration with my supervisors. As with the

work in Richards et al. (2021a,b) I have been responsible for writing the manuscript, producing the figures and numerical code, with Sandra Piazzolo and Sam Pegler providing supervision and editing.

This copy has been supplied on the understanding that it is copyright material and that no quotation from the thesis may be published without proper acknowledgement.

The right of Daniel Harry Mark Richards to be identified as Author of this work has been asserted by Daniel Harry Mark Richards in accordance with the Copyright, Designs and Patents Act 1988.

ACKNOWLEDGMENTS

I wouldn't have been able to accomplish this thesis without the support of so many people. Firstly I wish to thank my supervisors Sam Pegler, Sandra Piazzolo and Oliver Harlen for countless meetings, advice and encouragement. Dave Prior provided us with many interesting discussions, as well as the data which was key for the work in chapter 3. I also wish to thank the anonymous reviewers for Richards et al. (2021b) and Maurine Montagnat and Fabien Gillet-Chaulet and another anonymous reviewer for Richards et al. (2021a), for their contribution to significantly improving these papers, which form a significant part of this thesis. This work was funded by the UK Engineering and Physical Sciences Research Council (EPSRC) grant EP/L01615X/1 for the University of Leeds centre for doctoral training in fluid dynamics.

Outside of work, I wish to thank my partner Katrina for her support, encouragement and kindness while I have been working so hard on this. Thanks also to the people at Harnham Buddhist monastery, both residents and visitors, for without my frequent visits to take breaks from work, this thesis would have been much less manageable. I also wish to thank my friend Hassan, without whom I may never have started this PhD. Finally I wish to thank my parents for their years of care and love.

ABSTRACT

The loss of ice from Antarctica and Greenland is the main source of uncertainty for sea-level rise predictions under a warming climate. Ice fabrics - the distribution of crystal orientations within a polycrystal - are key for understanding the dynamics of ice. Understanding ice fabrics enables us to infer processes occurring within ice sheets. In addition, ice fabrics can cause the flow rate to vary by a factor of 9 in different directions. Despite this, it is still a challenge to model ice fabrics both accurately and efficiently. I develop the first fully constrained continuum model for fabric evolution which agrees with experimental results and has only temperature and velocity gradient as inputs, with low computational cost. Using this model I explore fabrics generated across a spectrum of two-dimensional deformations and temperatures. Results show that intermediate deformation regimes between pure and simple shear result in a smooth transition between a fabric characterised by a cone-shape and a secondary cluster pattern. Highly-rotational deformation regimes produce a weak girdle fabric. I also predict fabrics within an ice stream and compare results to measured ice fabrics from cores at the East Greenland Ice Core Project ([EGRIP](#)) site by tracing the flow path upstream using satellite data. This approach correctly predicts the fabric pattern at [EGRIP](#) - a girdle/horizontal maxima perpendicular to the flow. The results also provide insights into properties deep within the ice sheet such as the level of basal slip. In summary, the fabric model and its applications presented in this thesis enable prediction of ice fabrics much more accurately and easily than previously. Due to its numerical efficiency the developed and tested fabric evolution model presented in this work can now be coupled to large-scale ice-sheet models and provide a reliable basis for estimating the effect of viscous anisotropy.

CONTENTS

1	INTRODUCTION	1
1.1	Research questions	2
1.2	Thesis outline	3
2	BACKGROUND	5
2.1	Ice microstructure	5
2.1.1	Processes affecting fabric evolution	5
2.1.2	Observed fabrics	10
2.1.3	Fabric patterns	11
2.2	Modelling ice	13
2.2.1	Overview of modelling approaches	13
2.2.2	Anisotropy and the flow of ice	14
2.2.3	Mathematical representations of the fabric	19
2.2.4	Fabric evolution	21
3	THE EVOLUTION OF ICE FABRICS: A CONTINUUM MODELLING APPROACH VALIDATED AGAINST LABORATORY EXPERIMENTS	27
3.1	Introduction	28
3.2	Model details	29
3.2.1	Evolution equation	29
3.2.2	Non-dimensionalisation	30
3.3	Spectral method	31
3.4	Results	33
3.4.1	General forms of the fabric	33
3.4.2	Strain-rate dependence	35
3.4.3	Inversion for parameters in simple shear	37
3.4.4	Extrapolation to compression	39
3.5	Discussion	42
3.5.1	General model behaviour	42
3.5.2	Prediction of strain-rate dependence	45
3.5.3	Comparison with other models	48
3.5.4	Future Applications	48
3.6	Conclusions	49
4	ICE FABRICS IN TWO-DIMENSIONAL DEFORMATIONS: BEYOND PURE AND SIMPLE SHEAR	51
4.1	Introduction	52
4.2	Background	52

4.2.1	Experiments in intermediate deformations	52
4.2.2	Classifying flow regimes	53
4.2.3	Open questions addressed here	57
4.3	Methods	57
4.3.1	Non-dimensionalisation	59
4.3.2	Pole figure and cross section representation	59
4.4	Results	61
4.4.1	General fabric evolution: dependence on temperature and vorticity number	61
4.4.2	Fabric regime diagrams for cluster angle and fabric type	63
4.4.3	Analysis of fabric evolution timescales	70
4.5	Discussion	72
4.5.1	Fabric patterns across deformation regime and temperature space	72
4.5.2	Finite strains required for fabric evolution	73
4.5.3	Consequences for ice core interpretation	74
4.5.4	Implications for ice flow properties and modelling	75
4.6	Conclusions	77
5	NUMERICAL MODELLING OF ICE STREAM FABRICS: IMPLICATIONS FOR RECRYSTALLIZATION PROCESSES AND BASAL SLIP CONDITIONS	79
5.1	Introduction	79
5.2	Background	81
5.2.1	Shallow ice and shallow shelf approximations	81
5.2.2	The EGRIP site	82
5.3	Methods	86
5.3.1	Deformation history	86
5.3.2	Temperature history	88
5.3.3	Dimensional form of SpecCAF	88
5.4	Results	88
5.4.1	The effect of slip at the base of the ice sheet on fabric development throughout an ice stream	89
5.4.2	Strain-rate dependence of rotational recrystallization	93
5.5	Discussion	94
5.5.1	Girdle & horizontal maxima perpendicular to the flow	94
5.5.2	Oscillation in eigenvalues	95

5.5.3	Fabric strength & rotational recrystallization	95
5.5.4	The importance of basal slip for the flow of NEGIS	96
5.5.5	Timescales for fabrics to adjust to new deformations	97
5.5.6	Deformation mechanisms in ice stream flow	98
5.6	Conclusions	99
6	ONGOING AND FUTURE WORK	101
6.1	Ongoing work	101
6.1.1	Numerical method	102
6.1.2	Preliminary Results	104
6.2	Future work	105
7	DISCUSSION AND CONCLUSIONS	109
7.1	General discussion	109
7.2	Conclusions	116
A	SPHERICAL HARMONICS	119
A.1	Using the spherical harmonics to solve partial differential equations	120
A.1.1	Relationship between spherical harmonics and orientation tensors	122
B	NUMERICS AND CONSTRAINING OF SPECCAF	123
B.1	Number of harmonics	123
B.2	Experimental data used in comparison	123
C	PARAMETER SENSITIVITY STUDY	127
	BIBLIOGRAPHY	139

LIST OF FIGURES

- Figure 2.1 Image from Faria et al. (2014). Ice 1h. Red represents oxygen, white hydrogen. The hexagonal symmetry is shown by the yellow dashed line. The top view is along the c -axis, whereas the bottom view is along the a -axis. 6
- Figure 2.2 Sketch of the primary slip systems in ice, taken from Placidi (2005). The figure shows the hexagonal lattice structure and the c -axis. 6
- Figure 2.3 Diagram showing the four processes that can affect the ice fabric. An illustration of the mechanism on the microstructure, as well as the resulting effect on a pole figure of orientation mass distributions is shown for each one. (a) Under basal slip deformation, the c -axis rotates towards the axis of compression. In the pole figure for this case the cluster of c -axes at θ_1 also move towards the compression axis. (b) Rigid body rotation: any vorticity in the flow acts to rotate the crystallites and their c -axes around the axis of rotation. (c) Rotational recrystallization: $n_{1,2,3}$ represent grains with their orientation illustrated by the direction of hatching. Sub grains form at the boundaries between larger grains with intermediate orientations. In the pole figure, this translates to a diffusion of high intensity clusters of orientation towards $n_{1,2,3}$. (d) Migration recrystallization: the grain with a lower dislocation density, with orientation n_1 , migrates into the grain with a higher dislocation density. In the pole figure, the mass fraction of c -axes towards n_1 increases and the mass fraction towards n_2 decreases. 8

- Figure 2.4 Illustration showing common fabrics or CPOs which develop in ice, illustrated by their pole figures, as well as the deformation regime and temperature they typically occur at. The pole figures show the distribution of c -axis orientations, with the compression axis at the centre. (a) shows a single-maximum fabric, produced in unconfined compression or simple shear at low temperatures (Qi et al., 2019). (b) shows a cone-shape fabric, produced in unconfined compression at higher temperatures, when grain-boundary migration is active (Paterson, 1999). This can also be considered a girdle fabric when the cone-angle approaches 90° . (c) shows a double maxima fabric produced in confined compression (pure shear) (Budd et al., 2013). (d) shows a single-maximum with a secondary cluster, produced in simple shear at higher temperatures (Kamb, 1972; Qi et al., 2019). The normal to the shear plane is at the centre of this pole figure. (e) shows a girdle fabric, expected to be produced in unconfined extension but not performed in the laboratory. The arrows show the extension direction. 12
- Figure 2.5 Plot of the enhancement factor $\hat{E}(\mathcal{D})$ in the CAFFE model, with $E_{max} = 10$ and $E_{min} = 0.1$ 19
- Figure 2.6 Schematic of orientation space. Each point on the unit sphere represents a specific orientation n 20

Figure 3.1 Comparison of the pole-figures produced by the model, compared to sketches of expected pole figures, based on experimental observations and ice core samples (Paterson, 1999). Each row represents a different deformation. Comparison between the expected sketch and the model are presented for both no migration recrystallization, ($\tilde{\beta} = 0$), and with migration recrystallization, for the illustrative case of $\tilde{\beta} = 2$. Other parameter values chosen were $\tilde{\lambda} = 0.05$ and $\iota = 1$. The model pole figures are plotted at true strain $\gamma = 0.7$. The final column shows a plot of the deformability, \mathcal{D}^* from eq. (2.33), which controls migration recrystallization. 34

Figure 3.2 This figure shows the strain-rate dependence of experimental fabrics in uniaxial (unconfined) compression. The plots shows two measures of fabric concentration for this flow field, λ_1 , the largest eigenvalue of $\mathbf{A}^{(2)}$ (a), and \hat{f} (b), against experimental data (Craw et al., 2018; Piazzolo et al., 2013). For each data set, in order to identify the strain-rate dependence, the values have been sorted into bins with roughly equal temperature ($\pm 1^\circ\text{C}$) and strain (± 0.025). The hats that indicate the values have been normalised against the value at $\dot{\gamma} = 10^{-5}$ in order to collapse different bins onto a single curve. A fit is also shown along with the R^2 value of the fit. 36

Figure 3.3 Plot of the parameters $\tilde{\lambda}$ (rotational recrystallization), $\tilde{\beta}$ (migration recrystallization) and ι (basal-slip deformation) found from the inversion described in section 3.3 at three temperatures: $-30, -7, -5^\circ\text{C}$. The inverted-for parameters are shown as points along with a linear regression from these points for each parameter. A linear regression gave the best fit to results at -20°C , this is discussed in section 3.5.1. Note the broken y-axis as the parameter $\tilde{\lambda}$ changes much less than ι and $\tilde{\beta}$. 38

Figure 3.4 Caption on next page. 40

Figure 3.4 Comparison of the model with experiments performed in (a) simple shear (Journaux et al., 2019; Qi et al., 2019) and (b) compression (Craw et al., 2018; Piazzolo et al., 2013). The simulation parameters ($\tilde{\lambda}, \tilde{\beta}, \iota$) as functions of temperature were taken from the linear regression in fig. 3.3. Each row shows the comparison between the model and experiments at a specific temperature (and flow field). The first column shows a plot of the largest 2 eigenvalues of $\mathbf{A}^{(2)}$. The line represents the simulation and the circles show experimental values, with their size corresponding to the strain-rate at which they took place. The circles with numbers correspond to plotted experimental pole figures. These are shown alongside pole figures from the model at the same strain. In the top right, the J index for each pole figure is shown, above the number corresponding to the experimental point shown in the plot of $\mathbf{A}^{(2)}$. Table B.1 shows the experimental conditions. The model was run with the spherical harmonics truncated at $L = 12$.

- Figure 3.5 Comparison of model predictions and experimental data showing cone angle θ of the fabric in compression (illustrated in the inset pole figure) against strain γ . Solid lines show results from models run at different temperatures using interpolated parameters as shown in fig. 3.3. This figure is from Fan et al. (2020). Experimental data points are shown as circles taken from experiments (Craw et al., 2018; Fan et al., 2020; Jacka, 2000; Jacka and Maccagnan, 1984; Montagnat et al., 2015; Piazzolo et al., 2013; Qi et al., 2017; Vaughan et al., 2017). The size of the marker corresponds to the strain-rate the experiment was performed at, and it is coloured by temperature. Representation chosen and experimental data based on fig 14 and table 4 in Fan et al. (2020). 43
- Figure 4.1 Schematics illustrating two-dimensional flow regimes at different vorticity numbers \mathcal{W} (eq. (4.1)): (a) Pure shear ($\mathcal{W} = 0$), (b) Simple shear ($\mathcal{W} = 1$), (c) Pure rotation ($\mathcal{W} = \infty$). For each flow the streamlines and deformation regime produced are shown. 54
- Figure 4.2 Illustrative figure showing the vorticity number for ice flowing at a divide, showing a range from 0 to 1. The problem setup is from Martín et al. (2009) with isotropic ice. The simulation has an aspect ratio of 20, but only the region from $x = 0$ to $x = 10H$, where H is the height of model domain, is shown. The domain has the velocity from the shallow-ice-approximation imposed at the left and right boundaries, and the surface accumulation is set to match the outflow, corresponding to a steady state. No-slip is imposed at the base and a free surface is assumed at the top. The vorticity number is shown, alongside streamlines. This flow was computed using a full-Stokes solver written in FEniCS (Martin Alnæs et al., 2015) with $n = 3$ and solved using Taylor-Hood elements. 55

- Figure 4.3 The vorticity number for a 2D slice from a modified version of the [ISMIP-HOM Experiment F benchmark](#) (Pattyn et al., 2008). The ice is flowing from left to right, down a hill with angle 3.0° , and encounters a Gaussian bump at the base. Compared to Pattyn et al. (2008), the Gaussian bump is 4 times higher and 31.6 times sharper. Over the bump the flow accelerates leading to vorticity numbers greater than 1. This simulation was performed using Elmer/ICE (Gagliardini et al., 2013) with $n = 1$. 56
- Figure 4.4 Vorticity number (defined in eq. (4.1)) calculated from the surface velocity data of Antarctica (Mouginot et al., 2019) after averaging over a 10×10 block and taking the mean value within each block. The calculation uses the horizontal velocity fields from the observed surface velocity combined with an estimate of the average vertical shear predicted to occur in the top 25% of the ice sheet using the shallow-ice-approximation. The colour shows the vorticity number on a log scale. The transparency shows the relative error: an error in \mathcal{W} of 100% or greater is plotted as white and an error of 0% is plotted as the full colour. The inset shows the Ross Ice Shelf, with the easting and northing in Antarctic polar stereographic coordinates. This shows considerable variation across the continent, including deformation regimes not accessible in the laboratory. 58
- Figure 4.5 The model parameters $\iota, \tilde{\lambda}, \tilde{\beta}$ as functions of temperature, determined by linear regression to experimental data in both compression and simple shear, as conducted in Richards et al. (2021b). The 95% and 80% confidence intervals are shown. 60

- Figure 4.6 To illustrate the fabric I show a simulation in simple shear at $T = -5^\circ \text{C}$. (a) shows a pole figure from the model at an effective strain of $\gamma = 0.345$ (where the strain-rate is defined as in eq. (4.2)). (b) shows a pole figure from laboratory experiments (Qi et al., 2019) at the same temperature and strain, showing good agreement. The white dotted line in (a) and (b) shows $y = 0$. (c) shows $\bar{\rho}^*$ at $y = 0$ against strain. Here the white dotted line highlights the strain at which the pole figure is plotted. θ is the polar angle. Also highlighted is the classification of the different fabric types at different strains; from double-maxima to secondary cluster to the steady state single maxima. For this figure only the principal axes of deformation are oriented at $\theta = \pm 45^\circ$. 62
- Figure 4.7 Slices of the pole figure showing the value of ρ^* at $y = 0$ for an array of temperatures and vorticity numbers. All $y = 0$ plots go to a strain of $\gamma = 1$. The colour limits are the same for all plots. 64
- Figure 4.8 Pole figure for $\mathcal{W} \rightarrow \infty$ and $T = -5^\circ \text{C}$ at steady-state. A very weak girdle fabric is produced, with the girdle coincident with the axis of vorticity, shown. This fabric has a J index of 1.16, where $J = 1$ is an isotropic fabric. 65
- Figure 4.9 Contour plots showing the angle (in degrees) of the largest cluster from the compression axis. Panels are shown for progressively increasing finite strain values. This angle is fairly invariant with finite strain. The resolution of this figure is 50×50 across the parameter space. 67
- Figure 4.10 Regime diagram of the different fabric patterns which occur (defined in fig. 2.4). The angle of the primary cluster in fig. 4.9 at 20° and 50° is also overlaid. As in fig. 4.9 diagrams are shown for discrete strain values. The resolution of this figure is 50×50 across the parameter space. 68

- Figure 4.11 Pole figures overlaid onto the regimes at $\gamma = 2$. The pole figures are centred at the vorticity number and temperature they occur. 69
- Figure 4.12 Properties of steady-state fabrics across the $\mathcal{W} - T$ parameter space. (a) shows the strain at which the fabric, at constant T and \mathcal{W} , reaches steady-state (defined as a rolling average of the J index over a strain window of 2 gets within 5% of the steady-state value). (b) shows the J index at the steady state. (c) shows the plot of J against strain γ at $T = -30^\circ \text{C}$, $\mathcal{W} = 0.01$, with the calculated steady-state strain 71
- Figure 5.1 Adapted from Kirchner et al. (2011), showing the vertical velocity profile for the a) shallow ice approximation, b) shallow shelf approximation, and c) a mix of the two, valid for an ice stream such as at EGRIP. 82
- Figure 5.2 View showing an overview of Greenland in (a), showing the velocity magnitude calculated from Joughin et al. (2018) and a rectangle describing the inset region in (b), which shows the tracked plan-view path upstream of the EGRIP ice core location. The location of the Greenland Ice Core Project (GRIP) core is also shown. 83
- Figure 5.3 Pole figure from Stoll (2019), at a depth of 1361.02 m. This shows both a girdle pattern, but also two horizontal maxima. The pole figure is shown with the z -axis out of the page. Note that the orientation of the pole figure is unconstrained when rotating about the z axis. This is because when ice cores are drilled they are free to rotate and this information is usually lost. 84
- Figure 5.4 Girdle fabric from Westhoff et al. (2020), where the orientation of the girdle has been found. This figure shows c -axis data averaged over a depth 1400 – 2100 m. The pole figure is shown with the z -axis out of the page, North at 0° . The girdle is perpendicular to the flow-direction. 85

- Figure 5.5 Figure for $u_b = u_s$ (no vertical shear) showing (a): 3D streamline paths and pole-figures aligned with the streamline axis (s, z) and (b): the eigenvalues of $\mathbf{A}^{(2)}$ with depth, and pole figures from the model output aligned with the North and East directions at the corresponding depths (the same orientation as fig. 5.4.) Note some streamlines cross due to changes in accumulation with time, this is discussed in section 3.4. 90
- Figure 5.6 Figure for $u_b = 0$ showing (a): 3D streamline paths and pole-figures aligned with the streamline axis (s, z) and (b): the eigenvalues of $\mathbf{A}^{(2)}$ with depth, and pole figures from the model output aligned with the North and East directions at the corresponding depths (the same orientation as fig. 5.4.) Note some streamlines cross due to changes in accumulation with time, this is discussed in section 3.4. 91
- Figure 5.7 Figure for $u_b = 0.9u_s$ (basal velocity 90% the surface velocity) showing (a): 3D streamline paths and pole-figures aligned with the streamline axis (s, z) and (b): the eigenvalues of $\mathbf{A}^{(2)}$ with depth, and pole figures from the model output aligned with the North and East directions at the corresponding depths (the same orientation as fig. 5.4.) Note some streamlines cross due to changes in accumulation with time, this is discussed in section 3.4. 92
- Figure 5.8 Plot of the calculated value of u_b/u_s from Gerber et al. (2021) along the streamline, used in fig. 5.9 93
- Figure 5.9 Figure like figs. 5.5 and 5.6 for a variable $\frac{u_b}{u_s}(s)$, from Gerber et al. (2021) 93
- Figure 5.10 Figure like fig. 5.5 with $u_b = u_s$ but $\lambda = \lambda_0/3$, where λ is the parameter controlling rotational recrystallization. 94

- Figure 5.11 Plot showing a regression for $\tilde{\lambda} = \lambda/\dot{\gamma}$ for (a) strain-rate dependence only, and (b) temperature dependence only. The points used in the regression (from both chapters 3 and 5), 95% confidence interval and R^2 values are shown. 97
- Figure 6.1 A schematic of the numerical procedure for the proposed coupled model for anisotropic viscous flow of ice deformed by dislocation creep. Starting at the top left, the anisotropic viscosity tensor is calculated in terms of the fabric, represented by $\mathbf{A}^{(2)}$ and $\mathbf{A}^{(4)}$ - see section 2.2.2. From this the flow field can be calculated, depending on the geometry and boundary conditions. Then the fabric at the next timestep can be found using SpecCAF 102
- Figure 6.2 Velocity magnitude at $t = 0$, with an isotropic fabric everywhere. Annotations show the boundary conditions: a pressure inlet on the length, a line of symmetry in the centre (so the top half of the simulation is not computed, but a reflection of the bottom), an outlet on the right, no-slip walls to describe the obstruction and free-slip walls elsewhere. The colour scale is chosen to match fig. 6.3 105
- Figure 6.3 Plot of velocity magnitude like fig. 6.2 but at the end of the simulation ($t = 4.1$). 106
- Figure 6.4 Plot of $A_{xx}^{(2)}$, the component of the second-order orientation tensor aligned with the flow direction, at the end of the simulation. At $t = 0$ $A_{xx}^{(2)}$ was 1/3 (grey) everywhere. 106
- Figure 6.5 Plot of $A_{yy}^{(2)}$ (y is vertically upwards), at the end of the simulation. At $t = 0$ $A_{yy}^{(2)}$ was 1/3 (grey) everywhere. 107

Figure B.1	The error in the eigenvalues of $\mathbf{A}^{(2)}$ and corresponding pole figures for different values of the number of spectral modes L , illustrating the higher resolution arising for large L . The illustrative parameters $\tilde{\lambda} = 0.05, \iota = 1, \tilde{\beta} = 1$ were chosen here. Both the error and the pole figures are shown at an arbitrary strain of $\gamma = 1$. The error is calculated relative to a highly numerically resolved solution with $L = 50$. The plot shows the exponential convergence of the spectral method. 124
Figure C.1	As fig. 4.7 but with $\iota_{\max}, \tilde{\beta}_{\max}, \tilde{\lambda}_{\min}$, to give the strongest fabric. 128
Figure C.2	As fig. 4.7 but with $\iota_{\min}, \tilde{\beta}_{\min}, \tilde{\lambda}_{\max}$, to give the weakest fabric. 129
Figure C.3	As fig. 4.9 but with $\iota_{\max}, \tilde{\beta}_{\max}, \tilde{\lambda}_{\min}$, to give the strongest fabric. 130
Figure C.4	As fig. 4.9 but with $\iota_{\min}, \tilde{\beta}_{\min}, \tilde{\lambda}_{\max}$, to give the weakest fabric. 131
Figure C.5	As fig. 4.10 but with $\iota_{\max}, \tilde{\beta}_{\max}, \tilde{\lambda}_{\min}$, to give the strongest fabric. 132
Figure C.6	As fig. 4.10 but with $\iota_{\min}, \tilde{\beta}_{\min}, \tilde{\lambda}_{\max}$, to give the weakest fabric. 133
Figure C.7	As fig. 4.11 but with $\iota_{\max}, \tilde{\beta}_{\max}, \tilde{\lambda}_{\min}$, to give the strongest fabric. 134
Figure C.8	As fig. 4.11 but with $\iota_{\min}, \tilde{\beta}_{\min}, \tilde{\lambda}_{\max}$, to give the weakest fabric. 135
Figure C.9	As fig. 4.12 but with $\iota_{\max}, \tilde{\beta}_{\max}, \tilde{\lambda}_{\min}$, to give the strongest fabric. 136
Figure C.10	As fig. 4.12 but with $\iota_{\min}, \tilde{\beta}_{\min}, \tilde{\lambda}_{\max}$, to give the weakest fabric. 137

LIST OF TABLES

Table 3.1	Table showing the results from the inversion for parameters. The inversion was performed for 7 bins in total, each with a mean temperate and strain-rate. The coefficient of variance is also shown, along with the parameters. 46
Table 3.2	Table showing the regression results using the inversion data in table 3.1. Results are shown both with and without strain-rate dependence. The R^2 and adjusted R^2 values are also shown, along with the 95% confidence intervals for each fitted parameter. 47
Table B.1	Table showing the experimental data used in fig. 3.4. The first column gives experimental number shown in the plot of $\mathbf{A}^{(2)}$ and beside the experimental pole figures in fig. 3.4. This is followed by the paper the data was published in and the conditions the experiment was run at. 125

ACRONYMS

CAFFE	Continuum-mechanical, Anisotropic Flow model, based on an anisotropic Flow Enhancement factor
CPO	Crystallographic Preferred Orientation
EGRIP	East Greenland Ice Core Project
FEniCS	Finite Element Computational Software
GOLF	General Orthotropic Linear Flow law
GRIP	Greenland Ice Core Project
ISMIP-HOM	Ice Sheet Model Intercomparison Project for Higher-Order Models
LEoPART	Lagrangian-Eulerian on Particles
NEGIS	North East Greenland Ice Stream
SIA	Shallow Ice Approximation
SSA	Shallow Shelf Approximation

INTRODUCTION

Mass loss from ice sheets is set to be the main contributor to sea-level rise this century (e.g. Shepherd et al., 2018). Reliably predicting sea-level rise depends on accurately modelling ice flow. One of the most important controls on ice flow dynamics is the ice fabric, i.e. the arrangement of the crystallographic axes within a polycrystal. Strong alignment of the crystal lattices may cause the strain-rate response to an applied stress to vary by a factor of 9 in different directions (e.g. Pimienta and Duval, 1987). Hence, understanding the fabrics present in any flowing ice sheet, i.e. Antarctica or Greenland, is important for predicting ice-sheet flow and, in turn, the loss of ice over time. Furthermore, with understanding ice fabric we can infer other properties deep into the ice-sheet, such as deformation, basal-conditions and temperature variations.

The damage caused by sea-level rise will cause significant hardship in terms of livelihood and habitat loss. The damage is likely to hurt most those people living in the poorest parts of the world, such as the small islands in the South Pacific and around river deltas in Bangladesh (Byravan and Rajan, 2010). Improving our understanding of ice dynamics allows a greater understanding of the flow of ice-sheets and therefore leads to more accurate predictions of the magnitude of this sea-level rise, allowing for better planning and mitigation in areas most affected.

When ice deforms or flows, the crystals within align along preferred directions. The distribution of crystal orientations is called the fabric or Crystallographic Preferred Orientation (CPO). Ice develops a fabric whenever it is deformed, and the fabric pattern produced is dependent on factors such as the deformation and temperature history. Therefore, by understanding the fabric we can infer information about processes deep into the ice-sheet, such as deformation conditions, temperature and the level of slip at the base of the ice sheet.

The fabric of ice also leads to viscous anisotropy in the ice. This means the viscosity of ice varies with direction. It has been shown that the flow rate of ice can vary by a factor of 9 in different directions (e.g. Pimienta and Duval, 1987). The flow itself in turn influences the fabric. This dynamic coupling between the flow field and the fabric

makes the study of ice a mathematically rich problem, and accurately modelling ice fabrics key for predicting the flow of ice. Despite the above, viscous anisotropy is commonly neglected or incorporated very crudely, in part because ice fabric evolution models cannot accurately reproduce fabrics seen in the natural world.

Due to the complexity, analysis and discussion of ice fabrics has focussed primarily on those deformed under a limited set of deformations. Fabrics from ice cores are commonly deformed under compression, as the majority of ice core sites are at these locations for better climate data. Fabrics from experiments are also limited primarily to compression or simple shear. The fabrics produced in these conditions are well known, but there is a need to extend this understanding to the whole space of possible deformations, in order to truly understand the deformations in ice-sheets.

The study of ice fabrics and anisotropy present in ice also has many parallels with other areas. Olivine aggregates that govern the rheology of the Earth's mantle are also an area where crystalline anisotropy influences a viscous flow. Improving our understanding of ice fabrics can also lead us to improve our understanding of these other materials, with have key geophysical importance.

1.1 RESEARCH QUESTIONS

To improve our understanding and modelling of ice fabrics, in this thesis I present a new, validated continuum model for ice fabric evolution and compare it to both laboratory experimental results and real-world conditions, as well as using it to explore a range of general deformations and temperature conditions. The main research questions I explore in this thesis are:

- Q1: How can we improve our modelling of ice fabrics, including all key processes while retaining computational efficiency?
- Q2: How do the processes affecting fabric evolution vary with temperature and strain-rate?
- Q3: Can we explain fabric patterns produced in completely general deformations, both in nature and in laboratory experiments, by taking exclusively deformation by dislocation creep into account?
- Q4: How can the developed fabric evolution model be used to improve our understanding of the dynamics of ice sheets?

Q5: What is needed from a fabric evolution model to simulate viscous anisotropy and have we reached this stage?

1.2 THESIS OUTLINE

Including this introduction, this thesis contains 7 Chapters. Chapter 2 introduces the key concepts and theory from literature for ice fabric, ice rheology and viscous anisotropy, and both small and large-scale modelling approaches. This is followed by 3 chapters of original scientific research, covering the development of a novel, constrained continuum ice fabric evolution model, and its application to both general deformations and temperatures - to explore the whole parameter space of fabrics, as well as applying it to simulate fabrics observed in an ice core obtained from a real-world location. Chapter 6 contains an overview of ongoing work to couple ice fabric evolution to viscous anisotropy, as well as possible future directions. Finally in chapter 7 I provide a general discussion of the findings in this thesis, specifically in light of the research questions above, and finish with conclusions.

Chapter 3 outlines my development of the SpecCAF model: a mesoscopic continuum equation for fabric evolution. The chapter describes the novel spectral solution method, and the process of comparing the model to experiments to constrain the parameters as functions of temperature. This results in the first fully constrained model for ice fabric evolution. This chapter represents the content of Richards et al. (2021b).

Chapter 4 describes the application of the SpecCAF model described previously to natural two-dimensional flows. This is motivated by the fact that the literature tends to consider only the cases of pure and simple shear. We extend this by using the model to explore the fabrics produced by deformations between pure and simple shear, as well as those more rotational than simple shear. This includes presenting a regime diagram for fabric patterns and using the model to explore steady-state properties not reachable in experiments. This chapter largely represents the content of Richards et al. (2021a).

Chapter 5 uses SpecCAF to simulate the fabrics from ice cores taken from the EGRIP site, a new drilling site in an active ice stream. Here, I use satellite data, combined with assumptions based on the shallow ice approximation with basal-slip, to predict the upstream path and velocity gradient tensor upstream of EGRIP. I can then predict the fabric using the deformation along the path. We compare the fabrics by

SpecCAF with the results from [EGRIP](#), and use this to infer information about the strain-rate dependence of parameters and conditions in the ice-sheet such as the level of basal-slip at [EGRIP](#).

BACKGROUND

This chapter gives an overview of the theory behind modelling fabric evolution and viscous anisotropy in ice. I begin with a description of the ice crystal structure at a microscopic scale, and the microstructural processes relevant to the ice fabric. I then review the modelling approaches for fabric evolution with a focus on models which can be incorporated into large-scale ice-sheet models. I then cover the current approaches to represent the anisotropic viscous rheology.

2.1 ICE MICROSTRUCTURE

The anisotropy of ice occurs due to its poly-crystalline microstructure. The ice that occurs naturally on Earth is known as Ice-1h and forms a hexagonal lattice structure as seen in fig. 2.1. Due to the hexagonal structure, the ice crystal has rotational symmetry. The axis of this symmetry is called the *c*-axis and is normal to the basal plane. A connected region of crystalline lattice with a common orientations is termed a *grain* and the regions between grains are termed grain boundaries. A polycrystal refers to a region of ice that contains a number of grains, and this can vary in size. The fabric or crystallographic preferred orientation (CPO) of a polycrystal refers to the distribution of crystal orientations within a polycrystal. A polycrystal with a random distribution of lattice orientations is said to have an isotropic fabric or no CPO. Other names used in the literature for fabric are texture or lattice preferred orientation (LPO).

2.1.1 *Processes affecting fabric evolution*

Ice in the natural world, which mostly exists relatively close to its melting point, will undergo creep when deformed. This is in a similar manner to polycrystalline materials such as olivine in the mantle and metals. Ice is considered a good model material for studying these other polycrystalline materials (Wilson et al., 2014). This creep can then be described as a ‘flow’ at large scales. For ice deformed in both the laboratory and in ice-sheets, it is creep through the movement

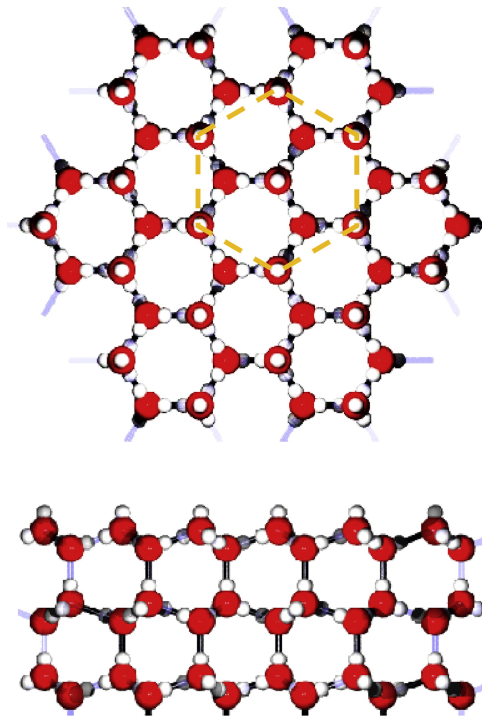


Figure 2.1: Image from Faria et al. (2014). Ice 1h. Red represents oxygen, white hydrogen. The hexagonal symmetry is shown by the yellow dashed line. The top view is along the c -axis, whereas the bottom view is along the a -axis.

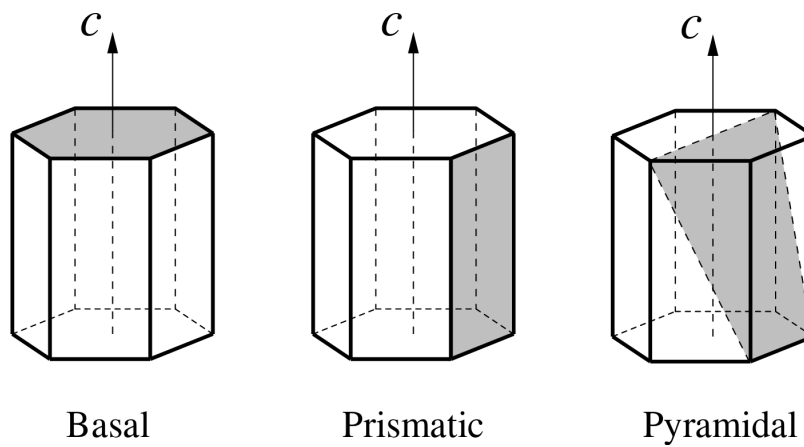


Figure 2.2: Sketch of the primary slip systems in ice, taken from Placidi (2005). The figure shows the hexagonal lattice structure and the c -axis.

of dislocations - local defects in the lattice arrangement caused by impurities or a local excess or deficiency of hydrogen atoms (Glen, 1968) - that is generally considered to dominate (Goodman et al., 1981; Paterson, 1999).

From dislocation theory (e.g. Weertman and Julia R. Weertman, 1992) the slip systems in ice - planes along which dislocations can move - are shown in fig. 2.2. Of these slip systems, dislocation creep along the basal plane is approximately 70 times easier than prismatic slip, and 180 times easier than pyramidal slip (Duval et al., 1983). Consequently, for temperatures typical in an ice sheet (-10°C to -30°C) basal-slip tends to dominate (Duval et al., 2010). Nevertheless, slip on the other planes must occur due to geometric compatibility. Recent work (Chauve et al., 2017) shows that in certain conditions non-basal slip can account for up to 30% of the deformation. However, despite this, dislocation creep along the basal planes (basal-slip deformation) dominates the contribution to macroscopic deformation (e.g. Petrenko and Whitworth, 2002)

As mentioned above, the normal to the basal plane is called the c -axis and due to the dominance of basal-slip deformation it is a common assumption to consider only the distribution of the c -axes when describing the ice fabric. As ice flows, the c -axes align to produce a fabric from the combination of deformation and recrystallization. Figure 2.3 illustrates schematically the deformation and recrystallization processes that affect the fabric: basal-slip deformation, rigid-body rotation, rotational recrystallization and migration recrystallization, which I will describe in turn below. For each, the effect on the microstructure is shown above a diagram, referred to as a pole figure, in which the shading indicates the mass distribution of c -axis orientations projected onto a plane. Since the pole figures are antipodally symmetric, it shows all the orientation information.

The effect of basal-slip deformation on the fabric (fig. 2.3a) can be understood through an analogy to a deck of cards sliding over one another: under compression the c -axes tend to rotate towards the axis of compression (Azuma and Higashi, 1984). A corresponding pole figure of the mass distribution of c -axis orientations shows the movement of a cluster of c -axes towards the compression axis. Furthermore, any vorticity in the flow acts to rotate the c -axes around the axis of vorticity (fig. 2.3b). Under these two mechanisms the change in orientation of the c -axis of a single grain can be described by

$$\dot{c}_i = w_{ij}c_j - \iota(d_{ij}c_j - d_{kl}c_l c_k c_i), \quad (2.1)$$

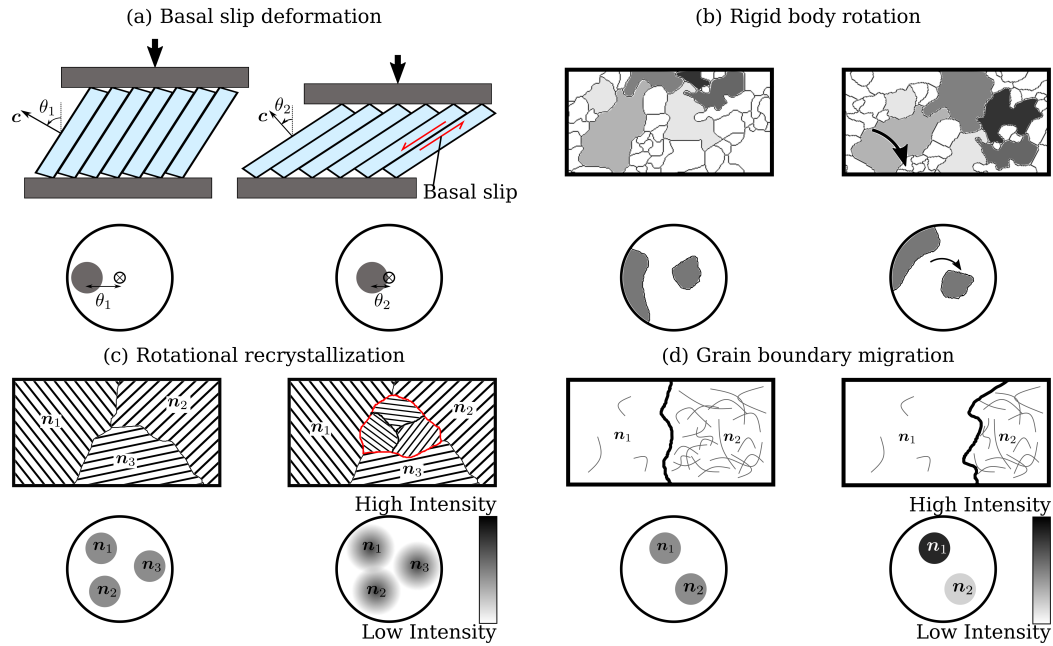


Figure 2.3: Diagram showing the four processes that can affect the ice fabric. An illustration of the mechanism on the microstructure, as well as the resulting effect on a pole figure of orientation mass distributions is shown for each one. (a) Under basal slip deformation, the c -axis rotates towards the axis of compression. In the pole figure for this case the cluster of c -axes at θ_1 also move towards the compression axis. (b) Rigid body rotation: any vorticity in the flow acts to rotate the crystallites and their c -axes around the axis of rotation. (c) Rotational recrystallization: $n_{1,2,3}$ represent grains with their orientation illustrated by the direction of hatching. Sub grains form at the boundaries between larger grains with intermediate orientations. In the pole figure, this translates to a diffusion of high intensity clusters of orientation towards $n_{1,2,3}$. (d) Migration recrystallization: the grain with a lower dislocation density, with orientation n_1 , migrates into the grain with a higher dislocation density. In the pole figure, the mass fraction of c -axes towards n_1 increases and the mass fraction towards n_2 decreases.

where \mathbf{w} and \mathbf{d} are the spin and strain-rate tensors of the individual grain or crystal and $\iota \leq 1$ is a parameter. For the case of slip only on the basal-plane $\iota = 1$. The first term $w_{ij}c_j$ represents the change in the c -axis due to rotation in the flow. The second term describes mathematically the process illustrated in fig. 2.3a for basal-slip deformation.

Rotational recrystallization and its effect on the microstructure is illustrated in fig. 2.3c. This occurs when dislocations in the microstructure recover into subgrain boundaries which, with increasing strain, will develop into grains (Drury et al., 1985). As dislocations are concentrated close to grain boundaries due to stress heterogeneities (Piazolo et al., 2015), subgrains, and therefore new grains developing from subgrains, tend to occur near grain boundaries. The orientation of these new grains is similar to their parent grains but has some random difference. This random process on the micro-scale causes a diffusion of any clusters of orientation in the distribution function (Gödert, 2003).

Figure 2.3d illustrates migration recrystallization, again illustrating the microstructural affect and the corresponding change in a pole figure. Migration recrystallization is mainly driven by a difference in strain energy i.e. energy related to unbound dislocation density either side of a grain boundary (e.g. Humphreys and Hatherly, 2004). Hence, in the case of such strain induced migration recrystallization (Drury et al., 1985; Drury and Urai, 1990) the less strained grain grows at the expense of the more strained grain resulting in an overall decrease in the strain energy of the system. As the strain energy stored in a grain (corresponding to the dislocation density) is directly related to the imposed stress (Gottstein and Shvindlerman, 1999) migration recrystallization is inherently related to stress as well. The dislocation density accumulated within a certain grain is primarily a response to its orientation relative to the main deviatoric stress axes. For example, a grain favourably oriented for basal slip (which as discussed earlier requires far less stress than other slip systems) will accumulate less dislocations than a grain that is oriented unfavourably. Consequently, depending on the deformation regime, grains of certain orientation will grow at the expense of grains of another unfavourable orientation. As a result, the effect of migration recrystallization is to produce c -axes clustered towards certain orientations in a polycrystal.

The above processes are all driven through the movement of dislocations in the ice lattice. Another process which may cause ice to deform is diffusional creep. This may occur for ice deformed at very

low stresses with very low grain sizes (Azuma et al., 1999; Goldsby and Kohlstedt, 1997).

Grain boundary sliding is another deformation mechanism, which is accommodated by either diffusional or dislocation creep. This occurs when grains slide relative to each other. Grain boundary sliding on its own will not produce a fabric (Zhang et al., 1994) however dislocation creep acting to accommodate grain boundary sliding will still produce a fabric. It has been suggested that grain boundary sliding may be the dominant, or a significant mechanism at the stress and strain-rates of ice sheets (Goldsby and Kohlstedt, 2001). However, this is controversial (Duval and Montagnat, 2002), because deformation primarily by grain boundary sliding will either not produce a fabric, or produce a much weaker fabric than deformation solely by dislocation creep. This would seem inconsistent with the strong fabrics consistently observed from cores taken from ice sheets (Duval and Montagnat, 2002).

2.1.2 *Observed fabrics*

Ice fabrics can be observed through laboratory experiments, through ice cores from real-world locations, and, more recently, inferred through seismic and radar measurements.

In the laboratory, the majority of experiments are performed in compression, either in pure shear (2D) or unconfined (uniaxial) compression (3D), without any rotational component (e.g. Craw et al., 2018; Fan et al., 2020; Jacka, 2000; Jacka and Maccagnan, 1984; Piazzolo et al., 2013). The other endmember considered is simple-shear (Journaux et al., 2019; Qi et al., 2019). Laboratory experiments provide detailed fabric measurements in known conditions. However experiments are mostly limited to endmember deformation regimes, as well as to strains of around 0.4 for compression (Fan et al., 2020) and 2 for direct simple shear (Qi et al., 2019).

Fabrics can also be analysed by taking ice cores in ice sheets. An understanding of these fabrics enables us to interpret the deformation regime and temperature history of ice cores. Initial studies of ice cores have concentrated on ice domes or divides (Gow, 1961; Holtzschcherer et al., 1954; Johnsen et al., 1995). These locations are deliberately chosen because they have minimal deformation, to act as a good proxy for past climate data. At domes, the ice will be deformed vertically in unconfined compression, producing either a single-maximum or a girdle shape fabric (fig. 2.4). Recently, ice cores have become available

in locations with more complex deformation regime histories (Stoll, 2019; Treverrow et al., 2010). Stoll (2019) show examples of a variety of fabric shapes such as girdles and single-maximum fabrics orientated in different directions as well as relatively faster fabric development with depth compared to ice cores taken at or near divides. Fabrics can also be measured from boreholes using sonic and optical techniques (Gusmeroli et al., 2012; Kluskiewicz et al., 2017).

Recently, data from radar and seismics has also been used to infer fabric properties (Booth et al., 2020; Fujita et al., 2006; Matsuoka et al., 2003). These methods can capture natural ice fabrics without expensive drilling, allowing data to be collected at more active locations such as ice streams (Jordan et al., 2020).

2.1.3 *Fabric patterns*

Figure 2.4 illustrates schematically some commonly observed fabric patterns seen in laboratory experiments and from ice cores. These are illustrated by pole figures as in fig. 2.3. Laboratory experiments studying fabric evolution have been performed mostly in uniaxial compression and this produces either a single maximum at low temperatures (fig. 2.4a) or a cone-shape fabric at high temperatures (fig. 2.4b). At low temperatures ($T \approx -30^\circ\text{C}$) the basal-slip deformation regime dominates and this causes c -axes to rotate towards the axis of compression, producing the single-maximum shown in fig. 2.4a. The cone-shape fabric shown in fig. 2.4b, seen in experiments such as Kamb (1972), is produced by the balance of basal-slip deformation and migration recrystallization. The process of migration recrystallization acts to consume grains orientated towards the compression axis, and grow grains orientated in a ring 45° away from the compression axis. Therefore, the balance of basal-slip deformation regime and migration recrystallization produces a ring or cone-shape pattern in the pole figure. In pure shear (2D compression), the grains produced by migration recrystallization instead form two clusters at 45° . This is shown in fig. 2.4c. This can be thought of like a cone-shape fabric confined to two dimensions. This has been seen in experiments such as Budd et al. (2013).

Recent simple shear experiments produce either a single-maximum at low temperatures, or a single-maximum with an offset secondary cluster (fig. 2.4d) at intermediate strains and high temperatures (Journaux et al., 2019; Qi et al., 2019). This pattern is similar to a double-

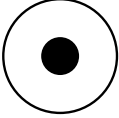
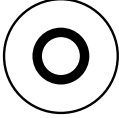


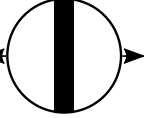
Fabric name	(a) Single-maximum	(b) Cone-shape	(c) Double-maximum	(d) Secondary cluster	(e) Girdle
Pole figure					
Deformation	Compression, Simple shear	Unconfined compression	Confined compression	Simple shear	Unconfined extension
Temperature	Low (~ -30°C)	High (~ -10°C)	High (~ -10°C)	High (~ -10°C)	Low (~ -30°C)

Figure 2.4: Illustration showing common fabrics or CPOs which develop in ice, illustrated by their pole figures, as well as the deformation regime and temperature they typically occur at. The pole figures show the distribution of c -axis orientations, with the compression axis at the centre. (a) shows a single-maximum fabric, produced in unconfined compression or simple shear at low temperatures (Qi et al., 2019). (b) shows a cone-shape fabric, produced in unconfined compression at higher temperatures, when grain-boundary migration is active (Paterson, 1999). This can also be considered a girdle fabric when the cone-angle approaches 90° . (c) shows a double maxima fabric produced in confined compression (pure shear) (Budd et al., 2013). (d) shows a single-maximum with a secondary cluster, produced in simple shear at higher temperatures (Kamb, 1972; Qi et al., 2019). The normal to the shear plane is at the centre of this pole figure. (e) shows a girdle fabric, expected to be produced in unconfined extension but not performed in the laboratory. The arrows show the extension direction.

maxima but the presence of vorticity in simple shear causes the cluster that is not aligned with the shear plane normal to be advected towards the primary cluster. As the secondary cluster's orientation changes, grains of that orientation accumulate more dislocations so start to be consumed by migration recrystallization. This results in the imbalance in cluster strengths seen in fig. 2.4d.

2.2 MODELLING ICE

2.2.1 *Overview of modelling approaches*

The range of interest in the deformation of ice is vast, ranging from micrometres for studying the microstructural, grain-grain interactions; to 1000s of kilometres when studying ice-sheets. Consequently, different approaches must be used depending on the scale one seeks to work on. At the smaller scale, approaches such as Llorens et al. (2016) and Piazzolo et al. (2015) model the microstructure directly using a discrete model incorporating deformation and recrystallization processes. This involves simulating both individual grains and the interactions between them. Any deformation is imposed as a boundary condition. Kennedy et al. (2013) take a similar approach by modelling a network of cuboids with each cuboid representing an individual grain. These approaches are key to improving our understanding of the processes that lead to fabric formation. However, since they require solving for the microstructure directly, they are too computationally expensive to be incorporated into models of ice sheet flows. Furthermore, they are unable to reproduce some commonly observed patterns seen in experiments and nature, including the secondary c -axis cluster commonly seen in pole figures for simple shear.

At a larger scale there are ice-sheet flow models, which are key to predicting future sea-level rise. However, the majority of models (e.g. Cornford et al., 2013; Larour et al., 2012; Lipscomb et al., 2018; Winkelmann et al., 2011) do not include viscous anisotropy or fabric evolution. Elmer/ICE (Gagliardini et al., 2013) incorporates anisotropy, and calculates the fabric development using an evolution equation for the second moment of the orientation distribution function (the second-order orientation tensor, defined below in section 2.2.3), without migration recrystallization. This approach is described in section 2.2.4.1. This approach is computationally inexpensive and can easily accommodate different deformations but cannot accurately re-

produce experimentally observed fabrics. The anisotropic viscosity is directly related to the fabric. Therefore, modelling the fabric accurately is key to modelling viscous anisotropy reliably.

2.2.2 Anisotropy and the flow of ice

Generally, the movement of large ice masses can be described by Stokes' equations for the flow of viscous incompressible fluid:

$$\begin{aligned}\frac{\partial S_{ij}}{\partial x_j} - \frac{\partial p}{\partial x_i} &= \rho g \\ \frac{\partial u_i}{\partial x_i} &= 0\end{aligned}\tag{2.2}$$

where \mathbf{S} is the deviatoric stress, p is the pressure, ρ is the density and \mathbf{g} the force due to gravity. To solve this an expression for the deviatoric stress is needed. Historically, the glaciological community has used Glen's law (Glen, 1952):

$$\mathbf{D} = A(T)\tau_e^{n-1}\mathbf{S}.\tag{2.3}$$

Here $\mathbf{D} = (\nabla\mathbf{u} + \nabla\mathbf{u}^T)/2$, the strain-rate tensor. The parameter $A(T)$ is a temperature dependent rate factor, $\tau_e = \sqrt{\frac{1}{2}S_{ij}S_{ij}}$, the second invariant of the deviatoric stress \mathbf{S} . This is a power-law fluid model. Note that eq. (2.3) is the inverse of the conventional form of a constitutive law, ($S_{ij} = \mu D_{ij}$). Expressing Glen's law in this form gives:

$$S_{ij} = (2A)^{-1/n}\dot{\gamma}^{\frac{1-n}{n}}D_{ij},\tag{2.4}$$

where $\dot{\gamma} = \sqrt{D_{ij}D_{ij}/2}$ is the effective strain-rate. Glen's law does not include any anisotropic effects. As mentioned in the introduction, the viscous anisotropy of ice, caused by the fabric, can cause the flow rate to vary by a factor of 9 in different directions. In this section I review the approaches in the literature to describe an anisotropic viscosity, such that the viscosity μ is replaced by fourth-rank tensor μ_{ijkl} .

2.2.2.1 Transverse isotropy

The simplest form of anisotropy is transverse isotropy, where the material has a plane of isotropy. Boehler (1987) gives the general expression for a transversely isotropic viscosity:

$$\mu_{ijkl} = \zeta_0 \left(\delta_{ik}\delta_{jl} + \zeta_1 v_i v_j v_k v_l + \zeta_2 (\delta_{ik} v_l v_j + v_i v_k \delta_{jl}) - \frac{1}{3} (\zeta_1 + 2\zeta_2) v_k v_l \delta_{ij} \right), \quad (2.5)$$

where v is the unit normal to the plane of isotropy, $\zeta_0, \zeta_1, \zeta_2$ are parameters currently undefined and δ_{ij} is the identity tensor. An inverse expression for the fluidity is also valid for transverse isotropy:

$$\mathcal{F}_{ijkl} = \zeta_0 \left(\delta_{ik}\delta_{jl} + \zeta_1 v_i v_j v_k v_l + \zeta_2 (\delta_{ik} v_l v_j + v_i v_k \delta_{jl}) - \frac{1}{3} (\zeta_1 + 2\zeta_2) v_k v_l \delta_{ij} \right), \quad (2.6)$$

where \mathcal{F} is the fluidity and again $\zeta_0, \zeta_1, \zeta_2$ are parameters left undefined.

For the case of an ice grain, the assumption of transverse isotropy is reasonable, and the plane of isotropy is the basal plane. Meyssonier and Philip (1996) has applied eqs. (2.5) and (2.6) to describe the behaviour of a single grain, for linear ($n = 1$) behaviour:

$$s_{ij} = \frac{2\eta}{\beta} \left[\delta_{ik}\delta_{jl} + 2(\gamma - \beta) c_i c_j c_k c_l + (\beta - 1) (\delta_{ik} c_l c_j + c_i c_k \delta_{jl}) - \frac{2}{3} (\gamma - 1) c_k c_l \delta_{ij} \right] d_{kl}, \quad (2.7)$$

where the c -axis describes the normal to the plane of isotropy. The parameter $\gamma \approx 1$ is the ratio of the viscosity in compression or tension along the c -axis to that in the basal plane, and $\beta \approx 0.01$ is the ratio of viscosity of a grain in shear parallel to the basal plane to that in the basal plane. As in eq. (2.1) a lower-case is used to denote individual grain properties, with \mathbf{s} and \mathbf{d} representing the stress and strain-rate tensors for the grain. The alternative form, starting from eq. (2.6) instead of eq. (2.5) is:

$$d_{ij} = \frac{\beta}{2\eta} \left[\delta_{ik}\delta_{jl} + 2 \left(\frac{\gamma + 2}{4\gamma - 1} - \frac{1}{\beta} \right) c_i c_j c_k c_l + \left(\frac{1}{\beta} - 1 \right) (\delta_{ik} c_l c_j + c_i c_k \delta_{jl}) - \frac{2}{3} \left(\frac{\gamma + 2}{4\gamma - 1} - 1 \right) c_k c_l \delta_{ij} \right] s_{kl} \quad (2.8)$$

Both eqs. (2.7) and (2.8) provide valid expressions for the linear behaviour of a transversely isotropic ice grain.

2.2.2.2 Taylor and Sachs bounds

To transform from the grain-scale expressions in eqs. (2.7) and (2.8) to expressions for the macroscopic viscosity or fluidity we must make further assumptions. As an analogy, we can view a polycrystal as being composed of individual grains that are mechanically connected in a network. Although the connectivity in the network is unknown we can consider the two extreme cases of parallel and series connections where all the grains experiences the same strain-rate or the same stress. These represent bounds on the behaviour of the network. These cases corresponds respectively to the Taylor and Sachs hypothesis and can be used give a flow law for large-scale ice dynamics.

The Taylor or Voigt bound assumes that all grains experience the macroscopic strain:

$$\mathbf{d}(\mathbf{x}, t) = \mathbf{D}(\mathbf{x}, t). \quad (2.9)$$

It is well known that this approximation violates stress equilibrium and is a poor approximation for ice (Castelnau et al., 1996), however it acts as an upper bound for the anisotropy. Combining eq. (2.9) and eq. (2.7) gives an expression for a macroscopic flow law:

$$S_{ij} = \frac{2\eta}{\beta} \left[\delta_{ik}\delta_{jl} + 2(\gamma - \beta)A_{ijkl}^{(4)} + (\beta - 1)(\delta_{ik}A_{lj}^{(2)} + A_{ik}^{(2)}\delta_{jl}) - \frac{2}{3}(\gamma - 1)A_{kl}^{(2)}\delta_{ij} \right] D_{kl}. \quad (2.10)$$

Here $\mathbf{A}^{(2)}$ and $\mathbf{A}^{(4)}$ are the second and fourth-order orientation tensors respectively. When averaging over physical grains these are defined as:

$$A_{ij}^{(2)} = \sum_{g=1}^N f^g c_i^g c_j^g, \quad (2.11)$$

where N is the number of grains, f^g is the volume fraction of grain g with c -axis c^g (Gagliardini et al., 2009). Similarly $\mathbf{A}^{(4)}$ can be defined as:

$$A_{ijkl}^{(4)} = \sum_{g=1}^N f^g c_i^g c_j^g c_k^g c_l^g. \quad (2.12)$$

I discuss orientation tensors further in section 2.2.3. Equation (2.10) gives an anisotropic rheology which can be combined with eq. (2.2) to find the flow field.

The other end member is the Sachs hypothesis (also known as the Reuss hypothesis or the static bound) from Sachs (1929). This assumes the macroscopic stress is imposed on all the grains:

$$s(\mathbf{x}, t) = \mathbf{S}(\mathbf{x}, t). \quad (2.13)$$

This violates strain compatibility and acts as a lower bound for the anisotropy. However it is known to be much closer to reality for ice than the Taylor hypothesis (Castelnau et al., 1996). Combining eq. (2.13) and eq. (2.8) gives an alternative macroscopic flow law:

$$D_{ij} = \frac{\beta}{2\eta} \left[\delta_{ik}\delta_{jl} + 2\left(\frac{\gamma+2}{4\gamma-1} - \frac{1}{\beta}\right)A_{ijkl}^{(4)} + \left(\frac{1}{\beta} - 1\right)(\delta_{ik}A_{lj}^{(2)} + A_{ik}^{(2)}\delta_{jl}) - \frac{2}{3}\left(\frac{\gamma+2}{4\gamma-1} - 1\right)A_{kl}^{(2)}\delta_{ij} \right] S_{kl}. \quad (2.14)$$

For this model, the behaviour of a polycrystal with a perfect single-maximum fabric is the same as a single crystal.

Both eqs. (2.10) and (2.14) are linear ($n = 1$). While this may be reasonably valid for a single grain (Kamb, 1961), on the large scale ice is known to obey a power law relationship with $n \approx 3$ (Glen, 1952). A linear anisotropic flow law $S_{ij} = \mu_{ijkl}D_{kl}$ can be easily extended to incorporate power-law dependence, as well as temperature dependence $A(T)$ from Glen's law:

$$S_{ij} = (2A)^{-1/n} \dot{\gamma}^{\frac{1-n}{n}} \mu_{ijkl} D_{kl} \quad (2.15)$$

where μ_{ijkl} comes from eq. (2.10) or the inverse of eq. (2.14). This has been done by Martín et al. (2009).

2.2.2.3 General orthotropic linear flow law

Another anisotropic flow law, proposed in Gillet-Chaulet et al. (2005) is the General Orthotropic Linear Flow law (GOLF) This constitutive law derives a general expression for the viscosity based on the eigenvectors of $\mathbf{A}^{(2)}$. The constitutive law is:

$$\mu_{ijkl} = \eta_0 \sum_{r=1}^3 \left[\eta_r M_{ij}^{(r)} M_{kl}^{(r)} + \eta_{r+3} (\delta_{ik} M_{lj}^{(r)} + M_{ik}^{(r)} \delta_{jl}) - \frac{1}{3} (\eta_r + 2\eta_{r+3}) M_{kl}^{(r)} \delta_{ij} \right].$$

(2.16)

Here $\mathbf{M}^{(r)}$ ($r = 1, 2, 3$) is formed from the dyadic products of the eigenvectors of the second order orientation tensor (Gagliardini et al., 2013). In order to accurately represent micro-mechanical behaviour, the equation has six parameters η_r which are functions of the eigenvalues of the second-order orientation tensor. The values of each η_i are chosen to match the response found through smaller scale models which solve crystal dynamics directly, such as the visco-plastic-self-consistent model (Castelnau et al., 1996). Equation (2.16) has been extended to the non-linear case as in eq. (2.15) by Ma et al. (2010). A disadvantage of eq. (2.16) is that it does not depend on any higher order orientation tensor than $\mathbf{A}^{(2)}$, and hence detailed features in the fabric cannot be represented (this fact is discussed in detail in appendix A.1.1).

2.2.2.4 CAFFE flow law

Another flow law, which is not truly anisotropic, is proposed alongside the fabric evolution model in Placidi et al. (2010). This is the Continuum-mechanical, Anisotropic Flow model, based on an anisotropic Flow Enhancement factor (CAFFE). In contrast to the above flow laws, it does not attempt to represent any directional dependence in the viscosity, but instead proposes a fabric dependent softening parameter \hat{E} :

$$D_{ij} = A(T)\hat{E}(\mathcal{D})\tau_e^{n-1}S_{ij}, \quad (2.17)$$

where τ_e is the second invariant of \mathbf{S} , as in eq. (2.3). The enhancement factor is $\hat{E}(\mathcal{D})$ and \mathcal{D} called the macroscopic deformability and is defined as:

$$\mathcal{D} = \frac{5}{D_{mn}D_{nm}}D_{ij}D_{kl}(\delta_{ik}A_{jl}^{(2)} - A_{ijkl}^{(4)}), \quad (2.18)$$

so the enhancement factor is a function of the orientation tensors and the strain-rate tensor. Placidi et al., 2010 interprets \mathcal{D} as representing the normalised square of the stress on the basal plane.

The enhancement factor \hat{E} is chosen by Placidi et al. (2010) to have a dependency on \mathcal{D}^2 based on experimental results (Azuma, 1995):

$$\hat{E}(\mathcal{D}) = \begin{cases} (1 - E_{\min})\mathcal{D}^\tau + E_{\min}, & \mathcal{D} \in [0, 1] \\ (4\mathcal{D}^2(E_{\max} - 1) + 25 - 4E_{\max}) / 21 & \mathcal{D} \in [1, \frac{5}{2}], \end{cases} \quad (2.19)$$

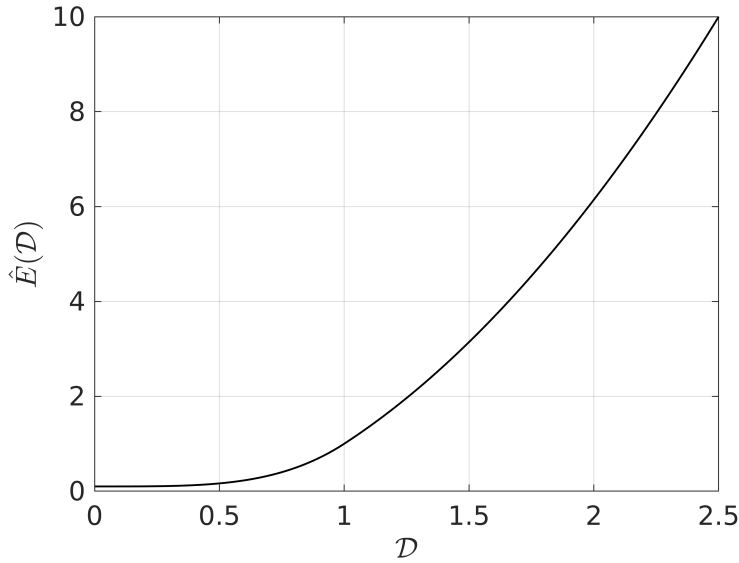


Figure 2.5: Plot of the enhancement factor $\hat{E}(\mathcal{D})$ in the CAFFE model, with $E_{max} = 10$ and $E_{min} = 0.1$

where $\tau = \frac{8}{21} \left(\frac{E_{max}-1}{1-E_{min}} \right)$. The parameter $E_{max} = 10$ is chosen match the maximum softening reported in ice (Budd and Jacka, 1989; Pimienta and Duval, 1987) and $E_{min} = 0.1$ is chosen as non-zero to avoid numerical problems. This is shown in fig. 2.5.

The advantage of eq. (2.17) is that it can be easily incorporated into existing ice-sheet flow models which use Glen's flow law. However, the flow law cannot distinguish between different fabric and deformation conditions which have the same value of \mathcal{D} . It also does not include any true anisotropy, i.e. any directional dependence in the viscosity.

2.2.3 Mathematical representations of the fabric

I now move onto mathematical descriptions of the fabric. These are required as inputs into the anisotropic flow laws in section 2.2.2. A general way to represent the fabric is to describe the distribution of c -axes within a polycrystal. This is termed the orientation distribution function. The orientation distribution function represents the volume fraction of the crystals in a polycrystal that are at a specific orientation (e.g. Gagliardini et al., 2009):

$$f^*(\mathbf{n})d\mathbf{n} = \frac{dV^*(\mathbf{n})}{V}, \quad (2.20)$$

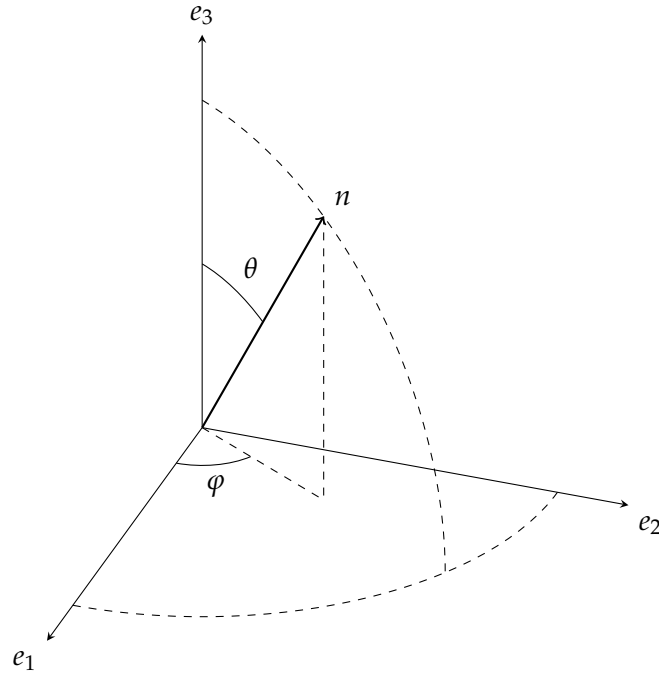


Figure 2.6: Schematic of orientation space. Each point on the unit sphere represents a specific orientation \mathbf{n}

where \mathbf{n} is the position vector on a unit sphere, illustrated in fig. 2.6 describing all possible orientations. In spherical coordinates, $\mathbf{n}(\theta, \varphi)$ is defined by:

$$\mathbf{n} = \sin \theta \cos \varphi \mathbf{e}_1 + \sin \theta \sin \varphi \mathbf{e}_2 + \cos \theta \mathbf{e}_3, \quad (2.21)$$

where θ is the polar angle, φ is the azimuthal angle and $\{\mathbf{e}_1, \mathbf{e}_2, \mathbf{e}_3\}$ is a fixed orthonormal basis. Throughout this thesis, quantities which vary with the unit orientation vector \mathbf{n} are denoted by an asterisk, with the exception of the spherical harmonics.

From eq. (2.20), it follows that:

$$\int_{S^2} f^*(\mathbf{n}) d\mathbf{n} = 1. \quad (2.22)$$

Placidi et al. (2010) uses a generalisation of the orientation distribution function to describe the mass fraction of grains with the solid angle \mathbf{n} :

$$\rho(\mathbf{x}, t) = \int_{S^2} \rho^*(\mathbf{x}, t, \mathbf{n}) d\mathbf{n}, \quad (2.23)$$

hence integrating ρ^* over the space of possible orientations gives the mass density of the ice at that point in space. Note $\rho^*/\rho = f^*$. When

describing a c -axis, the top is not distinguishable from the bottom. This leads to the symmetry:

$$\rho^*(\mathbf{n}) = \rho^*(-\mathbf{n}), \quad (2.24)$$

and similarly for f^* .

The orientation tensors, defined in terms of a physical average in eqs. (2.11) and (2.12), can also be defined from the continuum descriptions of the fabric which are defined above:

$$A_{ij}^{(2)} = \langle n_i n_j \rangle = \int_{S^2} \frac{\rho^*(\mathbf{n})}{\rho} n_i n_j \, d\mathbf{n}, \quad (2.25)$$

and

$$A_{ijkl}^{(4)} = \langle n_i n_j n_k n_l \rangle. \quad (2.26)$$

From eq. (2.22) and the symmetry in eq. (2.24) it follows that the second order orientation tensor is symmetric and positive definite with $A_{ii}^{(2)} = 1$, so there are only 5 independent components for the matrix $\mathbf{A}^{(2)}$. The second order orientation tensor does not provide a full description of the fabric. Different fabrics can have an identical $\mathbf{A}^{(2)}$. The higher-order orientations tensors will then be different. Nevertheless, it provides a good leading order description of the fabric. The eigenvalues of $\mathbf{A}^{(2)}$ are often used to describe ice fabrics, especially those drilled from ice cores. Equal eigenvalues imply an isotropic fabric. One eigenvalue larger than the other two implies a single-maxima (fig. 2.4a). Two large and equal eigenvalues imply a girdle fabric (fig. 2.4e).

2.2.4 Fabric evolution

2.2.4.1 Evolution of the orientation tensors

The common approach for modelling fabric evolution at large-scales is to derive an equation for the evolution of the orientation tensors. This can be done by considering the rotation of an individual grain such as in eq. (2.1) and making a Taylor assumption as in eq. (2.9) so the spin and strain-rate tensor at an individual grain are equal to the large scale spin and strain-rate tensors. Then, differentiating eq. (2.11) I obtain:

$$\frac{DA_{ij}^{(2)}}{Dt} = W_{ik}A_{kj}^{(2)} - A_{ik}^{(2)}W_{kj} - \iota \left(D_{ik}A_{kj}^{(2)} + A_{ik}^{(2)}D_{kj} - 2A_{ijkl}^{(4)}D_{kl} \right), \quad (2.27)$$

where $\mathbf{W} = \frac{1}{2}(\nabla \mathbf{u} - \nabla \mathbf{u}^T)$, the spin-rate or vorticity tensor, and $\mathbf{D} = \frac{1}{2}(\nabla \mathbf{u} + \nabla \mathbf{u}^T)$ is the strain-rate tensor as before. As can be seen in eq. (2.27), in order to calculate $A^{(2)}$ one needs to know $A^{(4)}$, while if one derives an equation for $\frac{DA^{(4)}}{Dt}$ as in Advani and Tucker (1987) then an expression for $A^{(6)}$ is required and so on. To prevent an infinite series of orientation tensor evolution equations, closure approximations are used to approximate higher order orientation tensors in terms of lower order ones. Many different closure approximations have been proposed (Chung and Kwon, 2002; Cintra and Tucker, 1995; Jack and Smith, 2005) and there have been comparisons of their accuracy (Altan and Tang, 1993).

It is possible to incorporate rotational recrystallization into eq. (2.27). The fabric evolution model in Elmer/ICE, originally described in (Gagliardini et al., 2013) and more recently by Lilien et al. (2021) is implemented as:

$$\begin{aligned} \frac{DA_{ij}^{(2)}}{Dt} = & W_{ik}A_{kj}^{(2)} - A_{ik}^{(2)}W_{kj} - \left(C_{ik}A_{kj}^{(2)} + A_{ik}^{(2)}C_{kj} - 2A_{ijkl}^{(4)}C_{kl} \right) \\ & + \lambda \exp \frac{\log(10)T}{10} (\delta_{ij} - 3A_{ij}^{(2)}) \|\mathbf{C}\|_2, \end{aligned} \quad (2.28)$$

where λ is a parameter, $\|\cdot\|_2$ is the second-invariant and \mathbf{C} represents a blend between strain-rate and stress:

$$\mathbf{C} = (1 - \alpha)\mathbf{D} + \alpha k_s \mathbf{D}_{\text{glen}} \quad (2.29)$$

where typical values are $\alpha = 0.06$, $k_s = 10$ and \mathbf{D}_{glen} is the strain-rate predicted by the isotropic Glen's flow law for a given deviatoric stress (eq. (2.3)). The tensor \mathbf{C} was first proposed by Gillet-Chaulet et al. (2006), and is designed to homogenise the stress and strain over a polycrystal when determining the fabric evolution.

Equation (2.28) represents the state-of-the-art for fabric evolution in large-scale ice-sheet models. The term $W_{ik}A_{kj}^{(2)} - A_{ik}^{(2)}W_{kj}$ represent the effect of rotation on the fabric. The term $\left(C_{ik}A_{kj}^{(2)} + A_{ik}^{(2)}C_{kj} - 2A_{ijkl}^{(4)}C_{kl} \right)$ represents the effect of basal-slip deformation. The final term in eq. (2.28) can represent rotational recrystallization. However eq. (2.28) is incapable of representing migration recrystallization as this process acts to produce features in the fabric pattern more detailed than the 2nd-order orientation tensor can represent.

2.2.4.2 Fabric evolution from Placidi et al. (2010)

Placidi et al. (2010) includes both a model for fabric evolution, and a fabric-dependent flow law. Here I cover the fabric evolution model extensively as it is the basis for much of the work in this thesis. The fabric evolution model is:

$$\frac{\partial \rho^*}{\partial t} + \mathbf{u} \cdot \nabla \rho^* = -\nabla^* \cdot (\rho^* \mathbf{v}^*) + \lambda \nabla^{*2}(\rho^*) + \beta(\mathcal{D}^* - \langle \mathcal{D}^* \rangle) \rho^*, \quad (2.30)$$

where λ and β (originally $\hat{\Gamma}$ in Placidi et al. (2010)) are parameters which are left unconstrained by Placidi et al. (2010). Here, ∇^* is the gradient operator in orientation space defined by:

$$\nabla^* \mathbf{v}^* = \frac{\partial \mathbf{v}^*}{\partial \mathbf{n}} - \left(\frac{\partial \mathbf{v}^*}{\partial \mathbf{n}} \cdot \mathbf{n} \right) \mathbf{n} = \frac{\partial v_i^*}{\partial n_j} - \frac{\partial v_i^*}{\partial n_l} n_l n_j, \quad (2.31)$$

which is the gradient operator restricted to the surface of a sphere. The parameters λ and β represent the rates of rotational recrystallization and grain-boundary migration, respectively. The orientationally dependent term \mathcal{D}^* will be defined below in eq. (2.33). The term \mathbf{v}^* defines the orientation transition rate:

$$v_i^* = W_{ij} n_j - \iota (D_{ij} n_j - n_i n_j n_k D_{jk}), \quad (2.32)$$

which is similar to eq. (2.1). The term $W_{ij} n_j$ in eq. (2.32) represents the effect of vorticity on the fabric. The second term models basal-slip deformation. The non-dimensional parameter ι represents the ratio of basal-slip deformation to rigid-body rotation. Unlike in eqs. (2.1), (2.27) and (2.28) ι is free to take values greater than 1.

The parameter λ (s^{-1}) represents the rate of rotational recrystallization, which can be modelled by a diffusion in orientation space (Gödert, 2003). Migration recrystallization is modelled by an orientation-dependent source term, with the rate controlled by β (s^{-1}). The orientation dependence is governed by the deformability, defined by:

$$\mathcal{D}^* = 5 \frac{(D_{ij} n_j)(D_{ik} n_k) - (D_{ij} n_j n_i)^2}{D_{mn} D_{nm}}. \quad (2.33)$$

Placidi et al. (2010) give the physical interpretation of \mathcal{D}^* as the (normalised) square of the shear strain rate resolved onto the basal plane. Because ice deforms primarily by basal slip, the resolved shear rate on the basal plane also drives the accumulation of deformation

energy in the physical grain, which drives migration recrystallization. The average of \mathcal{D}^* is defined as:

$$\mathcal{D} = \langle \mathcal{D}^* \rangle = \int_{S^2} \frac{\rho^*}{\rho} \mathcal{D}^* dn. \quad (2.34)$$

This is the macroscopic deformability used in eq. (2.17). If \mathcal{D}^* is greater than the average value $\langle \mathcal{D}^* \rangle$ then ρ^* at that orientation will increase, as implied by the final term on the right hand side of eq. (2.30). This corresponds to grains growing or nucleating with this orientation. Note that the total production and consumption of \mathcal{D}^* always balance. The factor of 5 in eq. (2.33) is a convention.

Equation (2.30) incorporates the net effects of grain-to-grain interactions through parameterisations. This is similar to other continuum approaches, for example how explicit descriptions of particle interactions are not included in the Stokes equations, yet are satisfactorily modelled statistically through parameterisation in the form of a constitutive relation.

The underpinning theory for eq. (2.30) was proposed previously by Faria (2001) and Faria (2006). Grains with the same orientations are called a *species*. There has been discussion in the literature (Faria et al., 2008; Gagliardini, 2008) on whether this theory implicitly includes a *Taylor assumption* (that all ice grains forming the polycrystal experience the same strain-rate) As discussed in section 2.2.2.2 this has been shown not to be valid for ice (Castelnau et al., 1996). To summarise this debate, Gagliardini (2008) suggests that the assumption in Faria (2006) that the strain-rate of a species is independent of orientation is equivalent to every grain undergoing the same deformation (a Taylor assumption). However, Faria et al. (2008) rejected this assertion and replied that this assumption only requires that grains move with the surrounding material, with no direct constraint on the individual deformation of grains. In accordance with the continuum approach, the net effect of deformations on individual grains, which can vary from grain to grain, is incorporated via parameterisations of the overall net effect of these interactions. Therefore, the theory of Faria (2006), and consequently eq. (2.30) does not impose a Taylor assumption on the grain deformation. However, care should be taken in attributing and parameters in the model as applying specifically to grain-to-grain interactions, rather than the bulk interactions representing their net statistical effect on the distribution function.

Despite the model not including the Taylor hypothesis, the term for basal-slip deformation in eq. (2.32) is similar to that which would be derived from a Taylor homogenisation of ice under a simple basal-slip only model, as was done for eq. (2.27). The difference is that the rate of basal-slip deformation, controlled by ι , can vary freely.

This fabric evolution model has multiple advantages when compared to modelling the evolution of $\mathbf{A}^{(2)}$ defined in eq. (2.27). Firstly it incorporates migration recrystallization, which has a leading order effect on the fabric pattern. Secondly, it is capable of reproducing much more detailed fabric patterns as it describes the orientation space by a continuous function, rather than 5 independent tensor components. However, because of this, it is harder to solve. Furthermore, the parameters (λ, β, ι) are still unconstrained. Until these parameters are quantified, the model cannot be used to predict ice fabrics.

THE EVOLUTION OF ICE FABRICS: A CONTINUUM MODELLING APPROACH VALIDATED AGAINST LABORATORY EXPERIMENTS

ABSTRACT

There remains a significant challenge to model ice crystal fabrics both accurately and efficiently within ice-sheet models. I develop the first fully constrained continuum model, validated against experiments, able to predict the evolution of a crystal fabric for any flow field or temperature. For this, I apply a mesoscopic continuum model describing the evolution of a mass distribution function of c -axis orientations. The model assumes that ice deforms by dislocation creep with slip primarily along the basal plane, and incorporates the effects of rigid body rotation, migration recrystallization and rotational recrystallization. I solve the model using a new spectral method, which is computationally highly efficient. By constraining the model parameters using data from laboratory experiments in simple shear, I provide the first estimates of two fundamental dimensionless parameters controlling the importance of different recrystallization processes as a function of temperature, as well as the first constraints on the strain-rate dependence of these parameters. With no further fitting, I apply the model to the case of compression, yielding excellent quantitative agreement with observed fabrics from corresponding experiments. The combination of the model, the spectral method and the parameter constraints as functions of temperature provide accurate and efficient predictions of ice crystal fabric evolution for general deformations, temperatures and strain-rates. The model-solver (SpecCAF) can, in principle, be extended to other important polycrystalline materials including olivine, the key material in mantle dynamics.

This chapter is based on a published paper, Richards et al. (2021b). The chapter has been edited to fit coherently within the thesis. In particular, much of the background and description of the model details in Richards et al. (2021b) has been moved to chapter 2.

3.1 INTRODUCTION

Understanding ice fabrics is key for interpreting processes in the ice-sheet and they are an important control on the rheology (Minchew et al., 2018) through the induced viscous anisotropy. However, even state-of-the-art ice-sheet models (Gagliardini et al., 2013) either neglect the effects of crystal anisotropy or apply a low resolution or unconstrained model for fabric evolution that neglects the key process of recrystallisation. Discrete models that solve for the microstructure directly have also been developed and analysed (Montagnat et al., 2014a). However, these are both computationally expensive and can fail to produce certain features of ice fabric. There is a need for a reliable, constrained and computationally inexpensive model that can be integrated into large-scale ice-sheet models.

Many laboratory experiments have been performed to investigate fabric development: in uniaxial compression (Craw et al., 2018; Fan et al., 2020; Jacka, 2000; Jacka and Maccagnan, 1984; Montagnat et al., 2015; Piazzolo et al., 2013; Qi et al., 2017; Vaughan et al., 2017) and simple shear (Journaux et al., 2019; Qi et al., 2019). This provides a large set of measurements at a range of temperatures, strains and strain-rates that could be used to benchmark new models and constrain their underlying parameters.

At a theoretical level, there are also several remaining open questions regarding the development of fabrics in ice. At the microscopic scale, there is still uncertainty over which slip systems and modes of recrystallization are key for producing the fabric patterns observed in nature and the laboratory (Qi et al., 2019). Furthermore, there is only a qualitative, not quantitative, understanding of the importance of different recrystallization processes at different temperatures (Piazzolo et al., 2013). The essential effect of strain-rate on the fabric remains an area of ongoing research (Wilson et al., 2019)

Here, I use a continuum model based on the CAFFE model (Placidi et al., 2010), described in section 2.2.4.2, to model the mass distribution of crystal orientations, which I solve using a spectral method (Montgomery-Smith et al., 2010), originally developed for fibre flows. By solving the inverse problem for the model parameters, I provide the first quantification of the magnitudes of different processes as functions of temperature. This combination provides a fully constrained continuum model for modelling the ice fabric, across a range of temperatures and deformations.

The closest previous work to this chapter is Bargmann et al. (2012). They used the CAFFE model (Placidi et al., 2010) with rotational and migration recrystallization to model the evolution of ice fabric at an ice divide. The model was implemented using a finite-volume method. They found good agreement up to intermediate depths, before encountering instabilities in their numerical model. In compression, their scheme reproduced cone-shape fabrics, but was unable to reproduce a secondary cluster in shear due to the numerical instabilities. They provided order of magnitude estimates for the model parameters.

3.2 MODEL DETAILS

To model the fabric I use the continuum approach of Faria (2006) and Placidi et al. (2010), described extensively in section 2.2.4.2. The model tracks quantities over both macroscopic space \boldsymbol{x} and orientation space \boldsymbol{n} .

3.2.1 Evolution equation

I use the fabric evolution equation from Placidi et al. (2010), first defined in eq. (2.30), which I repeat here:

$$\frac{\partial \rho^*}{\partial t} + \boldsymbol{u} \cdot \nabla \rho^* = -\nabla^* \cdot [\rho^* \boldsymbol{v}^*] + \lambda \nabla^{*2}(\rho^*) + \beta(\mathcal{D}^* - \langle \mathcal{D}^* \rangle) \rho^*.$$

I refer the reader to section 2.2.4.2, where I described the terms of this equation and their physical meaning extensively, along with discussion of the assumptions.

Since the parameters λ and β represent recrystallization rates, they can be expected to be functions of temperature (Wilson et al., 2019) and strain-rate (Piazolo et al., 2013). To date, the only determination of these parameters is an order of magnitude estimate given by Bargmann et al. (2012), without any temperature or strain-rate dependence. In this chapter I will determine the first detailed constraints on these functions using experimental data from compression and simple shear deformations of ice, and show that the resulting model produces all existing experimental observations spanning different deformation regimes and temperatures.

Equation (2.30) can be used to predict fabric evolution. Unlike models that solve for the microstructure directly, this equation can be applied readily to any velocity field, and is computationally cheap

enough to be incorporated into large-scale ice-sheet models. However, the accuracy of this method is dependent on correctly including the magnitudes of the terms modelling recrystallization, which I will come to later.

3.2.2 Non-dimensionalisation

To apply eq. (2.30) to spatially homogeneous fabrics and to compare to fabrics deformed in the laboratory. I non-dimensionalise by a characteristic density ρ_0 and strain-rate, which I define in this case as:

$$\dot{\gamma} = \sqrt{D_{ij}D_{ij}}. \quad (3.1)$$

Note this strain-rate $\dot{\gamma} = \sqrt{2}\dot{\gamma}_{\text{eff}}$, the effective strain-rate used in the definition of eq. (2.4) and later in this thesis. I choose this because it gives a direct correspondence to the experimental strains. I assume the fabric is spatially homogeneous, so the term $\mathbf{u} \cdot \nabla \rho^*$ can be neglected. The non-dimensional variables are represented with tildes and are defined as:

$$\begin{aligned} \tilde{\rho}^* &= \frac{\rho^*}{\rho_0}, & \tilde{\mathbf{D}} &= \frac{\mathbf{D}}{\dot{\gamma}}, & \tilde{\mathbf{W}} &= \frac{\mathbf{W}}{\dot{\gamma}} \\ \tilde{\lambda}(T, \dot{\gamma}) &= \frac{\lambda(T, \dot{\gamma})}{\dot{\gamma}}, & \tilde{\beta}(T, \dot{\gamma}) &= \frac{\beta(T, \dot{\gamma})}{\dot{\gamma}}. \end{aligned}$$

Recasting eq. (2.30) in terms of the non-dimensional variables above, I obtain:

$$\frac{\partial \tilde{\rho}^*}{\partial \tilde{t}} = -\nabla^* \cdot [\tilde{\rho}^* \tilde{\mathbf{v}}^*] + \tilde{\lambda} \nabla^{*2}(\tilde{\rho}^*) + \tilde{\rho}^* \tilde{\beta}(\mathcal{D}^* - \langle \mathcal{D}^* \rangle), \quad (3.2)$$

where

$$\tilde{\mathbf{v}}_i^* = \tilde{W}_{ij}n_j - \iota[\tilde{D}_{ij}n_j - n_in_jn_k\tilde{D}_{jk}].$$

is the non-dimensional form of the orientation transition rate (eq. (2.32)). The governing equation depends on three dimensionless parameters. Physically, $\tilde{\lambda}$ represents the ratio of the rate of rotational recrystallization to the strain-rate, and $\tilde{\beta}$ represents the ratio of the rate of migration recrystallization to the strain-rate. The ratio of basal-slip deformation to rigid-body rotation, $\iota(T)$ is already non-dimensional so is not modified. The non-dimensional time is $\tilde{t} = \dot{\gamma}t$.

3.3 SPECTRAL METHOD

Equation (3.2) is challenging to solve directly due to the differential operators on the surface of a sphere. In this section I describe a new spectral model, adapted from work by Montgomery-Smith et al. (2010) for fibre flows. The spectral method converts the partial differential equations over orientation space into a system of ordinary differential equations through the use of spherical harmonics. An overview of the spherical harmonics and their application to solving partial differential equations is given in appendix A. This method allows eq. (3.2) to be solved with high precision and computational efficiency.

The orientation mass density can be represented in terms of the spherical harmonics:

$$\rho^*(\mathbf{x}, t, \mathbf{n}) = \sum_{l=0}^{\infty} \sum_{m=-l}^l \hat{\rho}_l^m(\mathbf{x}, t) Y_l^m(\theta, \varphi), \quad (3.3)$$

where Y_l^m are spherical harmonic functions as defined in eq. (A.1). The weak form of eq. (3.2) can be found by integrating over the surface of the sphere and multiplying by the complex conjugate \bar{Y}_l^m , as in eq. (A.5):

$$\frac{\partial}{\partial t} \int_{S^2} \rho^* \bar{Y}_l^m = \int_{S^2} \nabla^* \cdot (\rho^* \mathbf{v}^*) \bar{Y}_l^m + \lambda \nabla^{*2} \rho^* \bar{Y}_l^m + \beta (\mathcal{D}^* - \langle \mathcal{D}^* \rangle) \rho^* \bar{Y}_l^m \, d\mathbf{n}. \quad (3.4)$$

The next step is to apply integration by parts to eq. (3.4). Integration by parts has a different form over the surface of a sphere:

$$\int_{S^2} \mathbf{f}^* \cdot \nabla^* g^* \, d\mathbf{n} = \int_{S^2} (\nabla^* \cdot (I - \mathbf{n}\mathbf{n}^T) \cdot \mathbf{f}^*) g^* \, d\mathbf{n} = \int_{S^2} ((2\mathbf{n} - \nabla^*) \cdot \mathbf{f}^*) g^* \, d\mathbf{n}. \quad (3.5)$$

I use eq. (3.5) to rearrange eq. (3.4) so the differential operator acts on \bar{Y}_l^m . For the left hand side of eq. (3.4) (the time derivative), I also replace ρ^* with the spherical harmonic expansion (eq. (3.3)) and, as this term has no multiplication or differentiation by components of \mathbf{n} , calculate the overlap integrals between $Y_{l'}^{m'}$ and \bar{Y}_l^m using eq. (A.3):

$$\frac{\partial}{\partial t} \hat{\rho}_l^m = \int_{S^2} ((2\mathbf{n} - \nabla^*) \bar{Y}_l^m) \cdot \mathbf{v}^* \rho^* + \beta (\mathcal{D}^* - \langle \mathcal{D}^* \rangle) \rho^* \bar{Y}_l^m \, d\mathbf{n} - \lambda l(l+1) \hat{\rho}_l^m. \quad (3.6)$$

Here I have also used the identity $\nabla^{*2}Y_l^m = -l(l+1)Y_l^m$ (eq. (A.6)) to simplify the rotational recrystallization term. The advantage of this form is that differentiation and multiplication by \mathbf{n} on \tilde{Y}_l^m can be represented as multiplications by other moments of the spherical harmonics through recursive application of the formulae in appendix A.1. Montgomery-Smith et al. (2010) provide an algorithm which recursively applies the identities in eqs. (A.12) to (A.14) to allow eq. (3.6) to be rewritten as a series of ordinary differential equations:

$$\frac{\partial}{\partial t}\hat{\rho}_l^m = \sum_{l'=0}^{\infty} \sum_{m'=-l'}^{l'} C_{l,l'}^{m,m'} \hat{\rho}_{l'}^{m'}. \quad (3.7)$$

For example, the first term in the deformability \mathcal{D}^* is:

$$D_{ij}n_j D_{ik}n_k = D_{11}^2 n_x^4 + D_{22}^2 n_y^4 + \dots \text{ (21 terms in total)}. \quad (3.8)$$

When this term is multiplied by \tilde{Y}_l^m in eq. (3.6) the aforementioned algorithm from Montgomery-Smith et al. (2010), using the identities in appendix A.1 to express operations by n_x, n_y, n_z and $\frac{\partial}{\partial n_x}, \frac{\partial}{\partial n_y}, \frac{\partial}{\partial n_z}$ in terms of other terms in the spherical harmonic expansion, can be applied recursively. Here I give a partial example by taking the first term in eq. (3.8):

$$D_{11}^2 n_x^4 \tilde{Y}_l^m = D_{11}^2 n_x^3 (n_z iL_y (\tilde{Y}_l^m) - iL_y (n_z \tilde{Y}_l^m)). \quad (3.9)$$

Expanding again only one term in the above:

$$\begin{aligned} n_z iL_y (\tilde{Y}_l^m) &= \frac{n_z}{2} (L_+ (\tilde{Y}_l^m) - L_- (\tilde{Y}_l^m)) \\ &= \frac{n_z}{2} (\sqrt{(l+m)(l-m+1)} \tilde{Y}_l^{m-1} - \sqrt{(l-m)(l+m+1)} \tilde{Y}_l^{m+1}), \end{aligned} \quad (3.10)$$

then again only taking the first term and applying Rodrigues' formula from eq. (A.7):

$$\begin{aligned} \frac{n_z}{2} \sqrt{(l+m)(l-m+1)} \tilde{Y}_l^{m-1} &= \\ \frac{1}{2} \sqrt{(l+m)(l-m+1)} \left(\sqrt{\frac{(l+m-1)(l-m+1)}{(2l-1)(2l+1)}} Y_{l-1}^{m-1} + \sqrt{\frac{(l+m)(l-m)}{(2l+1)(2l+3)}} \tilde{Y}_{l+1}^{m-1} \right). \end{aligned} \quad (3.11)$$

Thus through eqs. (3.9) to (3.11) we have (partially) transformed multiplying by n_x to a linear combination of the other spherical harmonics.

Once this has been done the orthogonality of the spherical harmonics (eq. (A.3)) can be used. This process must be applied recursively to all the terms in eq. (3.6). Clearly this is quite laborious but Montgomery-Smith et al. (2010) provides an algorithm and code to use the identities described in appendix A.1 to generate the terms in eq. (3.7) from any partial differential equation.

In the results, I truncate the outer summation in eq. (3.7) at $l' = L$, where L is a positive even integer representing the number of harmonics used. A comparison of the truncation error for different values of L is given in appendix B.1. As described in appendix A.1.1, truncating at L gives the same precision as solving the evolution equation for the L th-order orientation tensor.

3.4 RESULTS

I first use the unconstrained model to illustratively show the fabrics produced in different deformation regimes in section 3.4.1. I then calibrate the free parameters in the model by comparing the output to laboratory experiments of ice deformed in uniaxial compression and simple shear. I run the model with $L = 12$ and using a Runge-Kutta scheme for the time integration.

3.4.1 General forms of the fabric

I begin with an overview of the fabrics produced by the unconstrained model in four different modes of deformation. Figure 3.1 shows both sketched pole figures and predicted pole figures obtained from the unconstrained model for each form of deformation at a true strain of $\gamma = 0.7$. Panels (a)-(d) of fig. 3.1 illustrate the typical fabrics predicted by the model, with and without migration recrystallization, under respectively: uniaxial compression ($\nabla \tilde{\mathbf{u}} = \text{diag}(0.5, 0.5, -1)$), pure shear ($\nabla \tilde{\mathbf{u}} = \text{diag}(1, 0, -1)$), uniaxial extension ($\nabla \tilde{\mathbf{u}} = \text{diag}(1, -0.5, -0.5)$), and simple shear,

$$\nabla \tilde{\mathbf{u}} = \begin{bmatrix} 0 & 0 & 1 \\ 0 & 0 & 0 \\ 0 & 0 & 0 \end{bmatrix}.$$

The colour in the pole figures represents the magnitude of $\tilde{\rho}^*$ at that orientation. The pole figure is plotted with an azimuthal equidistant projection. For these examples, illustrative values of $\tilde{\lambda} = 0.03$, $\iota = 1$

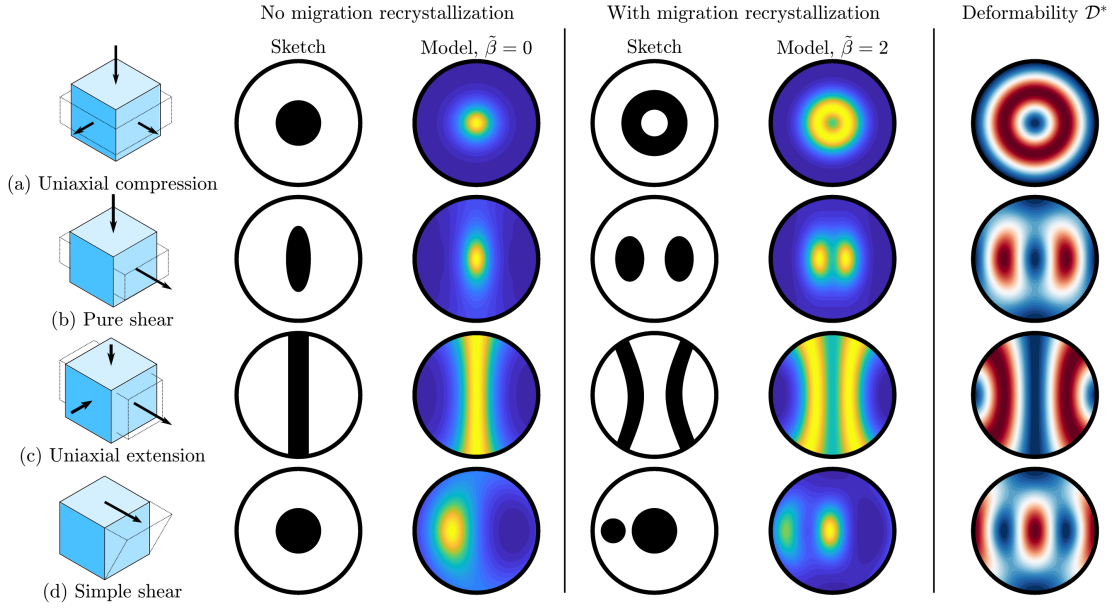


Figure 3.1: Comparison of the pole-figures produced by the model, compared to sketches of expected pole figures, based on experimental observations and ice core samples (Paterson, 1999). Each row represents a different deformation. Comparison between the expected sketch and the model are presented for both no migration recrystallization, ($\tilde{\beta} = 0$), and with migration recrystallization, for the illustrative case of $\tilde{\beta} = 2$. Other parameter values chosen were $\tilde{\lambda} = 0.05$ and $\iota = 1$. The model pole figures are plotted at true strain $\gamma = 0.7$. The final column shows a plot of the deformability, \mathcal{D}^* from eq. (2.33), which controls migration recrystallization.

and $\tilde{\beta} = 0$ or 2 were used. The right-hand column shows a pole figure of the deformability, \mathcal{D}^* , highlighting which orientations are favoured for grain growth by migration recrystallization.

In uniaxial compression (fig. 3.1a) without migration recrystallization, basal-slip deformation produces a single-maximum fabric towards the axis of compression. For this deformation, migration recrystallization acts to produce crystals orientated at 45° to the z-axis, and consume grains orientated otherwise. The balance of this process and deformation produces a cone-shape fabric with a cone angle $< 45^\circ$. The model produces the expected single-maximum or cone-shape

fabric, depending on the value of $\tilde{\beta}$ controlling migration recrystallization.

For pure shear (fig. 3.1b), the single maximum is elongated without migration recrystallization, and this feature is present in the model. With migration recrystallization, instead of a cone-shape seen in fig. 3.1a, two separate maxima develop, which can be seen in both the sketch and the model.

For uniaxial extension (fig. 3.1c) the model again agrees with the expected sketched pole figures. Without migration recrystallization, a girdle fabric (fig. 2.4e) is produced in the yz -plane. A girdle fabric is one in which all the crystal orientations lie on a single plane, and the pattern in the pole looks like a girdle. Migration recrystallization transforms this into a cone-shape fabric with the axis of the cone in the x -direction.

Simple shear, shown in fig. 3.1d, is the only flow with non-zero vorticity, so the orientation transition rate contains contributions from both rigid-body rotation and basal-slip deformation. The model predicts a single maximum orientated at a certain angle slightly offset from the shear plane, set by the balance between vorticity and basal-slip deformation. The sketch from observations however, shows a single-maximum with no offset. Migration recrystallization produces orientations towards the z and x directions. The cluster at the z -axis is sustained by a balance between vorticity moving it to the right, basal-slip deformation moving to the left and migration recrystallization acting as a source term. For the cluster orientated towards the $-x$ -axis, vorticity and deformation both act to move it in the same direction. Once these grains are no longer orientated towards the x -axis migration recrystallization causes grains more favourably orientated, i.e. those towards the x or z -axes, to consume them. This results in the secondary cluster gradually weakening.

3.4.2 Strain-rate dependence

I now investigate the strain-rate dependence of the ice fabric development. I investigate how key measures of the fabric: both λ_1 , the largest eigenvalue of $\mathbf{A}^{(2)}$, and J , a measure of total fabric concentration:

$$J = \int_{S^2} (\tilde{\rho}^*)^2 d\mathbf{n}, \quad (3.12)$$

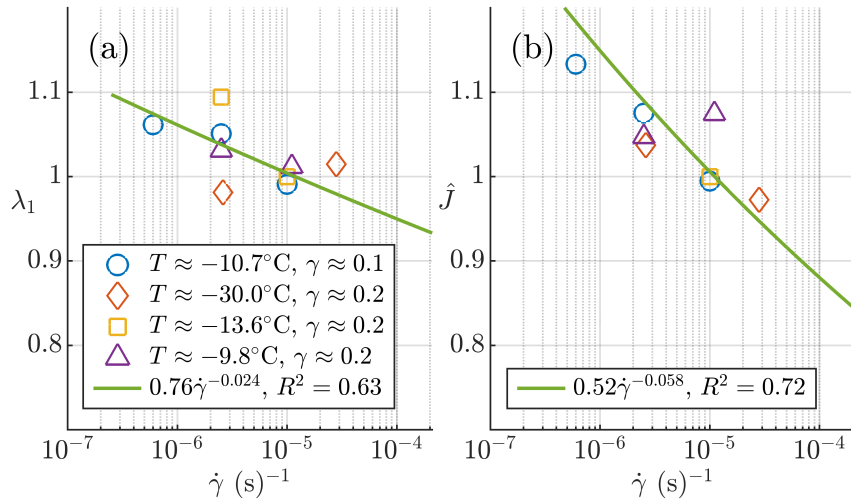


Figure 3.2: This figure shows the strain-rate dependence of experimental fabrics in uniaxial (unconfined) compression. The plots show two measures of fabric concentration for this flow field, λ_1 , the largest eigenvalue of $\mathbf{A}^{(2)}$ (a), and \hat{J} (b), against experimental data (Craw et al., 2018; Piazzolo et al., 2013). For each data set, in order to identify the strain-rate dependence, the values have been sorted into bins with roughly equal temperature ($\pm 1^\circ\text{C}$) and strain (± 0.025). The hats that indicate the values have been normalised against the value at $\dot{\gamma} = 10^{-5}$ in order to collapse different bins onto a single curve. A fit is also shown along with the R^2 value of the fit.

change with strain-rate. These changes are shown in fig. 3.2 for experiments in uniaxial compression (Craw et al., 2018; Piazzolo et al., 2013). For temperatures and strains at which there are multiple experiments the data has been sorted into bins and normalised by the value at $\dot{\gamma} = 2.5 \times 10^{-6} \text{ s}^{-1}$. This allows the results from experiments performed at different temperatures and strains to collapse onto a single curve and, to first approximation, a power-law fit to be performed. As can be seen from fig. 3.2 and the value of the derive power law exponents, both λ_1 and J depend very weakly on strain-rate. For example, the value of λ_1 varies by only $\sim 12\%$ over two orders of magnitude variation in strain-rate. This highlights how the fabric has only a very weak dependence on strain-rate.

I can extend the hypothesis of modelling the strain-rate dependence by a power law to the recrystallization parameters:

$$\begin{aligned} \lambda &\propto \dot{\gamma}^a, & \tilde{\lambda} &\propto \dot{\gamma}^{a-1} \\ \beta &\propto \dot{\gamma}^b, & \tilde{\beta} &\propto \dot{\gamma}^{b-1}. \end{aligned} \quad (3.13)$$

Based on the weakness of the strain-rate dependence in fig. 3.2 it is safe to assume that to leading order $a, b = 1$ in eq. (3.13). This means the fabric and non-dimensional parameters can be assumed to be independent of strain-rate (for ranges typical of experiments).

3.4.3 Inversion for parameters in simple shear

Based on the assumed strain-rate independence above, I henceforth assume that the three non-dimensional parameters in the model $(\tilde{\lambda}, \tilde{\beta}, \iota)$ are functions of temperature only. To provide a first quantification of this dependence, I apply a regression to invert the model for the parameters $(\tilde{\lambda}, \tilde{\beta}, \iota)$ which give the best fit at specific temperatures in simple shear experiments (Journaux et al., 2019; Qi et al., 2019). Once these parameters are constrained for this case, I use them to compare the model to experimental data in compression, thereby checking the predictive accuracy of the model for generalised deformations without any further fitting.

Qi et al. (2019) deformed ice cores in direct simple shear. The ice had an initially isotropic fabric and was deformed at temperatures of -30°C , -20°C and -5°C , at a constant strain-rate of $1 \times 10^{-4} \text{ s}^{-1}$ up to strains of $\gamma = 2.6$. They found the development of a secondary cluster in all experiments except at high strain and -30°C . They hypothesise these patterns arise from the balance between basal-slip deformation and migration recrystallization.

Journaux et al. (2019) ran similar experiments, but deformed the ice in torsion at $T = -7^\circ\text{C}$ and a mean $\dot{\gamma} = 1.14 \times 10^{-6} \text{ s}^{-1}$ over a range of strains. This still produces the same simple shear velocity gradient.

In order to invert for the model parameters $\tilde{\lambda}, \tilde{\beta}, \iota$ as functions of temperature I fitted the model to the fabrics from simple shear experiments. I minimised the total difference in the unique components of the fourth-order orientation tensor, between the model and experiments. Data from -20°C in Qi et al. (2019) was not included as only 2 experiments were performed at this temperature, so it is difficult to constrain the parameter set. Once the parameters $\tilde{\lambda}, \iota, \tilde{\beta}$ were found over a range of temperatures I performed a linear regression to give

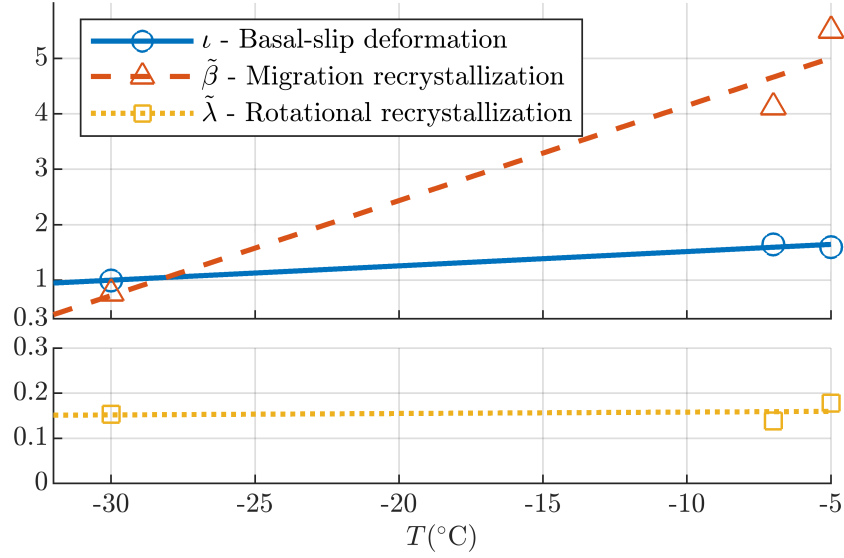


Figure 3.3: Plot of the parameters $\tilde{\lambda}$ (rotational recrystallization), $\tilde{\beta}$ (migration recrystallization) and ι (basal-slip deformation) found from the inversion described in section 3.3 at three temperatures: -30 , -7 , -5°C . The inverted-for parameters are shown as points along with a linear regression from these points for each parameter. A linear regression gave the best fit to results at -20°C , this is discussed in section 3.5.1. Note the broken y-axis as the parameter $\tilde{\lambda}$ changes much less than ι and $\tilde{\beta}$.

the parameters as functions of temperature, which is plotted in fig. 3.3. Although an Arrhenius profile was expected, a linear fit gave the best predictions at intermediate temperatures (in fig. 3.4) of $\approx -20^\circ\text{C}$. This is discussed in section 3.5.1. The parameters ι and $\tilde{\beta}$ both increase with temperature, suggesting increased basal-slip deformation and migration recrystallization. However, rotational recrystallization, controlled by $\tilde{\lambda}$, is fairly constant.

Figure 3.4 shows a comparison of the model and experiments in both simple shear and uniaxial compression. As an initial condition I assume an isotropic fabric, i.e. $\tilde{\rho}^* = \frac{1}{4\pi}$ everywhere. The parameters at each temperature were calculated from the linear regression in fig. 3.3. There is excellent agreement between the model and experiments, across flow states, temperature and strain-rate. The plot on the left shows the largest two eigenvalues of the second-order orientation tensor. The numbered experiments are plotted as pole figures,

alongside a pole figure extracted from the model at the same strain. The experimental strain-rates are visualised by the size of the circles. The results demonstrate the ability of the model to accurately predict fabric evolution in different flow states and its strong dependence on temperature.

For simple shear in fig. 3.4a the plot of the largest two eigenvalues of $\mathbf{A}^{(2)}$ against shear strain γ shows the largest eigenvalue increasing, corresponding to the cluster orientated towards the z-axis. The model accurately tracks the evolution seen in the experiments, including for the simulation at $T = -20^\circ\text{C}$ which was not used in the inversion.

I am able to accurately reproduce the experimental fabrics across a range of temperatures and strain-rates. The model accurately reproduces a secondary cluster, commonly seen at lower strains such as experiment (3), (5), and (7) in fig. 3.4a. At higher strains the secondary cluster tends to disappear, such as in (4) and (6), and this is also seen in the model.

The data for -7°C is from Journaux et al. (2019). As can be seen from the size of the circles in fig. 3.4a, these experiments were performed at a lower strain-rate ($\dot{\gamma} = 10^{-7}$ - 10^{-6} s^{-1}). Despite the multiple orders of magnitude difference in strain-rate from Qi et al. (2019) the model and parameters, without strain-rate dependence, still agree excellently with experimental results.

3.4.4 *Extrapolation to compression*

To test the model in a different flow field it was run in uniaxial compression. The parameters $(\tilde{\lambda}, \tilde{\beta}, \iota)$ were taken from the linear regression performed in simple shear (fig. 3.3). The comparison to experiments was performed by taking results from Craw et al. (2018) and Piazzolo et al. (2013). Note Piazzolo et al. (2013) used D_2O ice, hence the temperatures have been converted based on the difference in melting points (Ossipyan and Petrenko, 1988). The experiments are over a greater variety of strain-rates ranging from $\dot{\gamma} = 6 \times 10^{-7} \text{ s}^{-1}$ to $\dot{\gamma} = 2.4 \times 10^{-4} \text{ s}^{-1}$.

The comparison between the model and experiments is shown in fig. 3.4b. For uniaxial compression I plot the largest two eigenvalues of $\mathbf{A}^{(2)}$ against true axial strain ϵ . The growth of the largest eigenvalue represents the concentration of orientation towards the z-axis. The presence of a cone-shape fabric cannot be discerned from $\mathbf{A}^{(2)}$. The agreement between the model and experiments seen here is excellent, with the model lying within the experimental scatter at all tempera-

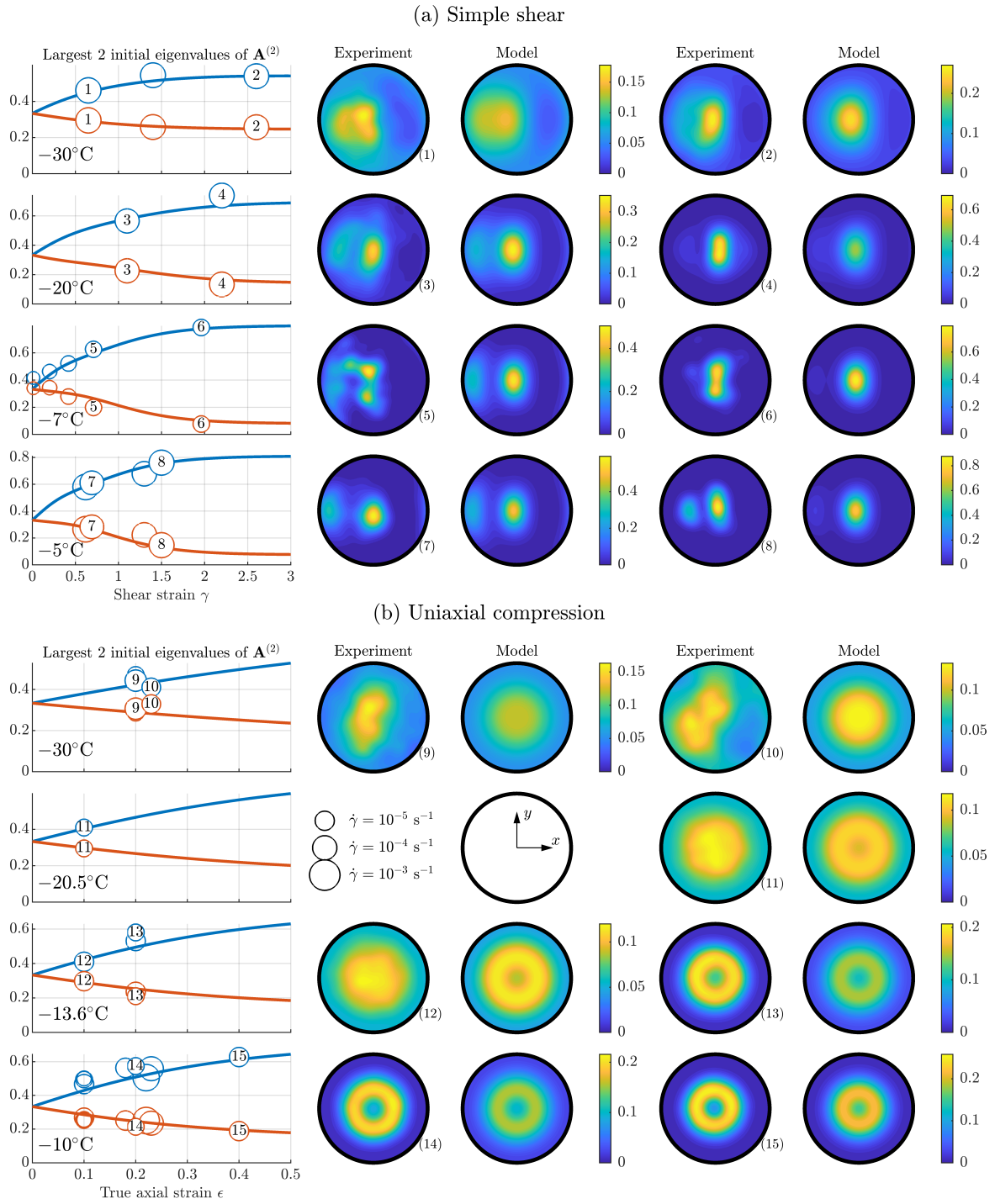


Figure 3.4: Caption on next page.

Figure 3.4: Comparison of the model with experiments performed in (a) simple shear (Journaux et al., 2019; Qi et al., 2019) and (b) compression (Craw et al., 2018; Piazzolo et al., 2013). The simulation parameters $(\tilde{\lambda}, \tilde{\beta}, \iota)$ as functions of temperature were taken from the linear regression in fig. 3.3. Each row shows the comparison between the model and experiments at a specific temperature (and flow field). The first column shows a plot of the largest 2 eigenvalues of $\mathbf{A}^{(2)}$. The line represents the simulation and the circles show experimental values, with their size corresponding to the strain-rate at which they took place. The circles with numbers correspond to plotted experimental pole figures. These are shown alongside pole figures from the model at the same strain. In the top right, the J index for each pole figure is shown, above the number corresponding to the experimental point shown in the plot of $\mathbf{A}^{(2)}$. Table B.1 shows the experimental conditions. The model was run with the spherical harmonics truncated at $L = 12$.

tures. The model also predicts the rapid development of a fabric even at very low strains.

At $T = -30^{\circ}\text{C}$ the model pole figures agree well with experiments. Both experiments (9) and (10) show a large amount of asymmetry in the pole figure which can be assumed to be experimental scatter. At $T = -20.5^{\circ}\text{C}$ and $T = -13.6^{\circ}\text{C}$, the model consistently predicts a cone-shape fabric, even at low strains. However only experiment (13) has a cone-shape fabric, and (11) and (12) do not. At the higher temperature of $T = -10^{\circ}\text{C}$, a cone-shape is seen in both experiments and the model.

Figure 3.5 shows how cone angle changes with temperature and strain. A range of laboratory experiments are plotted as circles, with the colour representing the experimental temperature and the strain-rate shown by the size, as before. The model was run with the interpolated parameters from fig. 3.3, at different temperatures and plotted alongside as solid lines.

Again there is excellent agreement with experiments. At higher temperatures there is scatter in the experiments, but the model generally predicts the trend of cone angle reducing gradually as strain increases for $-15 < T < -5^{\circ}\text{C}$. I also accurately predict the decrease in cone angle at -30°C , including the point at which the fabric transitions from a cone-shape to a single-maximum (corresponding to $\theta = 0^{\circ}$).

These comparisons show that the model, with the parameters determined earlier in simple shear, also work in uniaxial compression with no further fitting required.

3.5 DISCUSSION

3.5.1 *General model behaviour*

In summary, the model incorporates four processes (fig. 2.3): basal-slip deformation; rigid-body rotation of the fabric due to any vorticity in the flow; rotational recrystallization which acts to diffuse any concentrations in the fabric pattern; and migration recrystallization (which acts as a source or a sink at specific orientations depending on the deformation configuration). By including basal-slip deformation and migration recrystallization (and rigid-body rotation in simple shear) the model is able to reproduce all observed fabrics in existing laboratory experiments. Generally, there is excellent agreement across the different deformations of compression and simple shear, across

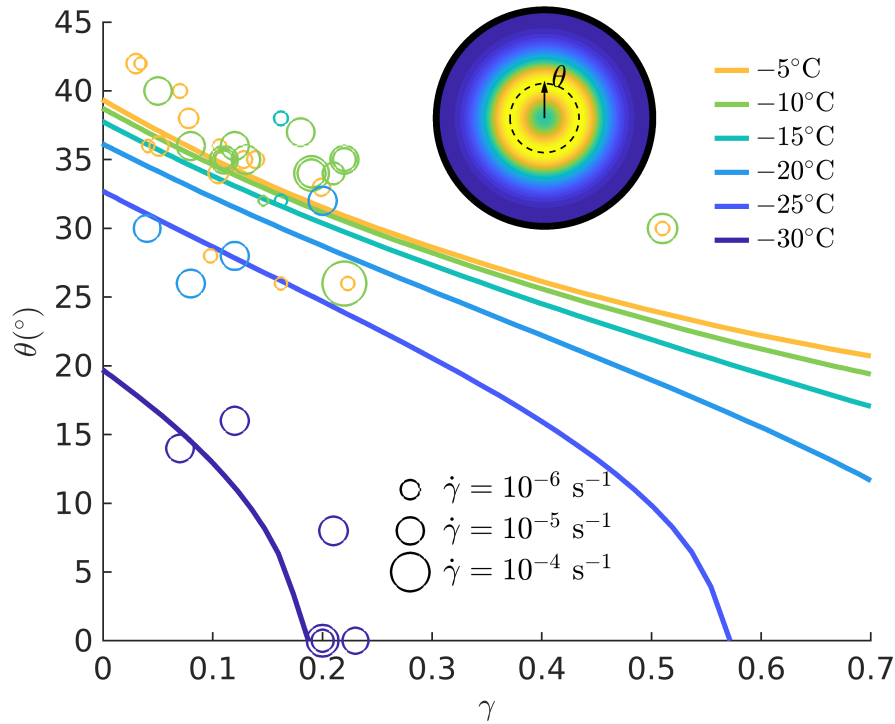


Figure 3.5: Comparison of model predictions and experimental data showing cone angle θ of the fabric in compression (illustrated in the inset pole figure) against strain γ . Solid lines show results from models run at different temperatures using interpolated parameters as shown in fig. 3.3. This figure is from Fan et al. (2020). Experimental data points are shown as circles taken from experiments (Craw et al., 2018; Fan et al., 2020; Jacka, 2000; Jacka and Maccagnan, 1984; Montagnat et al., 2015; Piazzolo et al., 2013; Qi et al., 2017; Vaughan et al., 2017). The size of the marker corresponds to the strain-rate the experiment was performed at, and it is coloured by temperature. Representation chosen and experimental data based on fig 14 and table 4 in Fan et al. (2020).

strain-rates ranging from $10^{-7} - 10^{-4} \text{ s}^{-1}$ and temperatures between -30°C and -5°C . The excellent agreement indicates that other processes, such as non-basal slip, do not need to be modelled explicitly for accurate prediction of fabric evolution even if they are active in the microstructure.

Figure 3.3 shows that as temperature increases both ι and $\tilde{\beta}$ increase, while $\tilde{\lambda}$ stays roughly constant. The general increase of migration recrystallization ($\tilde{\beta}$) with temperature agrees with theory (Faria et al., 2014). However, this work is the first numerical quantification of the importance of migration recrystallization and its change with temperature. Although it could be expected that the temperature dependence would conform to an Arrhenius equation, as all processes are driven by dislocation-creep which itself has an Arrhenius temperature dependence. However, a linear relationship gives the best prediction at intermediate values ($T \approx -20^\circ\text{C}$). Strictly speaking, the parameters are controlling the magnitudes of the different terms in eq. (2.30) and their effect on the fabric pattern, so we are not suggesting that recrystallization itself follows a linear fit. As can be seen in fig. 3.3 it would be helpful to have more data points available for the regression in the region of around -20°C .

The parameter ι , which represents the ratio of basal-slip deformation to rigid-body rotation, increases from ~ 1 at -30°C to ~ 1.6 at -5°C . In comparison, Seddik et al. (2008) found $\iota = 0.6$ best represented fabrics from ice core samples which were at roughly -40°C . They did not posit a temperature dependence. The regression predicts $\iota \approx 0.9$ at this temperature. The difference can be explained by noting that their model did not include recrystallization.

The use of values of $\iota > 1$ is novel. If ι is capped at 1, the model cannot reproduce the experimental pole figures or the evolution of the orientation tensor. For a single grain, described in eq. (2.1) ι must be ≤ 1 . When using a Taylor homogenisation to derive a fabric evolution equation as is done in eq. (2.27) this under-predicts the fabric intensity (Montagnat et al., 2014b). The continuum theory used to derive the fabric evolution model used in this chapter does not place any such constraint on ι . This suggests for polycrystals the effect of basal-slip deformation on the fabric is increased compared to individual grains. I also note that if eq. (2.28) used in Lilien et al., 2021 is combined with Glen's law (eq. (2.3)) this is mathematically equivalent to $\iota = 1.54$.

The increased contribution from basal slip with temperature can be explained by the increased activity of migration recrystallization

at higher temperatures. This means more grains with low dislocation density grow and grains with high dislocation density are consumed. Non-basal slip occurs more frequently in regions of high dislocation density (Chauve et al., 2017). Therefore, migration recrystallization acts to increase the amount of grains favourably orientated for basal slip.

The model predicts that rotational recrystallization, controlled by $\tilde{\lambda}$, is roughly independent of temperature, only increasing by $\sim 15\%$ from -30°C to -5°C . This suggests that rotational recrystallization should be primarily stress or strain-rate dependent, in broad agreement with the theory of Faria et al. (2014).

The offset single-maximum fabric in simple shear which occurs in fig. 3.1d with $\tilde{\beta} = 0$ is also predicted by Llorens et al. (2016) and Van der Veen and Whillans (1994) without recrystallization. In nature and experiments, this is unlikely to occur as this situation can only arise if $\iota \geq 1$ and $\tilde{\beta} \approx 0$. Such a combination of parameters does not occur at any temperature (fig. 3.3): for low temperatures $\iota < 1$ and $0 < \tilde{\beta} < 1$ and for high temperatures migration recrystallization is large even though $\iota > 1$.

3.5.2 Prediction of strain-rate dependence

In fig. 3.3 I have assumed the non-dimensional parameters are independent of strain-rate. This means the ratio of recrystallization rate to strain-rate is constant. As can be seen from fig. 3.4 this is a good assumption to leading order, and the parameters are able to predict the fabric across a variety of strain-rates.

Nevertheless, to provide a first estimate of the strain-rate dependence of the parameters controlling the relative importance of recrystallization processes in eq. (3.13), I perform a regression for the parameters $(\tilde{\lambda}, \tilde{\beta}, \iota)$ including all experimental data, in both compression and simple shear. Table 3.1 shows the inversion results. The mean temperature T , mean strain-rate $\dot{\gamma}$, number of experiments in each set n and coefficients of variances c_v are also shown. For simple shear the parameters were found by minimising the error in the components of $\mathbf{A}^{(4)}$ as described previously. For compression, taking advantage of the expected rotational symmetry of the fabric in φ , the error was defined as the θ integral of the difference between φ averaged $\tilde{\rho}^*$:

	Flow	$T/^\circ\text{C}$	$\dot{\gamma}/\text{s}^{-1}$	n	$c_v(T)/\%$	$c_v(\dot{\gamma})/\%$	$\tilde{\lambda}$	ι	$\tilde{\beta}$
Compression		-30.0	1.26×10^{-5}	3	0.00	107	0.173	1.23	0.620
		-13.6	7.50×10^{-6}	3	0.00	57.7	0.198	1.93	4.25
		-10.2	1.03×10^{-5}	3	8.90	5.60	0.126	1.54	5.92
		-9.50	1.66×10^{-4}	2	3.00	64.5	0.343	1.98	2.75
Simple shear		-30.3	1.33×10^{-4}	3	1.20	8.60	0.153	0.993	0.763
		-7.00	1.14×10^{-6}	5	0.00	71.9	0.139	1.65	4.12
		-5.50	1.26×10^{-4}	4	3.50	33.3	0.178	1.59	5.51

Table 3.1: Table showing the results from the inversion for parameters.

The inversion was performed for 7 bins in total, each with a mean temperate and strain-rate. The coefficient of variance is also shown, along with the parameters.

$$\text{error} = \int_0^{\pi/2} \left| \int_0^{2\pi} \rho_{\text{exp}}^*(\theta, \varphi) \, \text{d}\varphi - \int_0^{2\pi} \rho_{\text{sim}}^*(\theta, \varphi) \, \text{d}\varphi \right| \sin \theta \, \text{d}\theta. \quad (3.14)$$

This takes advantage of the rotational symmetry of the fabric in compression to give a more precise measure of the difference between two fabrics. Table 3.2 shows regressions with and without strain-rate dependence. These regressions were performed using all the data in the table above (both compression and simple shear) hence are different from fig. 3.3. The fit results, R^2 , adjusted R^2 and confidence intervals are shown to compare regressions with different number of predictors.

The fit for strain-rate dependence in table 3.2 is the first quantification of how the parameters change with strain-rate. However including strain-rate dependence widens the confidence intervals for the parameters. Further experiments are required for a more reliable estimate. However as a first attempt the values are close to what was hypothesised: for all parameters the exponents are close to zero, highlighting the weakness of the dependence. For ι the exponent is especially close to zero (0.002) supporting the hypothesis that effect of basal-slip deformation on the fabric is independent of strain-rate. Furthermore this first estimate also gives $a = p_{\tilde{\lambda}} + 1 > 1$ and $b = p_{\tilde{\beta}} + 1 < 1$ from eq. (3.13). Therefore, this suggests the rate of rotational recrystallization increases with strain-rate while the rate of migration recrystallization decreases with strain-rate.

Variable	Equation	m	c	p	R^2	R^2_{adj}
$\tilde{\lambda}$		0.001	0.21	-	0.033	-0.16
ι	$mT + c$	0.026	1.95	-	0.60	0.53
$\tilde{\beta}$		0.176	6.09	-	0.76	0.71
$\tilde{\lambda}$		0.007	0.80	0.124	0.37	0.056
ι	$(mT + c)\dot{\gamma}^p$	0.027	2.00	0.002	0.60	0.41
$\tilde{\beta}$		0.144	4.98	-0.018	0.77	0.65

95% confidence interval						
Variable	Equation	m		c	p	
$\tilde{\lambda}$		-0.007 - 0.009		0.065 - 0.347	-	
ι	$mT + c$	0.002 - 0.050		1.516 - 2.390	-	
$\tilde{\beta}$		0.063 - 0.289		4.046 - 8.125	-	
$\tilde{\lambda}$		-0.025 - 0.039		-1.221 - 2.823	-0.119 - 0.368	
ι	$(mT + c)\dot{\gamma}^p$	-0.017 - 0.071		-0.252 - 4.260	-0.097 - 0.102	
$\tilde{\beta}$		-0.155 - 0.443		-4.802 - 14.76	-0.193 - 0.156	

Table 3.2: Table showing the regression results using the inversion data in table 3.1. Results are shown both with and without strain-rate dependence. The R^2 and adjusted R^2 values are also shown, along with the 95% confidence intervals for each fitted parameter.

3.5.3 *Comparison with other models*

In a hierarchy of complexity for modelling ice fabrics, this model sits between modelling the polycrystal directly (Kennedy et al., 2013; Llorens et al., 2016), and solving for the evolution of the orientation tensors (Gagliardini et al., 2013; Lilien et al., 2021; Seddik et al., 2011). The model SpecCAF used here is much less computationally expensive than full-field models, and of comparable cost to solving for orientation tensors. This means it is a candidate for including in ice-sheet models.

Models such as Llorens et al. (2016) simulate directly the polycrystal and hence give a more complete representation of the microstructure than included here. However, it is difficult to apply general or changing deformations to these models. Such models are also far too computationally expensive to be used in ice-sheet models. The model used in this paper does not have these disadvantages. Despite this, the results compare favourably with Llorens et al. (2016). The model is consistently able to reproduce the secondary cluster seen in experiments, whereas the bulk fabrics produced by Llorens et al. (2016) do not show one, although it does appear in the high strain-rate areas for $\gamma < 1$. Therefore, the model is able to produce details that full-field models have not been able to produce to date.

To simulate fabrics at an ice divide Bargmann et al. (2012) used the same fabric evolution equation as this paper but solved with a finite-volume method. They constrained the parameters to an order of magnitude. They found $\tilde{\beta} = O(1)$ and $O(0.01) < \tilde{\lambda} < O(0.1)$, consistent with the results.

For large-scale ice-sheet models, the current approach to model fabric evolution is to calculate the evolution of the second-order orientation tensor without migration recrystallization, as described in eq. (2.28). This is equivalent to setting $\tilde{\beta} = 0$ and running SpecCAF with $L = 2$. This is unable to produce any detailed features, including cone-shape fabrics in compression or the secondary-cluster fabrics in simple shear. Therefore, eq. (2.28) is likely unable to predict the orientation tensors sufficiently accurately to model viscous anisotropy.

3.5.4 *Future Applications*

Our contribution of the spectral method and parameter inversion represents a step forward for the accuracy of fabric predictions in

ice-sheet models. The model and parameters can take the flow field, temperature and strain-rate as inputs and then predict accurately the fabric. The versatility, accuracy and computational efficiency of the model across deformations and temperature make it an excellent candidate for integration into ice-sheet models such as Elmer/Ice (Gagliardini et al., 2013). It should also be noted that, if SpecCAF is incorporated in such models, then the user can adjust the number of spherical harmonics L to balance accuracy against computational cost. For example, although I use $L = 12$ in this paper, $L = 6$ can still represent a secondary cluster in the fabric, as shown in fig. B.1. SpecCAF can also be used to explore the parameter space of deformation regimes and temperature due to its computational efficiency, and applied to simulate fabrics taken from ice cores.

The framework presented here can also be applied to other geological materials that develop a fabric and viscous anisotropy. The model-solver SpecCAF is transferable to other crystalline materials whose plasticity is dominated by one slip system in a certain temperature range, like mica or quartz (Kronenberg et al., 1990; Schmid and Casey, 1986). SpecCAF could also be generalised to other materials with multiple active slip systems. In this case the combination of the scheme with existing continuum models for slip-dependent fabric development is promising. For example, fabric development in olivine is an important research area: olivine is the main constituent of the upper mantle (Boehler, 1996) and has seismic and viscous anisotropy which is controlled by the fabric (Nicolas and Christensen, 1987). Large scale geodynamic models are highly dependent on the flow of the mantle where viscous anisotropy may play a major role (Tommasi et al., 2009). Thus accurately predicting fabric development is key for this field.

3.6 CONCLUSIONS

We provide the first complete, fully constrained framework for predicting the fabric for low computational cost, at any temperature including all key processes. This is done by solving the fabric evolution equation by Placidi et al. (2010) using a spectral method adapted from Montgomery-Smith et al. (2010) and then using experimental data in simple shear and compression to constrain the model parameters. The spectral method can solve the equations to high accuracy with low computational cost. The inversion for the model parameters (fig. 3.3)

provides the first quantitative estimate of the relative importance of different processes which affect the fabric as functions of temperature. The model-solver SpecCAF, combined with these parameters as functions of temperature, gives excellent agreement with experiments across a large range of deformations, temperatures and strain-rates.

The model provides new inroads towards understanding ice fabric dynamics under different deformations, for the interpretation of ice cores, and for implementation into ice-sheet models. The model provides the first method to capture all key features of fabrics such as secondary clusters across a range of temperatures and deformations and shows greater accuracy than full field models for much lower computational cost. That these accurate predictions arise mainly from the balance between basal-slip deformation and migration recrystallization highlight the importance of these processes. The constrained model provides a complete toolkit to model dynamically the fabric development in an ice sheet.

SpecCAF could be extended to other crystalline materials with one dominant slip system, such as micas. Furthermore, it could be generalised to incorporate more than one slip system, enabling modelling of more complex polycrystalline materials such as olivine, which is of primary importance to mantle dynamics.

ICE FABRICS IN TWO-DIMENSIONAL DEFORMATIONS: BEYOND PURE AND SIMPLE SHEAR

ABSTRACT

Ice fabrics are key for understanding and predicting ice flow dynamics. Despite its importance, the characteristics and evolution of ice fabrics beyond pure and simple shear flow has largely been neglected. Within an ice sheet, a significant part of the deformation can be outside the regimes of pure and simple shear. I use the model developed in the previous chapter, SpecCAF, which was shown to accurately reproduce experimentally observed fabrics in both compression and simple shear, to classify the fabrics produced under general two-dimensional deformation regimes. My analysis develops the first predictions for fabric patterns arising over a continuous spectrum of incompressible two-dimensional deformation regimes and temperatures, encompassing those intermediate to pure and simple shear, as well as those that are more rotational than simple shear. I find that intermediate deformation regimes between pure and simple shear result in a smooth transition between a fabric characterised by a cone-shape and a secondary cluster pattern. Highly-rotational deformation regimes are revealed to produce a weak girdle fabric. In addition, I obtain predictions for the strain-scales over which fabric evolution takes place at any given temperature. The use of this model in large-scale ice flow models as well as for interpreting fabrics observed in ice cores and seismic anisotropy, will provide new tools supporting the community in predicting ice flow in a changing climate.

This chapter is based on a manuscript in review in the international Journal *The Cryosphere* (Richards et al., 2021a). Revisions in response to reviewers have been submitted on 1st November 2021. As with the previous chapter, it has been edited to fit into the thesis, with parts of the background moved into section 2.1.2 and section 2.1.3, and the methods section combined with the corresponding section from Richards et al. (2021b) and merged into section 2.2.4.2.

4.1 INTRODUCTION

To date, the analysis and discussion of ice fabrics has focused primarily on those formed under the specific deformation regimes of pure and simple shear. The primary motivation of this chapter is to use the validated fabric model SpecCAF (Richards et al., 2021b) to take a step away from the isolated conditions of pure and simple shear and explore the continuous space of deformation regimes lying intermediate to these endmember cases, and also those that are more rotational than simple shear, across a unified spectrum. Ice flow is commonly modelled in the two-dimensional x - z plane (e.g. Martín et al., 2009), and analysis of this flow shows that it commonly resides outside the endmember regimes of pure and simple shear (we illustrate this below in section 4.2.2.1 below). Therefore, an exploration of the fabric patterns arising in this generalised situation is necessary as a step towards improving our ability to interpret fabrics derived from ice cores and to predict future ice flow taking ice fabric effects into account. As a first step towards this, we seek here to address a number of open questions. First, what fabrics are produced under any given (incompressible) two-dimensional deformation regime? Second, how do fabrics evolve at the very high strains which have remained inaccessible to laboratory experiments? Third, what strains are necessary to reach steady state in the different deformation regimes? Finally, at these high strains, how are the final steady states dependent on parameters such as temperature and type of deformation regime?

4.2 BACKGROUND

4.2.1 *Experiments in intermediate deformations*

In addition to the experiments in compression and simple shear described in section 2.1.2, experiments also have been performed using combined compression and shear, at close to the melting point of ice (Budd et al., 2013; Duval, 1981; Jun et al., 1996). Fabrics from Duval (1981) combining unconfined compression and simple shear show a broad cluster with 3 or 4 maxima inside it. Budd et al. (2013) shows, for an experiment with mostly simple shear combined with some confined compression and at an equivalent strain to that used later in this chapter of 0.75, a fabric which shows the merging of a double cluster (from pure shear) and a single-maxima (from simple shear). Experi-

ments have also been performed with layered samples of ice (Wilson, 2000; Wilson and Peterzell, 2012). In addition to the relatively few experiments that have been conducted under a combination of simple and pure shear, no analysis has been conducted of situations where fabrics are produced in deformation regimes more rotational than simple shear. We show in section 4.2.2.2 that deformation regimes inbetween pure and simple shear, and those more rotational than simple shear, occur widely in natural ice-sheet flows.

4.2.2 *Classifying flow regimes*

4.2.2.1 *General deformation regimes*

There exists a significant variety of deformation regimes in the natural world. One way to classify a deformation regime is by the vorticity number (Passchier, 1991), which measures the ratio of vorticity magnitude to strain-rate magnitude:

$$\mathcal{W} = \sqrt{\frac{W_{ij}W_{ij}}{D_{ij}D_{ij}}}, \quad (4.1)$$

where $\mathbf{W} = \frac{1}{2}(\nabla\mathbf{u} - \nabla\mathbf{u}^T)$ is the anti-symmetric part of the velocity gradient (the spin-rate tensor) and $\mathbf{D} = \frac{1}{2}(\nabla\mathbf{u} + \nabla\mathbf{u}^T)$ is the symmetric part of the velocity gradient (the strain-rate tensor). Figure 4.1 illustrates different flow regimes and the corresponding vorticity number \mathcal{W} for each. The vorticity number is 0 for pure shear or uniaxial compression, 1 for simple shear and ∞ for rigid-body rotation. Ice in the natural world will experience deformation regimes with vorticity numbers from 0 to ∞ , however to date fabrics produced for $\mathcal{W} = 0$ and $\mathcal{W} = 1$ are the only areas which have been extensively explored due to the limitations of possible deformation regimes in experiments.

In the late 1990s and early 2000s it was recognised in the geological community that flow in rocks cannot be approximated by endmember plane strain flow models alone (Bailey and Eyster, 2003; Jiang, 1994). There is now an extensive literature within structural geology which developed conceptual models and analytical techniques to predict and recognise natural geological flows with vorticity numbers between 0 and 1 (Fossen and Tikoff, 1993; Piazzolo et al., 2004; Piazzolo et al., 2002; ten Grotenhuis et al., 2002; Tikoff and Fossen, 1995) In contrast, such analysis is less common in discussions surrounding ice core interpretation; pure shear and simple shear tend to dominate

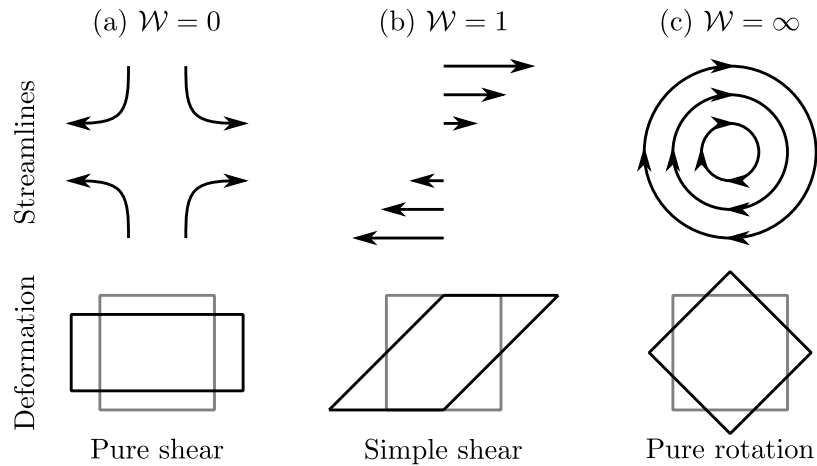


Figure 4.1: Schematics illustrating two-dimensional flow regimes at different vorticity numbers \mathcal{W} (eq. (4.1)): (a) Pure shear ($\mathcal{W} = 0$), (b) Simple shear ($\mathcal{W} = 1$), (c) Pure rotation ($\mathcal{W} = \infty$). For each flow the streamlines and deformation regime produced are shown.

discussions regarding both the interpretation of ice-sheet flow and experimental analysis. This may be mainly due to the fact that such endmember scenarios are a) experimentally straightforward to achieve, b) the two endmembers can – as a first approximation - be associated with different ice flow scenarios of an ice divide and the shallow ice approximation.

4.2.2.2 *Two-dimensional deformation regimes in natural ice flow*

As a first step towards exploring the fabrics produced by all possible deformation regimes, we will focus here on general incompressible two-dimensional deformations. Although deformation regimes in the natural world will be three-dimensional, exploring fabrics produced by two-dimensional deformation regimes is a natural first step away from the canonical regimes of pure and simple shear. It is also common to limit the modelling of ice sheets to two dimensions in the vertical cross-section (Martín et al., 2009; Pattyn et al., 2008). In fig. 4.2, we show the vorticity number from a 2D simulation of flow at an ice divide and its horizontal transition towards a flow dominated by vertical shear stresses (the shallow ice approximation). Due to the vanishing of horizontal velocity at the divide, the vorticity number is 0 there, corresponding to the regime of pure shear along the centre line. Away from the divide, the flow dominated by vertical shear stresses exhibits

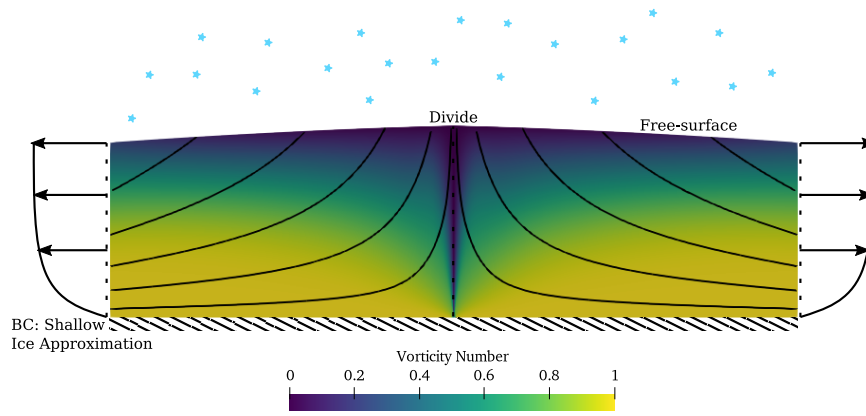


Figure 4.2: Illustrative figure showing the vorticity number for ice flowing at a divide, showing a range from 0 to 1. The problem setup is from Martín et al. (2009) with isotropic ice. The simulation has an aspect ratio of 20, but only the region from $x = 0$ to $x = 10H$, where H is the height of model domain, is shown. The domain has the velocity from the shallow-ice-approximation imposed at the left and right boundaries, and the surface accumulation is set to match the outflow, corresponding to a steady state. No-slip is imposed at the base and a free surface is assumed at the top. The vorticity number is shown, alongside streamlines. This flow was computed using a full-Stokes solver written in FEniCS (Martin Alnæs et al., 2015) with $n = 3$ and solved using Taylor-Hood elements.

a transition in the vorticity number from 1 at the base, corresponding to simple shear, towards close to 0 at the surface. In summary, the figure shows vorticity numbers between 0 and 1 are the norm.

It is not only vorticity numbers between 0 and 1 which can occur. Vorticity numbers greater than 1, corresponding to deformation regimes more rotational than simple shear, are predicted to occur in ice sheets. As an example consider the flow of ice over a Gaussian bump at the base shown in fig. 4.3. This is modification of the Ice Sheet Model Intercomparison Project for Higher-Order Models (ISMIP-HOM) experiment F benchmark (Pattyn et al., 2008), representing ice flowing downhill over a Gaussian bump. Compared to Pattyn et al. (2008), the bump is 4 times higher and 31.6 times sharper. This shows that even in a simple configuration, vorticity numbers greater than 1 can potentially occur in the vertical velocity profile. Figure 4.3 shows vorticity

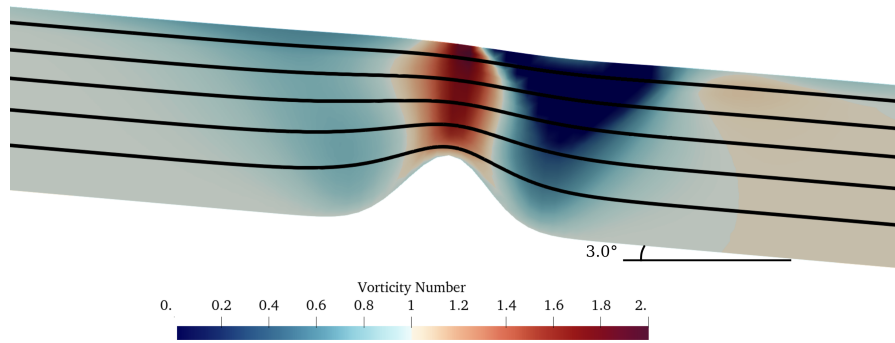


Figure 4.3: The vorticity number for a 2D slice from a modified version of the [ISMIP-HOM Experiment F benchmark](#) (Pattyn et al., 2008). The ice is flowing from left to right, down a hill with angle 3.0° , and encounters a Gaussian bump at the base. Compared to Pattyn et al. (2008), the Gaussian bump is 4 times higher and 31.6 times sharper. Over the bump the flow accelerates leading to vorticity numbers greater than 1. This simulation was performed using Elmer/ICE (Gagliardini et al., 2013) with $n = 1$.

numbers up to 2. To-date, the fabrics produced for vorticity numbers above 1 have not been analysed.

Further, I have calculated an estimate of the vorticity number near the surface of Antarctica, in order to illustrate the natural deviation from endmember regimes. To do this I have used surface velocity data from Antarctica (Mouginot et al., 2019) to calculate the vorticity number, shown in fig. 4.4. I have calculated the surface velocity gradients $\partial u/\partial x, \partial u/\partial y, \partial v/\partial x, \partial v/\partial y$ using central differencing. To evaluate the vorticity number, I use these estimates of horizontal velocity gradients combined with an estimate of the maximum vertical shear ($\partial u/\partial z, \partial v/\partial z$) in the top 25% of the depth of the ice-sheet determined using the shallow-ice approximation assuming no slip at the base of the ice sheet. The derivative $\partial w/\partial z$ is calculated using mass continuity and I have neglected the higher-order contributions $\partial w/\partial x$ and $\partial w/\partial y$.

To reduce the errors in the data for fig. 4.4 I have taken the mean value from a 10×10 block (covering a 4.5 km square). We have defined the standard deviation of any variables, such as velocity components, as the variance from the mean of the 100 samples in each 10×10 block. The relative standard deviation controls the transparency: if this is $> 100\%$ this location is plotted as white, and a relative standard

deviation of 0% is plotted as the full colour. From this figure we can see that there are many regions of Antarctica where the vorticity number near the surface is both at intermediate values between 0 and 1, and greater than 1. The regions characterised by high vorticity numbers ($W > 1$) occur typically in highly dynamic regions such as ice streams. Closer to the base of an ice-sheet, in regions where there is significant basal drag, the vorticity number tends to 1 as the vertical gradients dominate. In regions with no basal slip, these vorticity numbers are potentially valid to approximately 25% into the ice-sheet. In regions with slip at the base, the vorticity number will be valid deeper into the ice sheet.

4.2.3 *Open questions addressed here*

In this chapter I use the SpecCAF model to address the open questions highlighted in the introduction: what fabrics are produced under any given (incompressible) two-dimensional deformation regime, how do fabrics evolve at the very high strains, what strains are necessary to reach steady state, and how are these final steady states dependent on the parameters?

In section 4.4.1 I determine for the first time the evolution of fabrics in general 2D deformation regimes, bridging the complete spectrum from pure shear to rigid-body rotation, across the range of temperatures seen in ice sheets. In section 4.4.2 I construct a complete regime diagram for two-dimensional deformation regimes documenting fabrics that arise over the space of temperature, deformation regime, and strain, and explain the physical balances leading to these fabrics. Finally, in section 4.4.3 I investigate the time or strain scales over which ice fabric evolution takes place, as well as investigating the steady-state strength of ice fabrics, across the space of deformation regime and temperature. I then discuss the implication of these results for the interpretation of ice cores (section 4.5.3) and ice flow (section 4.5.4).

4.3 METHODS

I use the same model equations as in section 2.2.4.2 and chapter 3, therefore they are not repeated here.

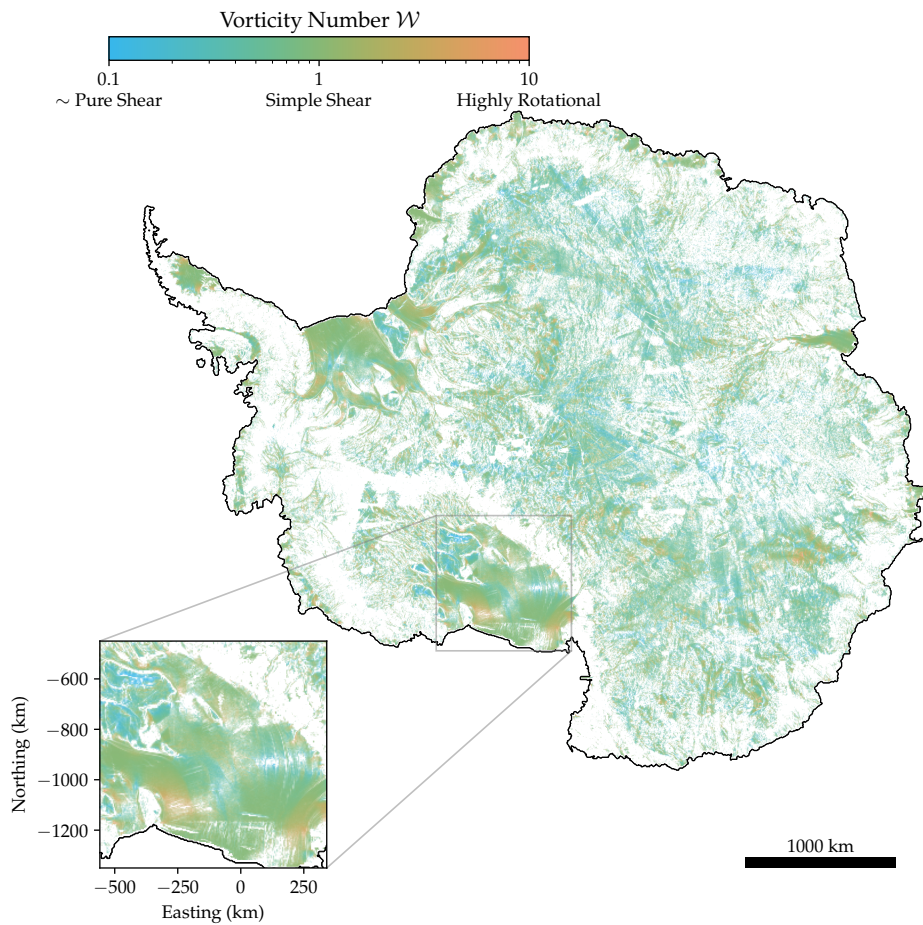


Figure 4.4: Vorticity number (defined in eq. (4.1)) calculated from the surface velocity data of Antarctica (Mouginot et al., 2019) after averaging over a 10×10 block and taking the mean value within each block. The calculation uses the horizontal velocity fields from the observed surface velocity combined with an estimate of the average vertical shear predicted to occur in the top 25% of the ice sheet using the shallow-ice-approximation. The colour shows the vorticity number on a log scale. The transparency shows the relative error: an error in \mathcal{W} of 100% or greater is plotted as white and an error of 0% is plotted as the full colour. The inset shows the Ross Ice Shelf, with the easting and northing in Antarctic polar stereographic coordinates. This shows considerable variation across the continent, including deformation regimes not accessible in the laboratory.

4.3.1 Non-dimensionalisation

The non-dimensionalisation I perform is slightly different to chapter 3. In this chapter I non-dimensionalise with the effective strain-rate:

$$\dot{\gamma} = \sqrt{\frac{1}{2}D_{ij}D_{ji}}. \quad (4.2)$$

This is equal to the square root of the second invariant of the strain-rate tensor \mathbf{D} . The strain-rate I non-dimensionalise with in this chapter is $\frac{1}{\sqrt{2}}$ times the strain-rate I used in eq. (3.1), which was based on the experimental strain-rate. I also use a slightly different temperature dependence for the parameters. In this chapter, I use a best fit from the entire inversion performed in table 3.1, rather than just from the inversion performed in simple shear. Furthermore, as the strain-rate I use to non-dimensionalise is $\frac{1}{\sqrt{2}}$ times that used in chapter 3, the non-dimensional recrystallization parameters $(\tilde{\lambda}, \tilde{\beta})$ used in this chapter are double those used in chapter 3. The non-dimensional parameters as functions of temperature are shown in fig. 4.5, along with the data points used and the 80% and 95% confidence intervals. In Appendix C a parameter sensitivity study can be found, reproducing figs. 4.7 and 4.9 to 4.12 with (a) $\iota_{\max}, \tilde{\beta}_{\max}, \tilde{\lambda}_{\min}$ and (b) $\iota_{\min}, \tilde{\beta}_{\min}, \tilde{\lambda}_{\max}$, with the max and min values taken from the 80% confidence interval in fig. 4.5. The maximum and minimum set of values (a) and (b) are chosen to give the strongest and weakest fabric respectively.

4.3.2 Pole figure and cross section representation

As a preliminary illustration of the model output and its representation, I show in fig. 4.6 an example of model output obtained by solving the model at $T = -5^\circ \text{C}$, in simple shear ($\mathcal{W} = 1$). The principal axes are orientated at $\theta = \pm 45^\circ$ directions of the pole figure. To visualise how the fabric changes with increasing strain, I plot slices of the pole figure at $y = 0$. The example pole figure in (a) is plotted at a strain of $\gamma = 0.345$. The value of ρ^* at $y = 0$ is plotted in (c) for each strain. This shows how the fabric develops from isotropic. A secondary cluster can clearly be seen as a transient feature which has mostly disappeared by $\gamma = 0.8$.

As an example comparison of the model prediction and experimental observations, I have included a pole figure from laboratory experiments (Qi et al., 2019) in fig. 4.6b, as I have done in fig. 3.4. This

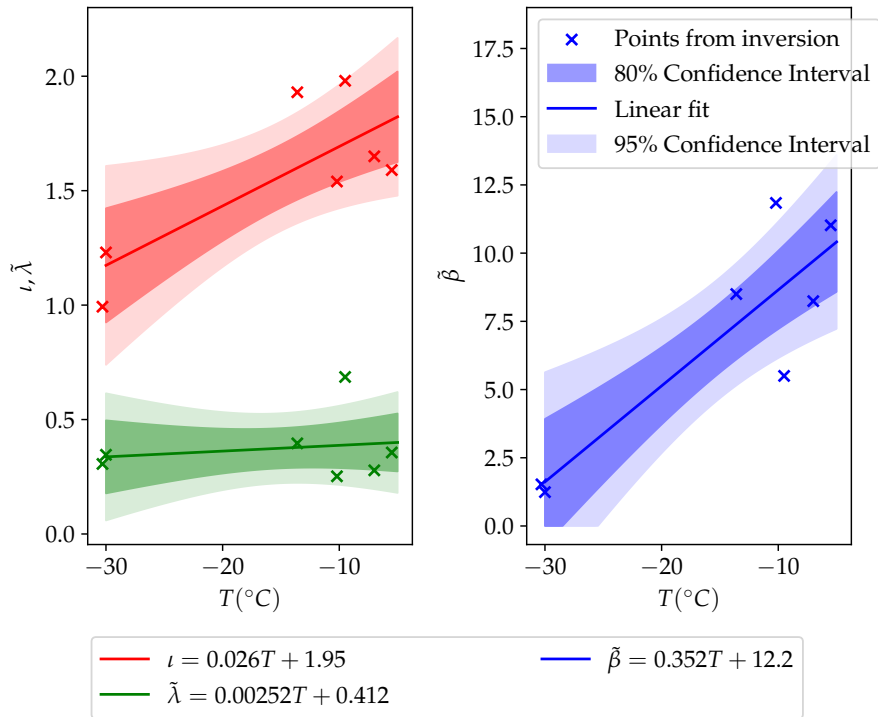


Figure 4.5: The model parameters $\iota, \tilde{\lambda}, \tilde{\beta}$ as functions of temperature, determined by linear regression to experimental data in both compression and simple shear, as conducted in Richards et al. (2021b). The 95% and 80% confidence intervals are shown.

is at the same temperature and strain as the model output in (a). There is very good agreement between the model and experiments.

4.4 RESULTS

4.4.1 *General fabric evolution: dependence on temperature and vorticity number*

I explore fabric evolution across a complete, continuous range of vorticity numbers \mathcal{W} for two-dimensional deformation regimes (spanning $\mathcal{W} = 0$ to ∞), and a continuous range of temperatures T relevant to ice-sheet flow ($T = -30$ to -5 ° C). For all cases, I assume an initially isotropic fabric. To make comparisons, I will limit my analysis to fabrics undergoing a constant two-dimensional deformation and at a constant temperature. The vorticity number, defined in eq. (4.1), gives the ratio of vorticity to strain-rate magnitude. However, it does not fully constrain the velocity gradient. To do so, I define the non-dimensional velocity gradient as:

$$\nabla \tilde{\mathbf{u}} = \begin{bmatrix} 1 & \mathcal{W} \\ -\mathcal{W} & -1 \end{bmatrix}. \quad (4.3)$$

This gives pure shear for $\mathcal{W} = 0$, simple shear for $\mathcal{W} = 1$ and rigid-body rotation as $\mathcal{W} \rightarrow \infty$. The principal-axes of deformation are aligned with the coordinate axes and are unchanged as \mathcal{W} varies.

With the velocity gradient fully defined, I explore the fabric dynamics produced across \mathcal{W} - T space in fig. 4.7. For each square I show the slice through the pole figure at $y = 0$ (explained in fig. 4.6) up to a finite strain of $\gamma = 1$. The temperature range is from -30 ° C to -10 ° C, temperatures typical in ice sheets (Duval et al., 2010). The vorticity number ranges from $\mathcal{W} = 0.1$, very close to pure shear, and $\mathcal{W} = 10$ representing highly vortical flow with curved streamlines. This provides a detailed picture of how the fabric evolves with increasing strain, providing insights into deformation regimes between compression and simple shear as well as showing fabrics produced by deformation regimes more rotational than simple shear. For low vorticity numbers, a single maximum can be seen at low temperatures which develops into double-maxima as strain increases. As \mathcal{W} increases the clusters are moved by the rotational component of the deformation,

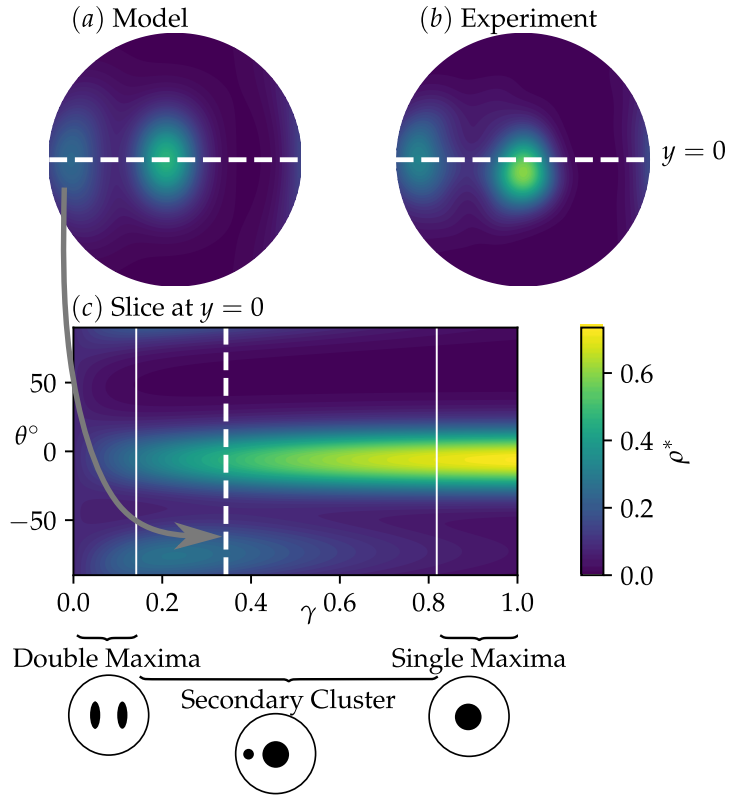


Figure 4.6: To illustrate the fabric I show a simulation in simple shear at $T = -5^\circ \text{C}$. (a) shows a pole figure from the model at an effective strain of $\gamma = 0.345$ (where the strain-rate is defined as in eq. (4.2)). (b) shows a pole figure from laboratory experiments (Qi et al., 2019) at the same temperature and strain, showing good agreement. The white dotted line in (a) and (b) shows $y = 0$. (c) shows $\tilde{\rho}^*$ at $y = 0$ against strain. Here the white dotted line highlights the strain at which the pole figure is plotted. θ is the polar angle. Also highlighted is the classification of the different fabric types at different strains; from double-maxima to secondary cluster to the steady state single maxima. For this figure only the principal axes of deformation are oriented at $\theta = \pm 45^\circ$.

resulting in a primary and secondary cluster. The weaker, secondary cluster is gradually consumed by migration recrystallization as strain increases, leading to a single maximum at high strains, for $\mathcal{W} \sim O(1)$.

I also show in fig. 4.7 analysis of fabrics produced in highly rotational ($\mathcal{W} > 1$) deformation regimes, which as I have shown are prevalent in real-world conditions (figs. 4.3 and 4.4). Figure 4.7 shows that the fabric is strongest for $\mathcal{W} = 1$, and weakens as vorticity increases past this. For example, for $\mathcal{W} = 10$ there is only a very weak fabric produced. Furthermore, at large vorticity numbers oscillation can be seen in the fabric pattern. Figures C.1 and C.2 in Appendix C show that variations in the parameters from fig. 4.5 affect the strength of the primary cluster primarily, but do not affect the variation with vorticity number or the transition from one fabric type to another. To further analyse the limit of very large vorticity numbers I show the fabric produced as $\mathcal{W} \rightarrow \infty$ in fig. 4.8. This fabric is seen for any vorticity number above $\mathcal{W} \approx 50$. To measure fabric concentration I use the J index, as defined in eq. (3.12). The J index of this fabric is 1.16, very close to completely isotropic ($J = 1$). It is unlikely this weak girdle fabric would be distinguishable from an isotropic fabric in a physical sample, where the fabric is determined by sampling a limited number of grain orientations.

4.4.2 Fabric regime diagrams for cluster angle and fabric type

To distil all the complex information shown in fig. 4.7 and make this information more easily accessible, I present results showing the variation of the angle of the primary cluster and the regimes of different fabric patterns across the \mathcal{W} - T space. The angle between the primary cluster and the closest principal axis of deformation (i.e. the axis of compression) is shown in fig. 4.9 at six separate finite strain values, across \mathcal{W} - T space. Even at a low finite strain of $\gamma = 0.3$ there is already an established difference in angle across the parameter space (fig. 4.9a). Low temperatures and low vorticity numbers have the primary cluster most closely aligned with the compression axis. The angle then increases as both temperature and especially vorticity number increase. As strain increases the variation in angle increases. However, for a finite strain greater than 0.5 the angle is mostly invariant with strain. Across the strain and temperature range, an angle of around 40° implies simple shear ($\mathcal{W} \approx 1$), whereas if the primary

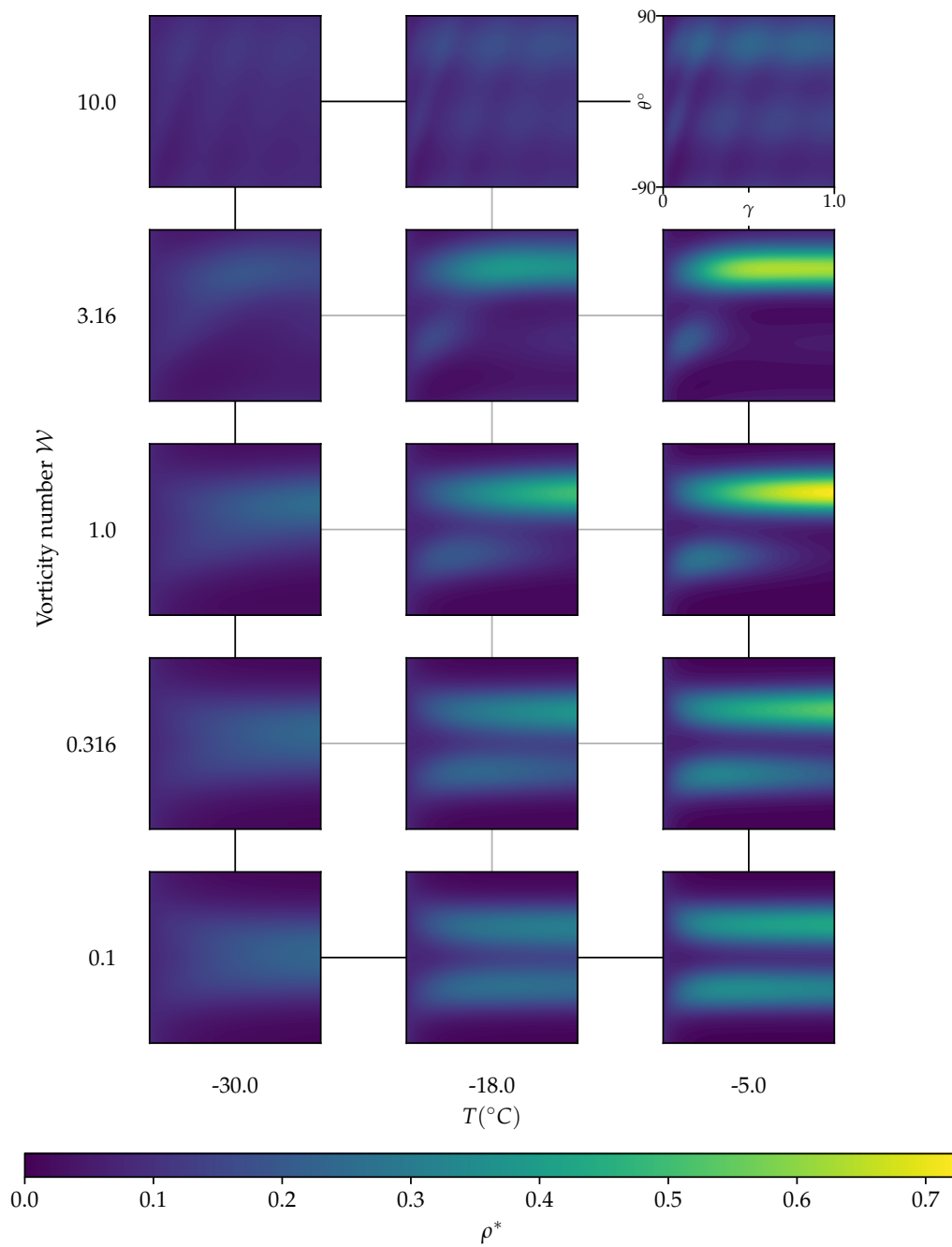


Figure 4.7: Slices of the pole figure showing the value of ρ^* at $y = 0$ for an array of temperatures and vorticity numbers. All $y = 0$ plots go to a strain of $\gamma = 1$. The colour limits are the same for all plots.

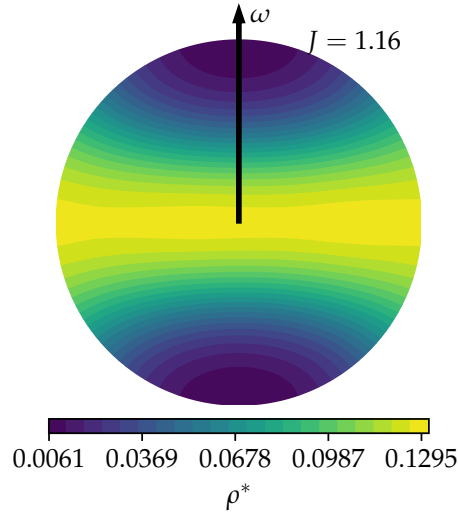


Figure 4.8: Pole figure for $\mathcal{W} \rightarrow \infty$ and $T = -5^\circ \text{C}$ at steady-state. A very weak girdle fabric is produced, with the girdle coincident with the axis of vorticity, shown. This fabric has a J index of 1.16, where $J = 1$ is an isotropic fabric.

cluster and compression axis are coincident, this suggests pure shear at $T \approx -30^\circ \text{C}$.

Figures C.3 and C.4 in Appendix C show fig. 4.9 with the strongest and weakest possible fabric based on the 80% confidence intervals in fig. 4.5. At low vorticity numbers and temperatures, the angle between the primary cluster and compression axis is slightly sensitive to variations in parameters, but outside of this space the angle is roughly unchanged.

As a means to visualise the variety of fabrics in terms of both the parameter space and across possible finite strains I show a regime diagram for fabric patterns in fig. 4.10. To define whether a fabric is a double-maxima, secondary cluster or single-maxima I take the ratio of the two largest peaks in the fabric. If the 2nd largest peak is less than 10% the strength of the largest peak, it defines as a single-maxima. If the strength of the 2nd largest peak is between 10% and 90% of the largest peak, it is defined as a secondary cluster. If it is $> 90\%$ it is defined as a double-maxima. Contour lines of primary cluster angle at 20° and 50° are also shown. This shows the different fabric types (fig. 2.4) across the space of temperature, vorticity number and finite strain. The figure is in the same format as fig. 4.9.

Figure 4.10a shows the initial fabric after a finite strain of only $\gamma = 0.3$. There are three regimes at this finite strain. For approximately

$\mathcal{W} < 0.7$ a double-maxima is produced. There is a small region, at high vorticity numbers and primarily at low temperatures but extending into high temperatures, at which a single-maxima is produced. Otherwise a secondary cluster is produced, this occurs for relatively high vorticity numbers and is more dominant at higher temperatures, as expected. At higher finite strain the double-maxima pattern becomes less prevalent, only occurring at lower vorticity numbers or not at all. This highlights the transient nature of this pattern. As a reminder, the double-maxima is the 2D equivalent of a cone-shape fabric (fig. 2.4). The double-maxima fabric is only present up to a finite strain of about $\gamma = 0.5$. In fig. 4.10c, at $\gamma = 1.0$ the parameter space is dominated by single-maxima and secondary-cluster patterns. Ice fabrics which develop at higher temperatures $T > -20^\circ\text{C}$ are dominated by secondary cluster patterns, with the exception of around $\mathcal{W} \approx 3$, where a single-maxima occurs because the secondary cluster is too weak. At lower temperatures $T < -25^\circ\text{C}$ a single-maxima is produced because migration recrystallization is not active enough for multiple clusters to be produced. This balance between a single-maximum fabric and a secondary cluster fabric continues as the finite strain increases, with a single-maxima also becoming more prevalent at high temperatures for vorticity numbers around 1 (fig. 4.10e and f).

Figures C.5 and C.6 in Appendix C show fig. 4.10 with the strongest and weakest possible fabric based on the 80% confidence intervals in fig. 4.5. The overall picture is similar. The variation with vorticity number is approximately unchanged and boundaries between the regimes shift by roughly $\pm 7^\circ\text{C}$.

To illustrate the difference in pole figure patterns at the same finite strain but different temperatures and deformation regimes I plot pole figures at a finite strain of $\gamma = 2$ (fig. 4.11) overlaid onto a regime diagram of fabric patterns. The pole figures are centred at the vorticity number and temperature they are simulated at. Figure 4.11 highlights fabrics are still variable despite being in the same regime. The fabric at $\mathcal{W} = 1, T = -5^\circ\text{C}$ is much stronger than the fabric at $\mathcal{W} = 10, T = -30^\circ\text{C}$ or $\mathcal{W} = 0.1, T = -30^\circ\text{C}$, however they are all single-maxima. It is also worth noting the difference in angle of the primary cluster across the parameter space: approximately 0° for $\mathcal{W} = 0.1, T = -30^\circ\text{C}$ but increasing as \mathcal{W} and T increase, as shown in fig. 4.9.

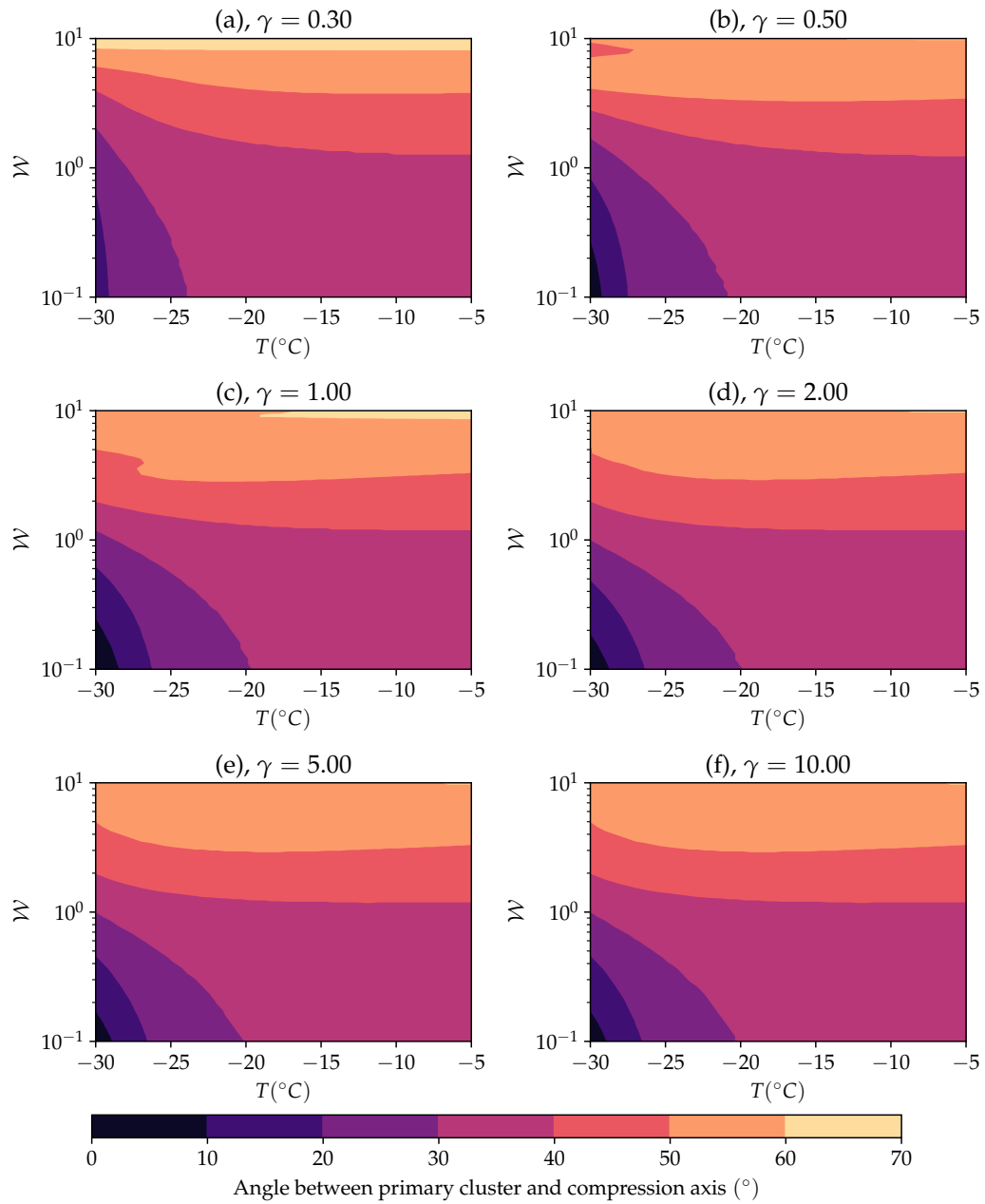


Figure 4.9: Contour plots showing the angle (in degrees) of the largest cluster from the compression axis. Panels are shown for progressively increasing finite strain values. This angle is fairly invariant with finite strain. The resolution of this figure is 50×50 across the parameter space.

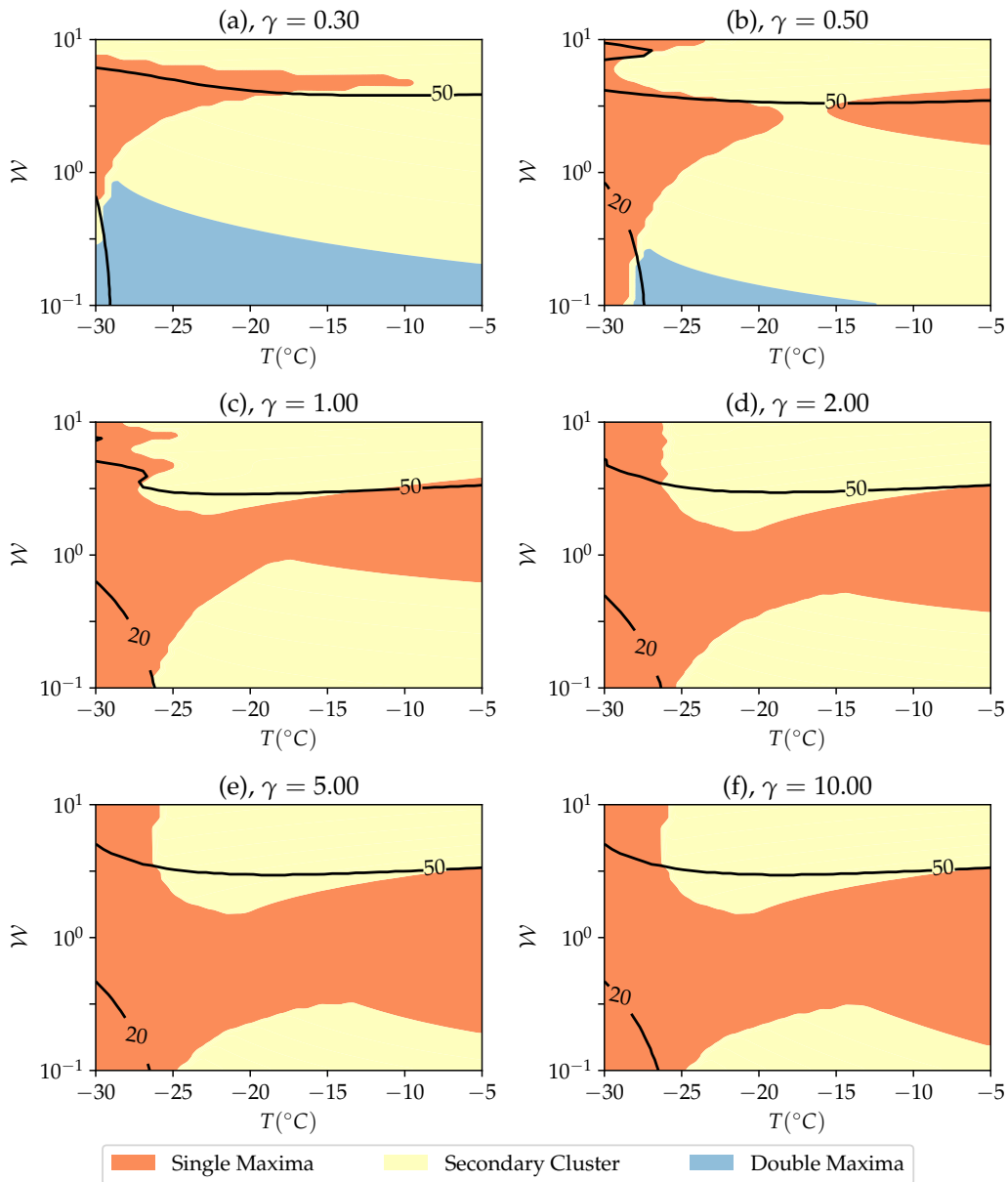


Figure 4.10: Regime diagram of the different fabric patterns which occur (defined in fig. 2.4). The angle of the primary cluster in fig. 4.9 at 20° and 50° is also overlaid. As in fig. 4.9 diagrams are shown for discrete strain values. The resolution of this figure is 50×50 across the parameter space.

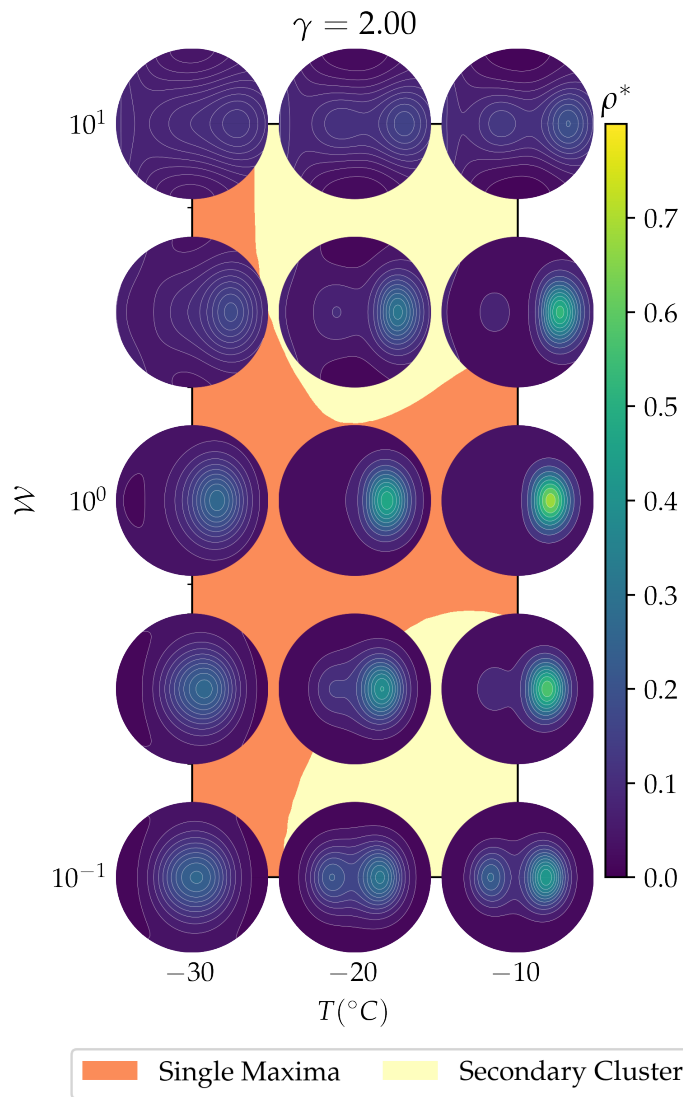


Figure 4.11: Pole figures overlaid onto the regimes at $\gamma = 2$. The pole figures are centred at the vorticity number and temperature they occur.

4.4.3 Analysis of fabric evolution timescales

A variable that is central to the interpretation of ice core fabrics is the timescale or, equivalently in the non-dimensional problem, the finite strain over which fabric evolution occurs. In fig. 4.12 I explore fabric evolution timescales. fig. 4.12a shows the finite strain required to reach halfway to steady state. I also show the J index when the fabric reaches steady state in fig. 4.12b. Both are shown across the space of \mathcal{W} - T . An example showing the evolution of the J index and the finite strain at which it reaches steady state is illustrated in fig. 4.12c.

Figure 4.12a shows the finite strain at which the J -index is halfway to its steady-state value. This can be considered the half-life over which fabric evolution occurs. Measuring the strain at halfway to steady-state gives insight into the timescale over which fabric development occurs and is more robust measure than estimating the strain at steady-state, which I found was sensitive to parameter variations such as those shown in appendix C. Vorticity numbers closest to zero and the coldest temperatures have the highest halfway strain. Under these conditions, neither rigid-body rotation nor migration recrystallization are activated to a significant degree: the fabric evolution is dominated by basal-slip deformation. Fabrics also take longer to develop closer to a vorticity number of 0.7, due to the fact that this vorticity number has the strongest fabrics generally. For $\mathcal{W} > 1$ the strain to reach half strength decreases, as the fabrics are shown to be generally weaker as vorticity number increases. This is clearly seen in fig. 4.12b (showing the J -index at steady-state). Generally, as temperature increases the steady-state fabric always increases in strength. Fabrics are strongest at a vorticity number of around 0.7 across almost the whole temperature space.

Figures C.9 and C.10 in appendix C show fig. 4.12 with the strongest and weakest possible fabric based on the 80% confidence intervals in fig. 4.5. These figures show that the halfway strain is fairly insensitive to changes in the parameters, with the maximum varying by around $\pm 20\%$. The maximum halfway strain remains at $\mathcal{W} = 0.1$, $T = -30^\circ\text{C}$ for both figs. C.9 and C.10. The J index at steady-state is more sensitive to changes in parameters but the general picture of how this variable changes across the \mathcal{W} - T space is similar, with the upper bound showing generally less variation across the parameter space.

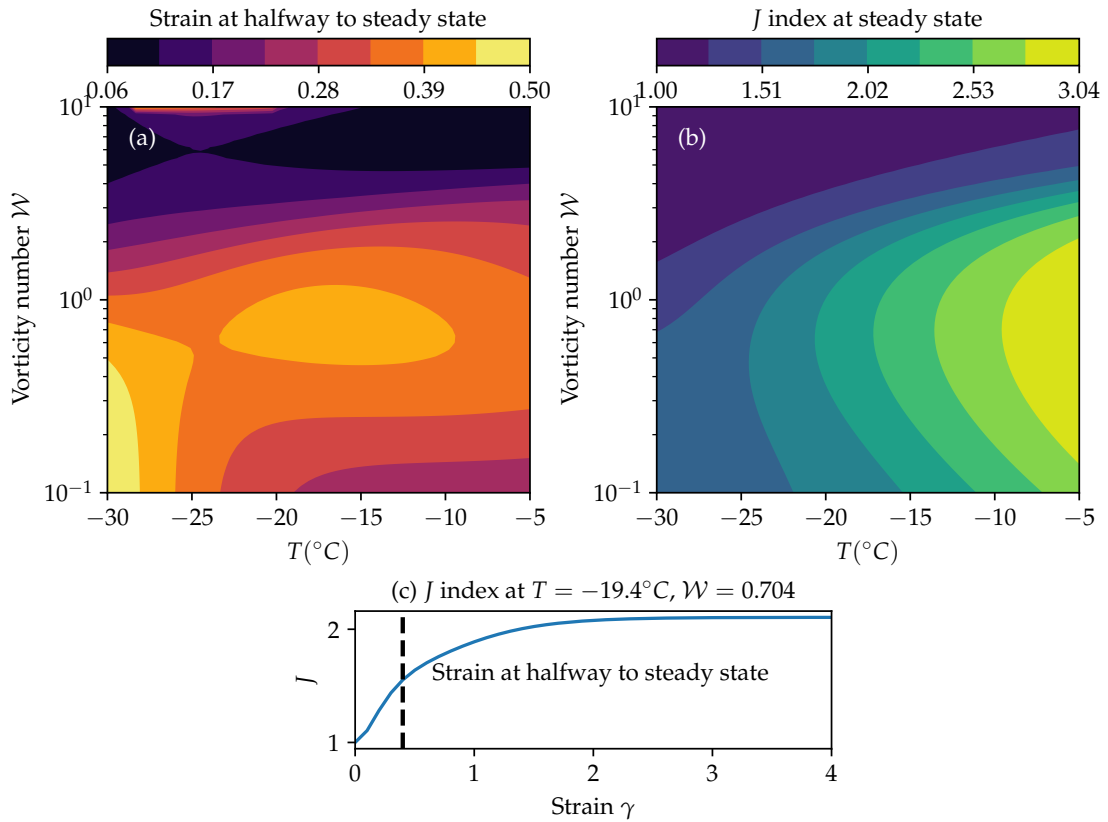


Figure 4.12: Properties of steady-state fabrics across the $\mathcal{W} - T$ parameter space. (a) shows the strain at which the fabric, at constant T and \mathcal{W} , reaches steady-state (defined as a rolling average of the J index over a strain window of 2 gets within 5% of the steady-state value). (b) shows the J index at the steady state. (c) shows the plot of J against strain γ at $T = -30^{\circ}\text{C}$, $\mathcal{W} = 0.01$, with the calculated steady-state strain

4.5 DISCUSSION

The analysis presented here gives predictions for the fabric patterns produced over the whole range of vorticity numbers and temperatures arising for incompressible two-dimensional deformation regimes, a first for fabric modelling. I have limited the analysis here to fabrics produced under a constant two-dimensional deformation regime and temperature. Although ice in the natural world will undergo changing deformation regimes, the analysis presented here is a first step to provide insights into fabrics produced for deformation regimes away from pure and simple shear. Furthermore, the fabrics analysed here are highly relevant for ice deformed in the laboratory, which is in most cases deformed at constant temperature and vorticity number.

Ice in the real world will undergo three-dimensional deformations yet it is common to model ice-sheets in two dimensions along the vertical cross-section, such as in fig. 4.2. This has been shown to be valid around divides such as in Martín et al. (2009). In some regions, such as ice streams, the deformation will be more three dimensional. Nevertheless, exploring general two-dimensional deformations is a good first step away from the isolated, two-dimensional conditions of pure and simple shear alone.

4.5.1 *Fabric patterns across deformation regime and temperature space*

Previous work has focused on modelling fabrics produced at fixed deformation regimes (Llorens et al., 2016), or modelling the deformation experienced by ice at a divide (Bargmann et al., 2012). Due to the computational efficiency of SpecCAF, I have been able to perform thousands of simulations across the parameter space of temperature and vorticity number to show how fabrics vary.

Our work generally shows a smooth transition between the two deformation regimes of pure and simple shear, as can be seen in fig. 4.7. Such intermediate deformation regimes are important in the real world (figs. 4.2 to 4.4) and must be taken into account when considering ice fabrics, rather than focusing on the isolated cases of pure and simple shear.

The weak fabric seen for highly rotational flows has not been studied at all so far. This result is interesting as it shows for the first time the fabric produced by highly rotational deformation regimes: a weak girdle fabric. Throughout these deformation regimes I have kept the

non-dimensional strain-rate constant. Therefore, at high vorticity numbers the weak fabric seen in figs. 4.7 and 4.8 is not caused by a lack of deformation. Instead it is due to the rotational component acting to quickly smear any cluster produced by basal-slip deformation or migration recrystallization to orientations where the cluster is consumed by migration recrystallization. The end result as $\mathcal{W} \rightarrow \infty$ is a very weak girdle fabric with the girdle aligned to the axis of vorticity.

The regime diagram in fig. 4.10 shows the fabric patterns produced across the space of vorticity number, temperature and strain. From experimentally deformed ice, the vast majority of fabrics produced are cone-shape fabrics (see Fan et al. (2020) or the references in fig. 3.5). However, ice deformed in the laboratory in compression can only reach strains of up to $\gamma = 0.5$ and fig. 4.10 highlights how double-maxima fabrics are only present up to these strains. Above $\gamma = 0.5$, secondary cluster and single-maxima patterns are more prevalent. Importantly, secondary cluster fabrics, which have been to-date only seen in simple shear ($\mathcal{W} = 1$), can occur at very low vorticity numbers (fig. 4.10c,d).

Results from Budd et al. (2013) show a secondary cluster fabric for $W = 0.85, \gamma = 0.34$ and $T = -2^\circ \text{C}$. Extrapolating fig. 4.10a would suggest this agrees with the model. Budd et al. (2013) also have another laboratory data point at $\mathcal{W} = 0.52, \gamma = 0.72$ and $T = -2^\circ \text{C}$ which shows a single-maxima pattern. Extrapolating fig. 4.10 would predict a secondary-cluster fabric, however close to boundary where the fabric becomes a single-maxima. Furthermore SpecCAF has only been constrained up to $T = -5^\circ \text{C}$, and as ice approaches the melting point the parameters are likely to behave non-linearly, so a simple extrapolation cannot be relied upon.

4.5.2 *Finite strains required for fabric evolution*

For the interpretation of ice fabrics it is essential that we know the timescale (or in the non-dimensional case here, total finite strain) over which fabrics evolve to steady state. In this chapter I have presented the first assessment of fabric timescales (fig. 4.12), by examining the ‘half-life’ for fabrics to reach steady state. In compression, experiments can only reach a maximum effective strain of $\gamma \approx 0.5$. It is often assumed that a strain of around $\gamma = 0.2$ represents a steady state in the mechanical properties, and consequently in fabric (Jacka, 2000). However, recent experiments show that the fabric continues to evolve

past this (Piazolo et al., 2013; Qi et al., 2017). It is also known that fabrics require higher finite strain to reach steady state in simple shear (Journaux et al., 2019). Qi et al. (2017) notes that fabric data is required at higher strains than has been achieved to date by compression experiments to link to high-strain natural environments. The results in this chapter fill this missing gap. Here I extend analysis of fabric regimes to very high strains of $\gamma = 10$. For low \mathcal{W} , in experiments and in fig. 4.7, a fabric quickly develops at very low strain $\gamma \approx 0.2$, (also seen in Craw et al., 2018). Although the fabric pattern does not change as strain increases, it cannot be said to be in steady-state because the concentration of orientation at the clusters continues to increase. It should be noted that any change in fabric intensity will directly affect the mechanical properties such as the degree of viscous and seismic anisotropy (Duval et al., 1983; Matsuoka et al., 2003).

Figure 4.12a shows that, for very low temperatures ($T \approx -30^\circ \text{C}$) the strain to reach halfway to steady state is the highest, around $\gamma = 0.5$. as can be seen in fig. 4.12c the true steady-state can not be reached to much later as the J index approaches the steady-state value slowly. From this it is safe to remark that reaching true steady states at these temperatures in laboratory experiments will be impossible for deformations close to pure shear. Although fig. 4.12a shows that, above very low temperatures ($T > -24^\circ \text{C}$), deformation regimes closer to simple shear take longer to reach steady-state. However these strains are more achievable in the laboratory as fabrics can be deformed in torsion, allowing very high strains such as $\gamma > 1.5$ to be reached (Journaux et al., 2019). Furthermore, the strain to reach halfway to steady state is primarily dependent on vorticity number \mathcal{W} , rather than temperature.

4.5.3 *Consequences for ice core interpretation*

Analysis and interpretation of ice cores remain key for understanding the processes occurring in the natural world, for both understanding the past climate history (Dansgaard et al., 1969) as well as understanding ice sheet dynamics (Schytt, 1958). The regime diagrams I have constructed (figs. 4.9 and 4.10) can be used as a toolkit to interpret ice cores. For example a single maxima fabric with an angle less than 20° between the compression axis and primary cluster centre implies the core has undergone mostly compression at low temperature. If other constraints such as knowledge the deformation regime history

or temperature has been constant to good approximation, the dominant deformation regime and temperature can be further constrained. As the work here is for constant temperature and vorticity number, any ice core fabric interpretation will inherently assume that an ice core that has been deformed primarily at a dominant temperature and deformation regime over its recent history. Since temperature varies with depth in an ice sheet (Paterson, 1999), this method is likely to be most reliable for ice cores where the ice is primarily moving horizontally i.e. far from ice divides. I also assume an initial random orientation for the fabric. Although deformation regime history in the natural world is likely to be complex, this is a reasonable assumption because ice formed from surface accumulation will initially have a random distribution of orientations (Montagnat et al., 2020).

The fabric pattern is a robust way to interpret ice cores, as it requires no assumptions about the deformation regime direction. This can be accomplished by the regime diagram we present in fig. 4.10. For example, the presence of double-maxima fabrics (two equal strength clusters) implies that the fabric has undergone a relatively low strain. A secondary cluster fabric implies that the fabric is likely to be at intermediate strains, and at temperatures $T > -20^\circ \text{C}$. A fabric which both has a low J index and a secondary cluster implies a highly rotational deformation regime $W > 3$. Furthermore, I have shown that the presence of a fabric which appears to be isotropic could be indicative not only of no deformation, but also of a highly rotational deformation regimes.

If other information about the fabric history is known, figs. 4.9 and 4.10 can be used in combination to extend this knowledge. For example, if there are independent constraints on the orientation of the deformation regime axis, then the angle of the primary cluster can be used to interpret ice cores as well. As can be seen in fig. 4.9 the angle between the primary cluster and the compression axis is relatively invariant with strain. Knowing this angle can therefore give a good estimate of the vorticity number and temperature, for deformation regimes which are primarily 2D.

4.5.4 *Implications for ice flow properties and modelling*

Viscous anisotropy of ice is controlled by the fabric and is a key control of the flow field (e.g. Alley, 1988). This anisotropy is dependent on the pattern, direction and strength of the fabric. The current approach

common in ice-sheet models is to represent anisotropy with an enhancement factor which scales the viscosity, either globally (Graham et al., 2018) or locally as in Placidi et al. (2010) (eq. (2.17)). The model SpecCAF used in this chapter can be coupled with any anisotropic viscosity formulation to include directional variation in viscosity. Martín et al. (2009) has coupled a fabric model to an anisotropic viscosity, but the fabric evolution model used did not include recrystallization, which are dominant processes in controlling fabric evolution and their approach to final steady states. The high sensitivity of fabric strength and patterns to temperature shown in this chapter and in experimental work (Qi et al., 2019) may lead to further interesting flow features on top of those caused by anisotropy alone. This can only be captured with a coupled fabric model including a temperature dependent fabric. Temperature can also affect the flow through viscous heating (e.g. Hindmarsh, 2004) and a temperature dependent fabric model coupled to anisotropic viscosity such as Gillet-Chaulet et al. (2005) would allow us to understand what proportion of the effects of temperature are a consequence of viscous heating and what proportion arise through temperature induced changes to the fabric.

The fabrics I have shown here give insight into where anisotropy may be most important in an ice sheet. Areas with strong fabrics will be highly anisotropic, with the viscosity varying in different directions. Anisotropic flow is not well studied but initial simulations with coupled anisotropic flow show it can explain hitherto unexplained observations such as syncline patterns observed under ice divides (Martín et al., 2009). My analysis of fabrics produced in highly rotational deformation regimes showing an almost isotropic fabric (as seen in fig. 4.7 and fig. 4.12b). This implies that in the regions of Antarctica where the flow is highly rotational, which as we can see in fig. 4.4 does occur, the fabric will evolve towards a state with limited anisotropy. However areas of approximately simple shear ($\mathcal{W} = 1$) show the strongest fabrics and hence the strongest effect of anisotropy. This means viscous anisotropic affects are expected to be widespread, further motivating the need to fully represent them in models. In future work it would be possible to explore how seismic wave velocities vary with the different fabrics modelled in this chapter, again comparing to real-world observations.

4.6 CONCLUSIONS

Prediction of fabric evolution is pivotal for the correct interpretation of ice core fabrics and reliably predicting ice losses in a changing climate using ice-sheet modelling. This work extends our ability to predict fabric evolution from the end-member deformation regimes of pure and simple shear to general two-dimensional deformation regimes. As such the presented study represents a step towards understanding fabrics in fully general conditions which is key for understanding viscous anisotropy and, in turn, large-scale ice-sheet flow modelling. I have shown that deformation regimes outside of pure and simple shear are important in common flow scenarios seen in ice sheets. There is the potential for future work to extend the modelled fabrics to calculate seismic anisotropic properties, enabling us to further improve our understanding of ice in natural flows.

The regime diagrams presented are a useful tool to help with the interpretation of ice core data. In combination with other information, such as the plane of deformation regime or an estimate of the temperature at which a core was deformed, these regime diagrams can be used to determine the primary deformation regime and temperature undergone by an ice core. I have shown that for two-dimensional deformations, the double-maxima fabric is not present at high strains when only a small amount of vorticity is present in the deformation regime $\mathcal{W} > 0.1$. This is important as many laboratory experiments are performed for $\mathcal{W} = 0$. Future work could investigate whether this conclusion extends to three-dimensional cone-shape fabrics.

Highly rotational deformation regimes were investigated for the first time and showed a weak girdle fabric aligned to the axis of vorticity. I have also shown how the timescale for fabric evolution, shown by the halfway strain to reach steady state, changes over the parameter space. Laboratory experiments around simple shear may be able to reach the strains required to get close to steady state, however compression experiments, especially at low temperatures cannot achieve the required strains for steady state.

NUMERICAL MODELLING OF ICE STREAM FABRICS: IMPLICATIONS FOR RECRYSTALLIZATION PROCESSES AND BASAL SLIP CONDITIONS

ABSTRACT

Accurately predicting ice crystal fabrics is key to understanding the processes and deformation in ice-sheets. In previous chapters I have shown that the SpecCAF model is capable of reproducing ice fabrics observed from laboratory experiments. In this chapter, for the first time, a numerical fabric model is used to predict the fabric evolution with an active ice stream. This is done by predicting the fabrics at the [EGRIP](#) ice core site. I do this using satellite data and inferred particle paths, combined with the shallow ice approximation (with basal slip) to infer a leading order approximation for the deformation through the ice sheet. I find that SpecCAF is able to predict the patterns observed at [EGRIP](#) - a girdle/horizontal maxima fabric perpendicular to the flow direction. By reducing the rate of rotational recrystallization in the model I am also able to predict the fabric strength at [EGRIP](#). As I have previously found rotational recrystallization is mostly temperature independent, this suggests rotational recrystallization may be primarily strain-rate/stress dependent. These results show SpecCAF can be applied to real-world conditions and provide insights into the deformation and basal-conditions of the ice sheet. As the model only considers deformation and recrystallization through dislocation creep, the results imply that - for the ice stream modelled - no other process is significantly influencing both the produced ice fabric and the deformation. I find that the model gives best results for full slip at the base of the ice sheet, implying that the level of sliding at the base of the ice sheet in the North Greenland Ice stream may be very high. The approach taken in this chapter could be extended to other ice core locations in Greenland and Antarctica.

5.1 INTRODUCTION

Understanding the flow of ice sheets is key for accurately predicting sea-level rise (Shepherd et al., 2018). By more accurately modelling the fabric of ice, we will improve the uncertainty in sea-level rise predic-

tions. Accurate fabric models are the first step to incorporate viscous anisotropy in ice sheet models. Furthermore, improved modelling of ice fabrics enables us to investigate natural ice core fabrics in detail focussing on possible deformation mechanisms, boundary conditions of flow and flow evolution.

Numerical modelling of ice fabrics has either aimed to match laboratory experiments, e.g. chapter 3 in this thesis (also published as Richards et al. (2021b)), or Llorens et al. (2016), or aimed to predict fabrics at or near to ice divides (Bargmann et al., 2012; Castelnau et al., 1996; Montagnat et al., 2012; Seddik et al., 2008). The majority of ice cores are taken at ice divides as they give reliable climate data. However, in order to give reliable climate data the deformation is minimal. Therefore the fabrics produced here are already well studied and not representative of conditions in the rest of the ice sheet.

In contrast to ice divides, some of the most dynamic regions in an ice sheet are ice streams, where there is slip at the base of the ice sheet and the ice flows much faster than other regions. These are key for controlling the mass loss from ice sheets (Bennett, 2003). Recently a drill site has been setup in east Greenland in an ice stream. This is called the East Greenland Ice Core Project, and fabric data from drilled ice core data is now available here (Stoll, 2019; Westhoff et al., 2020)

In previous chapters I have introduced the SpecCAF model, and shown it agrees well with laboratory experiments. Here I use this model to predict the fabrics at EGRIP to test: a) the applicability of SpecCAF to natural ice fabrics which originated from ice flowing at 4-7 orders of magnitude lower strain rates than ice deformed in the laboratory, i.e 10^{-12} to 10^{-10} versus 10^{-6} to 10^{-5} s^{-1} , and b) infer properties deep into the ice sheet.

These tests are a clear way forward in our ability to predict ice flow dynamics. For example, accurately modelling fabrics from real-world ice sheets is key as a step towards accurately modelling viscous anisotropy in ice sheets. Furthermore, reproducing real-world fabrics enables us to infer conditions deep into an ice sheet, such as temperature, basal drag, levels of strain partitioning and the value of the flow law parameter n .

Predicting ice fabrics from real-world locations is more challenging than those from well confined laboratory experiments (e.g. Budd et al., 2013; Qi et al., 2019) as they have a complex and changing deformation and temperature history. Here I present and test an approach which is based on combing predictions for the upstream flow path from

satellite data with leading order assumptions to estimate the velocity gradient at depth into an ice sheet upstream of the ice core site. I then use this calculated deformation as an input into SpecCAF to predict the fabric evolution. For this study, I use the [EGRIP](#) site as (a) the site is in an ice stream, a critical region for controlling the mass loss from the ice-sheet an ice stream (Bennett, 2003), and (b) there is detailed fabric data from drilled ice cores (Stoll, 2019), including for the first time azimuthal constraint on the ice core orientation (Westhoff et al., 2020).

5.2 BACKGROUND

In this background, I first review the shallow ice and shelf approximations. This is because I use these approximations to derive an approximation for the velocity gradient throughout the ice sheet from the satellite data - this is described later in section [5.3](#). I then give details of the [EGRIP](#) site and the ice core data currently available from here.

5.2.1 *Shallow ice and shallow shelf approximations*

In ice-sheet modelling, due to the complexity of solving the full Stokes equations, simplifications are often made by neglecting smaller terms in the force balance of an ice sheet. The simplest models, for a grounded ice sheet and for a floating ice shelf (over the ocean) are the Shallow Ice Approximation ([SIA](#)) and the Shallow Shelf Approximation ([SSA](#)) respectively. As the name suggests, these simplifications can be made because the ice sheet length is much greater than its thickness (i.e. the ice sheet is shallow). Kirchner et al. (2011) provides a review of the usefulness and limitations of these models. Figure [5.1](#) shows the vertical velocity profile for both the [SIA](#) and [SSA](#), as well as for a mix of the two valid for an ice stream.

The [SIA](#) is derived by assuming that vertical shear stresses (S_{xz} and S_{yz}) dominate in the force balance for an ice sheet, and retaining only the leading order terms. The [SIA](#) is valid both for regions with no slip at the base, and also regions with limited basal slip. Its validity breaks down for regions of high basal slip, such as ice shelves where the ice is floating on water. If the surface velocity and level of slip at the base are known, the [SIA](#) can be used to derive a vertical velocity profile through the ice sheet depth (fig. [5.1a](#)).

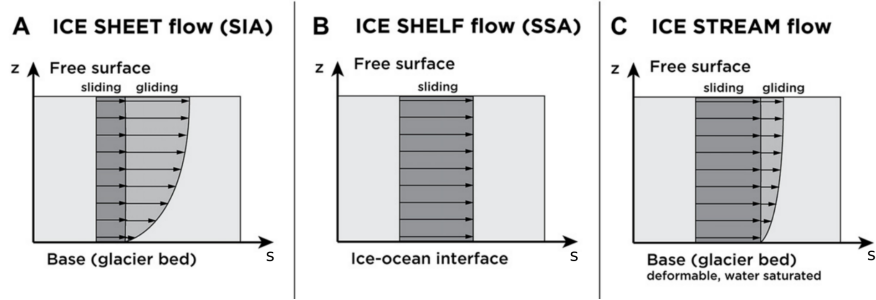


Figure 5.1: Adapted from Kirchner et al. (2011), showing the vertical velocity profile for the a) shallow ice approximation, b) shallow shelf approximation, and c) a mix of the two, valid for an ice stream such as at EGRIP.

The SSA, valid for ice shelves retains the xy normal and parallel shear stresses as well as the vertical shear stresses. As can be seen in fig. 5.1b, to a first approximation the vertical velocity profile is uniform with depth.

5.2.2 The EGRIP site

Historically, ice cores have been drilled at or close to divides, with the aim of having minimal deformation to give accurate paleoclimate data. Consequently there is much data from ice cores at or near divides (e.g. Dansgaard et al., 1969; Gow, 1961; Thorsteinsson et al., 1997), but from a deformation perspective the limited data from fast flowing locations is more interesting. EGRIP aims to provide exactly such data by retrieving ice cores from the fast-flowing North East Greenland Ice Stream (NEGIS), the largest ice stream in Greenland. This is shown in fig. 5.2. Figure 5.2a shows an overview of Greenland, contoured by velocity magnitude from satellite data (Joughin et al., 2018). Figure 5.2b shows a zoomed in region (highlighted by the rectangle in fig. 5.2a) showing the location of the EGRIP and GRIP drill sites. The tracked upstream path from Gerber et al. (2021) (discussed later) is also shown.

Ice fabric data from EGRIP has been published in Stoll (2019) and Westhoff et al. (2020). It should be noted the ice core drilling is ongoing with more fabric data at deeper depths yet to be published. Nevertheless data is available to a depth of 2100 m. Analysis of the eigenvalues of the second-order orientation tensor from fabric samples shows a transition from approximately isotropic (all eigenvalues = $1/3$) near the surface to eigenvalues of approximately 0.7, 0.3, 0 below 600 m.

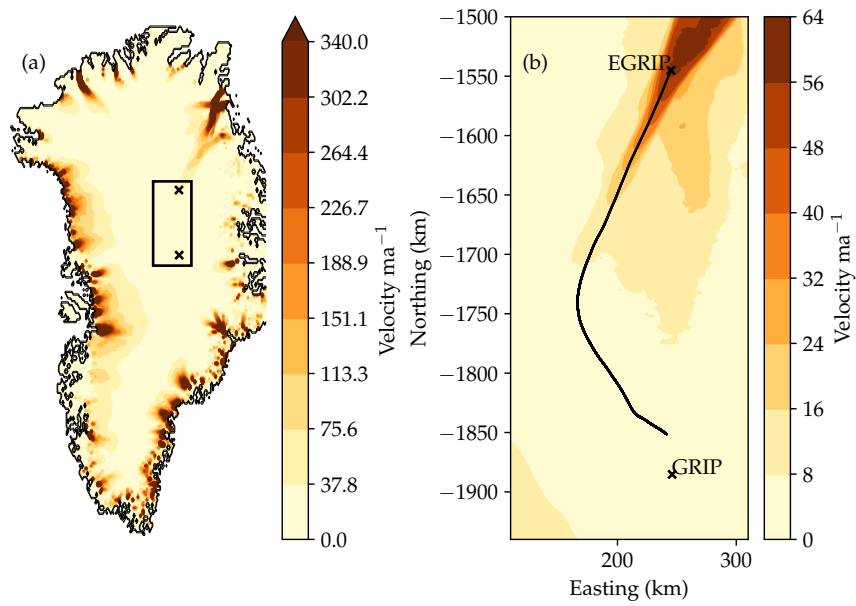


Figure 5.2: View showing an overview of Greenland in (a), showing the velocity magnitude calculated from Joughin et al. (2018) and a rectangle describing the inset region in (b), which shows the tracked plan-view path upstream of the EGRIP ice core location. The location of the GRIP core is also shown.

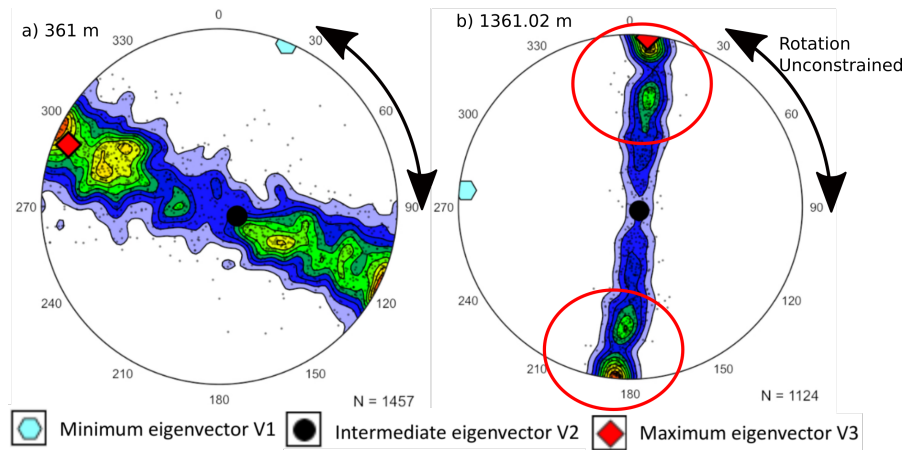


Figure 5.3: Pole figure from Stoll (2019), at a depth of 1361.02 m. This shows both a girdle pattern, but also two horizontal maxima. The pole figure is shown with the z -axis out of the page. Note that the orientation of the pole figure is unconstrained when rotating about the z axis. This is because when ice cores are drilled they are free to rotate and this information is usually lost.

The eigenvalue plot with depth also exhibits oscillations below 550 m. These oscillations are hypothesised to be caused by strain partitioning (Stoll, 2019), where local deformation differs from the regional deformation.

Stoll (2019) reports a girdle fabric between 350-1300 m. Below this depth they report a horizontal-maxima fabric. This is similar to the girdle fabric but exhibits clusters orientated normal to the z -axis. Pole figures from depths of 361 m and 1361 m are shown in fig. 5.3, adapted from Stoll (2019). Note that the orientation of the pole figures are unconstrained when rotating about the normal axis. This is because when ice cores are drilled they are free to rotate and therefore the directional data in the horizontal. Recent work seeks to recover this (Westhoff et al., 2020) but is currently not available for this pole figure. For fig. 5.3a a girdle pattern is visible. For fig. 5.3b the girdle pattern is still visible, but there are also two very strong clusters approximately perpendicular to the z -axis, highlighted in red. This correlates with the eigenvalue plot, as a evenly-distributed girdle fabric would be characterised by the largest two eigenvalues being equal (e.g. Gagliardini et al., 2009).

As discussed above, historically ice core samples are unconstrained in the $x - y$ plane. This means the angle of the girdle in fig. 5.3 is

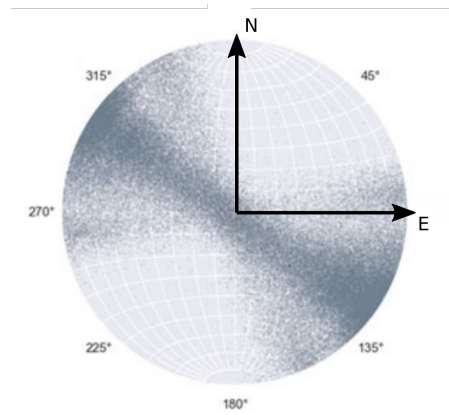


Figure 5.4: Girdle fabric from Westhoff et al. (2020), where the orientation of the girdle has been found. This figure shows c -axis data averaged over a depth 1400 – 2100 m. The pole figure is shown with the z -axis out of the page, North at 0° . The girdle is perpendicular to the flow-direction.

unknown. A recent advance (Westhoff et al., 2020) has allowed this to be found for the first time, so the ice core fabric can be compared directly to 3D ice fabrics from models. This has been done using fabrics from EGRIP as an example. Westhoff et al. (2020) found that the girdle fabrics from EGRIP were aligned perpendicular to the local flow direction. This is shown in fig. 5.4. From this work, we would expect the girdle fabrics seen at other depths in EGRIP, such as fig. 5.3 to be orientated in the same direction. This also agrees with data from other fast-flowing regions: Lutz et al. (2020) performed seismic measurements at a site in the Ross ice shelf in Antarctica. They estimated a combined girdle and horizontal maxima, approximately perpendicular to the flow direction from seismic measurements.

Gerber et al. (2021) has calculated the upstream particle path from the EGRIP site. They also calculate values for past accumulation rates, the surface height along the flow line and the level of slip at the base of the ice sheet. They do this by using age-depth data from radar measurements and simplified profiles for the vertical strain rate (Dansgaard and Johnsen, 1969), and vertical velocity profile (Grinsted and Dahl-Jensen, 2002).

5.3 METHODS

In order to predict the fabric of an ice core using the information available we must know (a) the deformation history, i.e. to as full extent as possible all terms in the velocity gradient tensor $\nabla \mathbf{u}$, and (b) the temperature history. I aim to trace the path of the ice core back in time to the point where it fell as snow. Here I can safely assume the fabric has an initial isotropic condition. I use satellite data for the velocity with a resolution of 250 m (Joughin et al., 2018) alongside data from Morlighem et al. (2017) for the bed and surface elevation, with a resolution of 150 m, and data from Ettema et al. (2009) for the surface accumulation rate, with a resolution of 1 km. I use the plan-view path shown in fig. 5.2, and corresponding surface derivatives from Gerber et al. (2021).

5.3.1 Deformation history

Once the plan view path is calculated, the surface derivatives $\partial u_s / \partial x$, $\partial u_s / \partial y$, $\partial v_s / \partial x$, $\partial v_s / \partial y$ can be calculated along the path. This is already done by Gerber et al. (2021). In order to arrive at an estimate for all the terms in the velocity gradient $\nabla \mathbf{u}$, along the three-dimensional path, I make the following assumptions:

1. I neglect the derivatives $\partial w / \partial x$, $\partial w / \partial y$, as order of magnitude analysis shows

$$O\left(\frac{\partial u}{\partial x}\right) \sim \frac{U}{L}, \quad O\left(\frac{\partial w}{\partial x}\right) \sim \frac{U\tau}{L^2}$$

where U , τ and L are the characteristic velocity, thickness and length of the ice-sheet. As $\tau \ll L$ the additional factor of τ/L means these derivatives are small compared to others.

2. The vertical gradients are not small and it is important to estimate them reliably. To do this I use the shallow ice approximation to estimate the vertical velocity profile, with variable slip at the base of the ice sheet:

$$u(z) = u_s \left(1 - \left(1 - \frac{u_b}{u_s} \right) \tilde{d}^{n+1} \right), \quad (5.1)$$

where u_s is the surface velocity and u_b is the basal velocity. The non-dimensional depth is $\tilde{d} = (h - z) / (h - b)$, where h is the height of the ice surface and b is the base. The parameter n is the

power from Glen's law (eq. (2.3)). Here I use $n = 3$. This profile arises from assuming vertical shear stresses are dominant, and this may not be the case at EGRIP as it is in an ice stream. However, the velocity profile recovers to the leading order estimate from the SSA when there is no basal drag (fig. 5.1b) Therefore we can use this as a leading-order estimate of the vertical velocity profile for any level of basal slip. From eq. (5.1) the vertical derivatives can be estimated as a function of the basal slip ratio u_b/u_s .

Furthermore estimates for $\partial u/\partial x$, $\partial u/\partial y$, $\partial v/\partial x$, $\partial v/\partial y$ at depth are given by:

$$\frac{\partial u}{\partial x} = \frac{\partial u_s}{\partial x} \left(1 - \left(1 - \frac{u_b}{u_s} \right) \bar{d}^{n+1} \right). \quad (5.2)$$

Once $\partial u/\partial x$ and $\partial v/\partial y$ are known, $\partial w/\partial z$ can be calculated by using $\nabla \cdot \mathbf{u} = 0$.

This gives us leading order estimates for all terms in the velocity gradient. The xy variation is accounted for by the satellite data, and the z variation is defined by the vertical velocity profile.

To define a fully three-dimensional path a location upstream is chosen. At the surface, when the ice falls as snow the the vertical velocity is given by the accumulation rate at that location (Arthern et al., 2006; Milani et al., 2018), combined with the vertical velocity arising from the surface slope:

$$w_s = -\dot{a} + u_s \frac{\partial h}{\partial s}. \quad (5.3)$$

Using the above equation the three-dimensional particle path can be integrated forwards from the start point somewhere along the plan view path, to a location at some depth at the EGRIP site. The accumulation rate from Milani et al. (2018) may not be valid for the time the ice core samples were deposited as snow. This discrepancy can lead to streamline paths crossing in the results, however the predicted fabric-depth relationship is not sensitive to this. An alternative approach, as in Gerber et al. (2021), could be to allow \dot{a} to be a free parameter which can be fit to give streamlines which do not cross (for each assumed vertical velocity profile). However, the approach I use here avoids introducing extra fitting parameters.

5.3.2 Temperature history

The temperature history must be defined as an input to SpecCAF. Data from Prior-Jones et al. (2021) gives estimates for the temperature at EGRIP with depth. Once the sensor has cooled to the surroundings, it stays roughly constant at -30°C . In order to know the temperature history upstream, I make another assumption.

3. I assume the temperature profile as a function of depth is the same upstream as at the EGRIP borehole location.

Therefore I use $T = -30^{\circ}\text{C}$ throughout.

5.3.3 Dimensional form of SpecCAF

As I am now simulating real-world dynamics I work with SpecCAF in dimensional form:

$$\frac{D\rho^*}{Dt} = -\nabla^* \cdot [\rho^* \mathbf{v}^*] + \lambda \nabla^{*2}(\rho^*) + \beta(\mathcal{D}^* - \langle \mathcal{D}^* \rangle) \rho^*. \quad (5.4)$$

Now I am tracking the change in the material derivative of ρ^* as I am tracking an ice block in a Lagrangian frame. I use the same parameters as in fig. 4.5 in chapter 4. However as the equations are no longer non-dimensionalised the recrystallization parameters are multiplied by the strain-rate:

$$\begin{aligned} \lambda &= \tilde{\lambda}(T) \dot{\gamma} \\ \beta &= \tilde{\beta}(T) \dot{\gamma}, \end{aligned} \quad (5.5)$$

where $\dot{\gamma} = \sqrt{D_{ij}D_{ij}/2}$ as in chapter 4. We now have a fully-constrained model and the required inputs to predict the fabrics of a drilled ice-core.

5.4 RESULTS

In figs. 5.5 and 5.6 I show the fabrics predicted at EGRIP with depth, as well as their evolution history along the calculated streamlines. fig. 5.5 shows the fabrics for $u_b = u_s$, i.e. with no vertical shear. fig. 5.5a shows a plot of the streamline paths with depth along the streamline. The streamline paths from the surface to depths at EGRIP can be seen. For two paths, the fabric evolution is shown from isotropic at the the surface to EGRIP. For fig. 5.5a, the pole figure axes are aligned with the

axes of the plot: the horizontal axis of the pole figure is aligned with the streamline coordinate, and the vertical axis is aligned with the z -axis. The lower path, which starts close to a divide, shows the fabric initially developing a weak single-maximum corresponding to vertical compression, before developing into a horizontal maxima around 100 km upstream. The upper path develops a similar fabric at similar distances upstream.

Note in fig. 5.5a, and in later figures, two of the streamlines cross. This suggests some of the upstream data, such as surface velocity or accumulation, changed over time. Even though such a cross over is not realistic, the results are still valid as the fabric eigenvalues reported at EGRIP are insensitive to the crossing streamlines, which happens far upstream.

Figure 5.5b shows the eigenvalues of the fabrics at EGRIP against depth as scatter points. This is plotted alongside a best-fit line from EGRIP core data from Stoll (2019). Also, pole figures are plotted on the right hand side, with the same normal as fig. 5.4. The fabric predicted by the model is much weaker than that seen from Stoll (2019). However, the results from EGRIP at these depths show a fabric pattern which is between a girdle and horizontal maxima (as seen in fig. 5.3) with the girdle perpendicular to the flow direction fig. 5.4 from Westhoff et al. (2020). This agrees with the pattern seen in fig. 5.5b. However, the pattern predicted (a girdle fabric also exhibiting horizontal maxima, aligned perpendicular to the flow direction) is in good agreement with Stoll (2019) and Westhoff et al. (2020). It is also interesting to note that the fabric is roughly invariant with depth.

Figure 5.6 shows the same as fig. 5.5, but for $u_b = 0$ (SIA with no basal slip). Figure 5.6a shows that the fabric pattern on the lower path retains a single-maximum throughout, as the deformation changes from compression to simple shear. The eigenvalues in fig. 5.6b show a stronger fabric compared to fig. 5.5b, however the fabric is still weaker than the data from EGRIP. Furthermore the vertical shear dominates the deformation below a depth of around 750 m, producing a single-maximum fabric orientation with the z -axis. This is not seen at EGRIP.

5.4.1 *The effect of slip at the base of the ice sheet on fabric development throughout an ice stream*

The above models represent endmember models in terms of boundary conditions for flow. To explore the effect of boundary conditions I

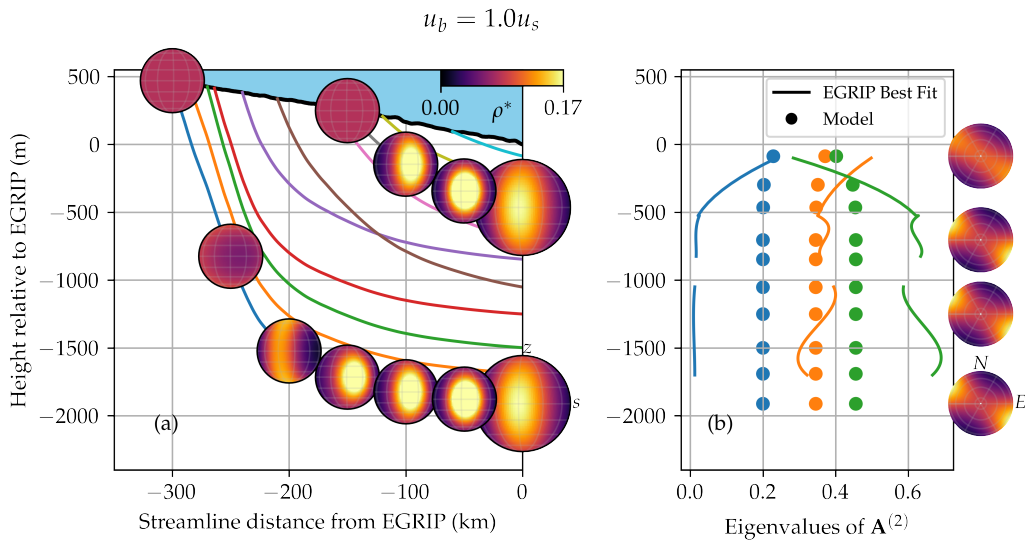


Figure 5.5: Figure for $u_b = u_s$ (no vertical shear) showing (a): 3D streamline paths and pole-figures aligned with the streamline axis (s, z) and (b): the eigenvalues of $\mathbf{A}^{(2)}$ with depth, and pole figures from the model output aligned with the North and East directions at the corresponding depths (the same orientation as fig. 5.4.) Note some streamlines cross due to changes in accumulation with time, this is discussed in section 3.4.

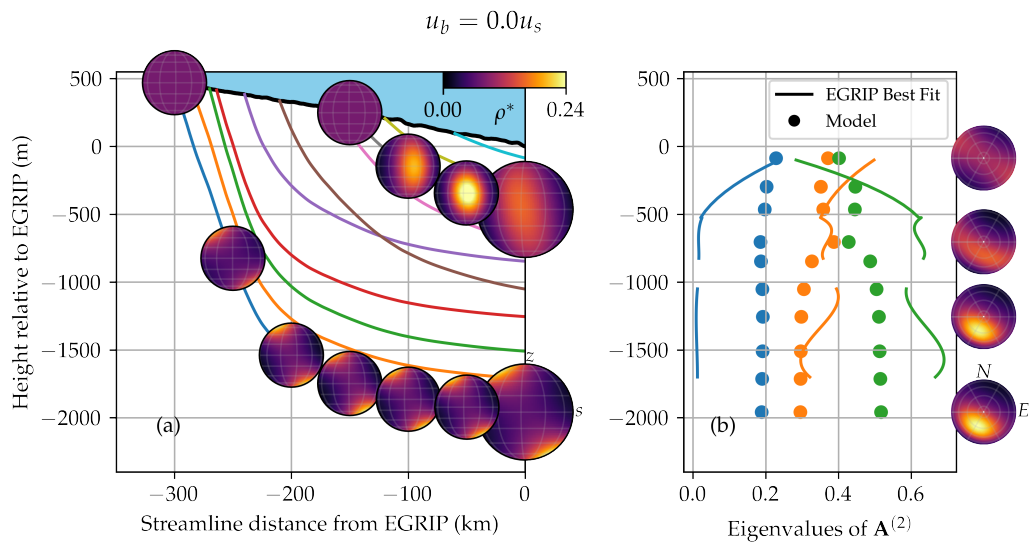


Figure 5.6: Figure for $u_b = 0$ showing (a): 3D streamline paths and pole-figures aligned with the streamline axis (s, z) and (b): the eigenvalues of $\mathbf{A}^{(2)}$ with depth, and pole figures from the model output aligned with the North and East directions at the corresponding depths (the same orientation as fig. 5.4.) Note some streamlines cross due to changes in accumulation with time, this is discussed in section 3.4.

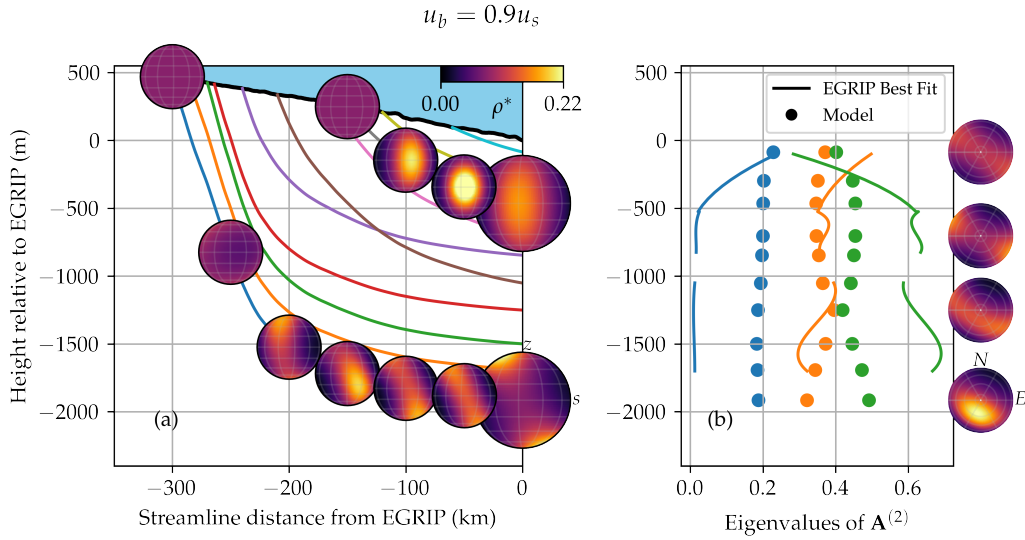


Figure 5.7: Figure for $u_b = 0.9u_s$ (basal velocity 90% the surface velocity) showing (a): 3D streamline paths and pole-figures aligned with the streamline axis (s, z) and (b): the eigenvalues of $A^{(2)}$ with depth, and pole figures from the model output aligned with the North and East directions at the corresponding depths (the same orientation as fig. 5.4.) Note some streamlines cross due to changes in accumulation with time, this is discussed in section 3.4.

modelled fabric evolution for an intermediate value of $u_b = 0.9u_s$ in fig. 5.7. At depths above 1500 m the fabric and eigenvalues are similar to fig. 5.5. However there is also an oscillation in the eigenvalues seen in fig. 5.7b, similar to that seen in Stoll (2019). There is also a clear transition between a girdle/horizontal maxima fabric at depths of above ~ 1500 m, and a single-maxima below. This can also be seen in the eigenvalue plot. Below 1500 m vertical shear becomes dominant leading to a single-maxima. Interestingly, the EGRIP ice core does not show this transition to a single-maxima, even to depths of 2100 m (as deep as data is currently available).

In figs. 5.5 to 5.7 I have used a constant u_b/u_s (the ratio of the basal velocity to the surface velocity) throughout the whole upstream path of the ice stream. However the level of basal sliding would be expected to vary, with $u_b \approx 0$ near ice divides and $u_b \approx u_s$ in an ice stream. Gerber et al. (2021) calculated the value of u_b/u_s along a streamline traced backwards from EGRIP, and this is shown in fig. 5.8. u_b/u_s is close to 0, until the path enters the ice stream where it rises. Close to EGRIP u_b/u_s

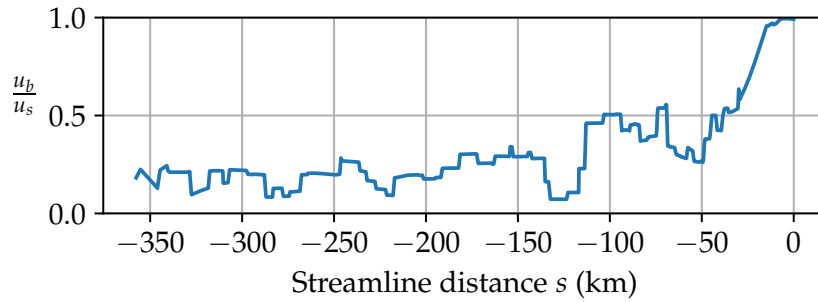


Figure 5.8: Plot of the calculated value of u_b/u_s from Gerber et al. (2021) along the streamline, used in fig. 5.9

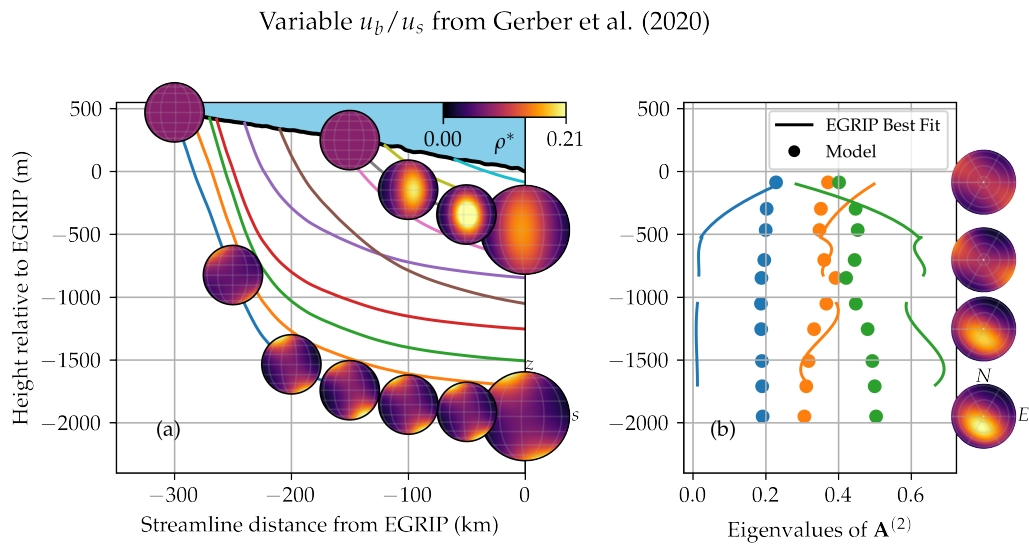


Figure 5.9: Figure like figs. 5.5 and 5.6 for a variable $\frac{u_b}{u_s}(s)$, from Gerber et al. (2021)

is estimated to be one, i.e. almost no vertical shear. Figure 5.9 shows the fabrics produced with this variable u_b/u_s . However, the suggested value of u_b/u_s appears to predict fabrics which do not agree with Stoll (2019). Although the middle eigenvalue matches, a single-maxima fabric is produced, rather than the girdle fabric seen at EGRIP.

5.4.2 Strain-rate dependence of rotational recrystallization

The fact that fig. 5.5 (with full sliding at the base) is the case which best matches the observed pattern at EGRIP, but has all eigenvalues too close to $1/3$ implies that the modelled fabric intensity is too low. In

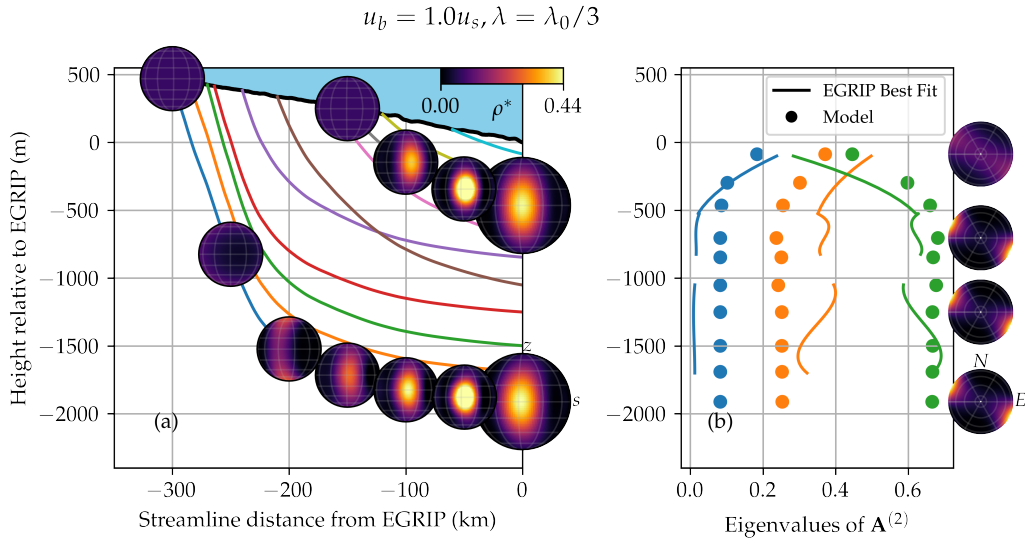


Figure 5.10: Figure like fig. 5.5 with $u_b = u_s$ but $\lambda = \lambda_0/3$, where λ is the parameter controlling rotational recrystallization.

other words, in the real world the fabric pattern is stronger and crystal orientations less ‘smeared’ out than in the model e.g. fig. 5.3b. This can be qualitatively explained by a too significant influence of rotational recrystallization which is modelled as a diffusional process that moves the fabric to isotropic. Consequently, a high contribution of rotation recrystallization will result in a less intense fabric pattern. To test this I reduce λ , the parameter controlling rotational recrystallization, by a factor of 3 while keeping all other parameters the same. This is shown in fig. 5.10, which has the same value of $u_b/u_s = 1$ as fig. 5.5. As can be seen in fig. 5.10 this gives much better agreement to the results from Stoll (2019). The smallest eigenvalue matches very well with the best fit line. The largest eigenvalue is slightly too high (correspondingly the 2nd eigenvalue is slightly too low), but the overall the fit is good. This leads to the horizontal maxima reported in Stoll (2019), with the maxima perpendicular to the flow direction. I note that this figure is for $u_b = u_s$, so there is no vertical shear.

5.5 DISCUSSION

5.5.1 Girdle & horizontal maxima perpendicular to the flow

The recent work by Westhoff et al. (2020) allows the orientation of ice cores normal to the z -axis to be found for the first time. This reveals

the fabric pattern at EGRIP to be a girdle or a horizontal maxima, both orientated perpendicular to the flow direction fig. 5.4. Similar patterns are seen at other ice streams from radar data (Booth et al., 2020; Lutz et al., 2020). This pattern and orientation is also produced by the model in figs. 5.5 and 5.10, when u_b/u_s is close to 1. The horizontal maxima, seen at depths > 1300 m, is left as an open question in Stoll (2019). Here, the horizontal maxima is also present in the results for $u_b = u_s$, hence we can rule out a cause by vertical shear. In the model, the girdle pattern is caused by the flow accelerating along the ice stream, and the horizontal maxima can be explained by shear perpendicular to the streamline, which will occur off the centre line of EGRIP. The fabric seen is a combination of these two flow regimes, acting through basal-slip deformation. The work here shows that this pattern can be explained by our current understanding of basal-slip deformation (represented in SpecCAF), and the leading order approximation for the flow deformation.

5.5.2 Oscillation in eigenvalues

The plot of eigenvalues of $\mathbf{A}^{(2)}$ at EGRIP from Stoll (2019) shows both a short (~ 150 m) and long (~ 800 m) wavelength oscillation in the eigenvalues with depth. Longer wavelength oscillations can also be seen in the model data, caused by the fabric pattern transitioning as vertical shear increases with depth. Therefore this longer wavelength change is expected from the zero-th order flow approximation. However the shorter wavelength oscillation is not seen in my results. Stoll (2019) attributes this to strain partitioning, i.e. where local deformation differs from the regional deformation (Carreras et al., 2013). The fact that this short wavelength oscillation is not seen in the model results here supports the hypothesis that it is caused by local deformation affects.

5.5.3 Fabric strength & rotational recrystallization

Figures 5.5 and 5.6 show that for whatever value of u_b/u_s , the parameters derived from experiments are not able to predict the fabric strength - characterised by the magnitude of the largest eigenvalue - seen in Stoll (2019). However by reducing rotational recrystallization by a factor of 3 in fig. 5.10 I am able to predict well the eigenvalues seen in Stoll (2019). The motivation for this change is in table 3.2 I

found $\tilde{\lambda}$ to be the parameter most invariant with temperature and most dependent on strain-rate, with a power of ~ 0.1 . The initial value of $\tilde{\lambda}$ was estimated from laboratory experiments, at strain rates of around $10^{-6} - 10^{-5} \text{ s}^{-1}$. In contrast, even in the fast flowing region around EGRIP the maximum strain rate is only around 10^{-11} s^{-1} . Although the parameters were hypothesised to be strain-rate independent to leading order, fig. 3.2 in chapter 3 shows the largest eigenvalue increasing as strain-rate decreases.

The results in fig. 5.10 would suggest that rotational recrystallization, controlled by λ , should be strain-rate dependent rather than temperature dependent. To investigate this I show in fig. 5.11 regressions assuming (a) only strain-rate dependence and (b) only temperature dependence for $\tilde{\lambda}$, including the data point from EGRIP alongside the data from table 3.1. Assuming a power law dependence $\tilde{\lambda} \propto \dot{\gamma}^p$ gives a power of only $p = 0.082$, so this is a weak dependence, however still significant when considering the orders-of-magnitude difference in strain-rates between laboratory experiments and ice-sheets. The fit is much better for the strain-rate dependence ($R^2 = 0.724$) compared to assuming a temperature dependence only ($R^2 = 0.159$). The confidence interval of the regression in (a) is still quite wide for low strain-rates appropriate to ice sheets. Applying the methodology in this chapter to other ice core locations could provide further data points at low strain-rates on this graph. Based on this, it may be appropriate to update the SpecCAF parameterisation to include a strain-rate dependence for $\tilde{\lambda}$.

5.5.4 *The importance of basal slip for the flow of NEGIS*

My results show that as u_b decreases, the depth at which the fabric transitions from a girdle to a single-maxima decreases. This occurs as reducing u_b/u_s means more vertical shear, so the depth at which vertical shear dominates the x and y shear terms reduces. When vertical shear dominates, the deformation regime is simple shear and a single-maxima is produced at this temperature (-30°C). Figure 5.6 ($u_b = 0$) transitions to a single-maxima at a depth of around 500 m, fig. 5.7 ($u_b = 0.9u_s$) transitions to a single-maxima around 1600 m. Only figs. 5.5 and 5.10, with $u_b = u_s$, accurately predict the fabric pattern at EGRIP. Therefore, the fact that the EGRIP ice cores have a girdle fabric to a depth of 2100 m - and possibly lower as cores below this are not yet available - suggests that the values of u_b/u_s

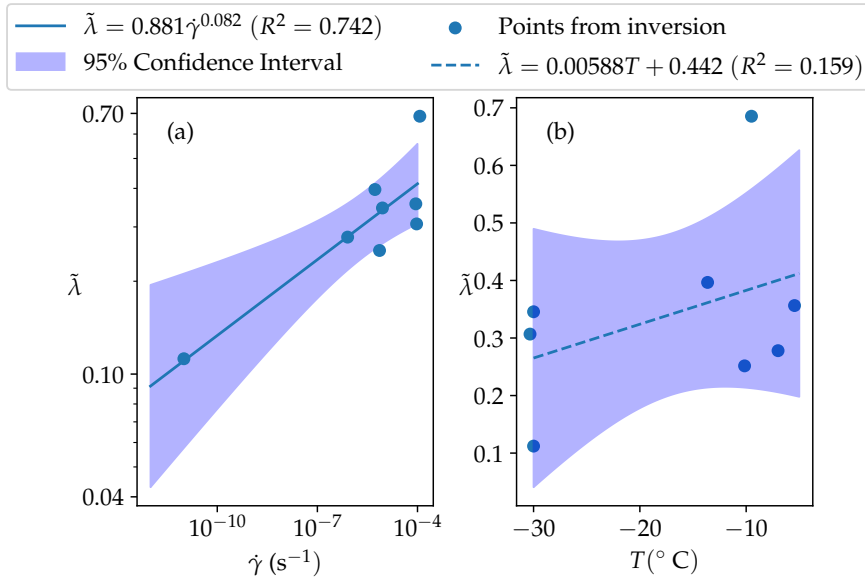


Figure 5.11: Plot showing a regression for $\tilde{\lambda} = \lambda/\dot{\gamma}$ for (a) strain-rate dependence only, and (b) temperature dependence only. The points used in the regression (from both chapters 3 and 5), 95% confidence interval and R^2 values are shown.

and consequently the amount of basal-sliding underneath EGRIP and possibly in the whole of NEGIS is extremely high. Another explanation is that the value of the power-law exponent, n , could be higher than 3. Recent work (Bons et al., 2018) has suggested $n = 4$ may be more valid in ice sheets. As can be seen from eq. (5.1) increasing n would concentrate the vertical shear closer to the base of the ice-sheet. With more ice core data close to the base (expected in 2022) this approach of combining ice core data with numerical modelling opens avenues for using fabric data to infer values for basal-slipperiness and for the parameter n .

5.5.5 Timescales for fabrics to adjust to new deformations

It is an open question how long fabric retain their ‘history’, i.e. how quickly fabrics adjust to changes in deformation and how far upstream deformation must be taken into account. Providing a robust measure of this is beyond the scope of this thesis, but the results presented above give insights into this. Figure 5.10 agrees well with the fabric pattern and strength at EGRIP. This figure very little variation of the fabric with depth below around 500 m. The streamline which finishes at this

depth starts 150 km upstream and takes a total time from the surface to EGRIP (from the streamline integration) of approximately 6000 yrs. As $u_b/u_s = 1$ for this simulation, although the fabrics have been deformed for different times, at the same point along the streamline they experience the same deformation. This suggests these fabrics are responding dynamically to changes in deformation, and the history beyond 6000 yrs, for this case, is unimportant. Lilien et al. (2021) finds that changes in deformation may affect the fabric for ~ 1000 to 10,000 yrs, in broad agreement with this result.

As fig. 5.10 suggests it takes fabrics ~ 150 km to respond fully to changes in deformation, it is unsurprising that fig. 5.9b shows a single-maxima at depth (characteristic of $u_b \ll u_s$) despite the local value of $u_b = u_s$ at EGRIP, shown in fig. 5.8. As can be seen in fig. 5.8, u_b/u_s has changed to 1 only over the last 30 km, so based on the results in fig. 5.5 we would not expect the fabric to adjust to this new deformation over such a short distance.

5.5.6 *Deformation mechanisms in ice stream flow*

As mentioned in section 2.1 there is currently an open question over whether the flow of ice streams can be explained entirely by dislocation creep (including basal-slip deformation, rotational recrystallization and migration recrystallization), which is encapsulated by the fabric model used here, or whether other processes are important, such as grain boundary sliding. Goldsby and Kohlstedt (2001) suggested that grain boundary sliding is the dominant deformation process in ice-sheets. This is unlikely to be true (Duval and Montagnat, 2002) however grain boundary sliding is still a candidate to contribute to ice deformation (e.g. Fan et al., 2020). Deformation by grain boundary sliding does not produce a fabric (Duval and Montagnat, 2002; Zhang et al., 1994).

The fact that the model can predict natural fabrics, taking only into account mechanisms caused by dislocation creep suggests that at least for EGRIP deformation ($\dot{\gamma} \sim 10^{-11} \text{s}^{-1}$) deformation is dominated by dislocation creep. Furthermore, if grain boundary sliding was contributing a small amount to deformation, we would expect a weaker fabric compared to laboratory experiments (which are indisputably in the dislocation creep regime). However we see the opposite result here: the fabrics at EGRIP are much stronger than predicted by the model using parameters derived from experiments fig. 5.5. It should be noted

however, that the model only predicts the distribution function of c -axes subject to deformation. Grain boundary sliding could still be present in the microstructure if it does not affect the deformation or the c -axis pattern.

5.6 CONCLUSIONS

Here I provide the first attempt to theoretically predict ice fabrics from a real-world ice stream. Cores taken from the [EGRIP](#) site lie in the fast flowing [NEGIS](#) and fabrics show a girdle or horizontal maxima pattern perpendicular to the flow direction. I model the upstream deformation conditions using satellite data and plan-view paths from Gerber et al. (2021) and Mougnot et al. (2019), as well as using the shallow ice approximation (allowing for sliding at the base of the ice sheet) to derive a leading order approximation for the velocity gradient through the ice sheet.

SpecCAF is able to predict the observed girdle/horizontal maxima aligned perpendicular to the flow direction which is seen at [EGRIP](#). These patterns were unexplained but the results show these fabrics can be produced through our current understanding of ice dynamics. The fact that the model was most accurate for full slip at the base ($u_b = u_s$) suggests that the level of basal sliding in [NEGIS](#) is very high. I also provide a timescale of 6000 yrs for fabrics to adjust to local deformation conditions, in agreement with Lilien et al. (2021).

By reducing rotational recrystallization I am also able to fully predict the pattern and eigenvalues seen at [EGRIP](#). This suggests that rotational recrystallization may be primarily strain-rate or stress dependent, as suggested by Faria et al. (2014). Future work could further constrain this relation. Furthermore, the fact that I can accurately predict fabrics at [EGRIP](#) using this model, suggests that dislocation creep - which underpins the mechanisms in the model - is the dominant deformation mechanism in this ice stream. Future work could further constrain this relation.

The work in this chapter could be extended by applying the procedure to other ice core locations, such as those taken at divides (e.g. Thorsteinsson et al., 1997). This would provide another end-member in the range of deformations. The modelling approach here can also be used to provide insights into the basal-conditions, and possibly the parameter n in the flow law.

ONGOING AND FUTURE WORK

6.1 ONGOING WORK

The work described in previous chapters represents a step forward for modelling ice fabrics, especially at large scales such as simulating ice sheets. The next step from this is to combine SpecCAF, which models the evolution of ice fabrics, with modelling of the viscous anisotropy of ice. As mentioned in previous chapters, the fabric of ice can cause viscous anisotropy due to the alignment of crystal grains. This has been shown to cause the flow rate to vary by a factor of 9 in different directions (Pimienta and Duval, 1987). Through the work in this thesis, we now have a constrained fabric model incorporating all the key processes, which gives good results when compared to both experiments and ice cores from ice sheets (chapters 3 and 5 respectively).

As part of ongoing work, and as future work leading on from this thesis, I am developing a coupled model to combine SpecCAF with representations for viscous anisotropy to simulate realistically the flow of ice sheets. Hruby et al. (2020) has recently shown that the fabric can cause ice streams to flow 15% faster (using an uncoupled model without fabric evolution). Viscous anisotropy coupled to fabric evolution has been applied to ice sheets before. Martín et al. (2009) simulated ice at a 2D divide, using the Static model described in eq. (2.14) and describing the fabric using the evolution equation for $\mathbf{A}^{(2)}$ described in eq. (2.27). The Elmer/ICE model (Gagliardini et al., 2013) is also capable of representing viscous anisotropy and fabric evolution in three dimensions, using a modified $\mathbf{A}^{(2)}$ described in eq. (2.28). However, the vast majority of ice-sheet models either do not include fabric evolution and viscous anisotropy, or attempt to include it by a constant enhancement factor (e.g. Graham et al., 2018) multiplying the viscosity, which is not dependent on the fabric and simply reduces the viscosity by the same factor in all directions.

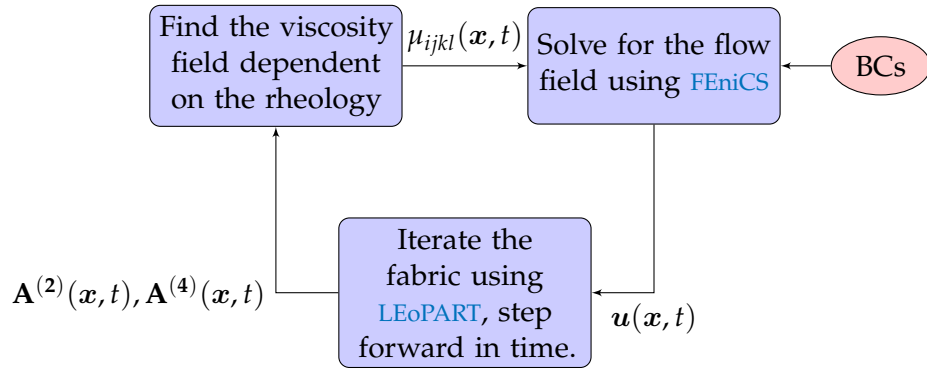


Figure 6.1: A schematic of the numerical procedure for the proposed coupled model for anisotropic viscous flow of ice deformed by dislocation creep. Starting at the top left, the anisotropic viscosity tensor is calculated in terms of the fabric, represented by $\mathbf{A}^{(2)}$ and $\mathbf{A}^{(4)}$ - see section 2.2.2. From this the flow field can be calculated, depending on the geometry and boundary conditions. Then the fabric at the next timestep can be found using SpecCAF

6.1.1 Numerical method

When incorporating the effect of anisotropy, the viscosity is usually described by a fourth-rank tensor μ_{ijkl} . I have described the different anisotropic viscosity formulations in section 2.2.2. Here I detail the steps I use to couple these to the fabric evolution model and solve for the flow field.

I use Finite Element Computational Software (FEniCS) (Martin Alnæs et al., 2015), combined with Lagrangian-Eulerian on Particles (LEoPART), a particle tracking add-on for FEniCS (Maljaars et al., 2021) to solve the coupled anisotropic viscous flow and fabric evolution equations. A schematic for the numerical procedure is shown in fig. 6.1. Once an initial condition for the fabric is defined (e.g. isotropic everywhere) the viscosity tensor can be defined, I then use this to solve for the velocity \mathbf{u} . The velocity is a diagnostic variable: it is set by the fabric field and the equation does not incorporate time dependence. With this new velocity field I use SpecCAF to find the ice fabric field at the next timestep.

6.1.1.1 Defining the viscosity tensor

The viscosity tensor μ_{ijkl} can be computed using one of the four formulations in section 2.2.2: the viscosity formulation arising from the Taylor bound in eq. (2.10); taking the inverse of the equation for the fluidity arising from the Static bound in eq. (2.14); the GOLF flow law from Gillet-Chaulet et al. (2005) in eq. (2.16); and finally the CAFFE flow law from Placidi et al. (2010) in eq. (2.17). To-date I have implemented all of the above with the exception of the GOLF flow law.

6.1.1.2 Solving for the velocity

Once the viscosity tensor is calculated the next step is to solve for the velocity field \mathbf{u} . As FEniCS is a finite element library we rewrite the Stokes equations (eq. (2.2)) in the variational form:

$$\int_{\Omega} S_{ij} \frac{\partial v_i}{\partial x_j} - p \frac{\partial v_i}{\partial x_i} + q \frac{\partial u_i}{\partial x_i} dx = \int_{\Omega} \rho g_i v_i, \quad (6.1)$$

where Ω is the solution domain and v and q are test functions to be chosen. This has the significant advantage compared to eq. (2.2) of not involving a derivative of \mathbf{S} . As we described in eq. (2.15), for non-linear viscous anisotropy the stress has the form:

$$S_{ij} = (2A)^{-1/n} \dot{\gamma}^{\frac{1-n}{n}} \mu_{ijkl} D_{kl},$$

where $\dot{\gamma}$ is the effective strain-rate as defined in eq. (4.2). Combining eq. (6.1) and the above equation I obtain:

$$\int_{\Omega} \frac{1}{2} (2A)^{-1/n} \dot{\gamma}^{\frac{1-n}{n}} \mu_{ijkl} \left(\frac{\partial u_k}{\partial x_l} + \frac{\partial u_l}{\partial x_k} \right) \frac{\partial v_i}{\partial x_j} - p \frac{\partial v_i}{\partial x_i} + q \frac{\partial u_i}{\partial x_i} dx = \int_{\Omega} \rho g_i v_i, \quad (6.2)$$

which, although complicated, can be inputted directly into FEniCS. This equation is solved with an iterative method due to the non-linearity ($\dot{\gamma}$ is a function of the velocity). This gives the velocity field, which is solely a function of the viscosity field $\mu_{ijkl}(\mathbf{x})$ and any boundary conditions.

6.1.1.3 Iteration of the fabric evolution

Once the velocity field is known at time t , the fabric evolution can be iterated to the next time step. To do this I use LEOPART, (Maljaars et al., 2021), which is an add on for FEniCS which allows for Lagrangian

particle tracking. I use this because the fabric evolution equation is hyperbolic in space:

$$\frac{\partial \rho^*}{\partial t} + \mathbf{u} \cdot \nabla(\rho^*) = \mathcal{F}^*(\rho^*, \mathbf{u}), \quad (6.3)$$

where \mathcal{F}^* denotes a short-hand for the orientationally dependent part of the fabric evolution equation, which is solved by SpecCAF. To solve this in an Eulerian frame typically requires the introduction of some level of artificial viscosity to suppress numerical instabilities (e.g. Dmitri Kuzmin et al., 2012) which is not representative of the true solution. Martín et al. (2009) used a semi-Lagrangian method (e.g. Durran, 1999) to solve for the fabric. Here LEOPART allows us to use a fully Lagrangian method. In essence, a number of particles are advected through the flow field with time, subject to the local velocity field. Each particle carries the fabric information, which is updated through SpecCAF, subject to the local velocity gradient at each timestep. LEOPART then provides methods to project the fabric information carried by the particles onto the finite-element space on which the velocity is solved for.

6.1.2 Preliminary Results

To show preliminary results for the coupled model, I present results for ice flowing through a constriction. This is a 2D simulation which is heavily idealised, but represents an ice shelf passing between a constriction, for example two islands. I show preliminary results for a simulation run at $T = -20^\circ\text{C}$ for SpecCAF, with the Taylor viscosity formulation (eq. (2.10)), and $n = 3$, and 6660 cells. The current implementation is non-dimensional and is run for 296 iterations to a non-dimensional time of 4.1. I start with an isotropic fabric everywhere and show the initial velocity field in fig. 6.2, along with annotations for the boundary conditions. I run half the domain shown, with a symmetry condition on the dashed line. The flow is driven by a pressure inlet on the left. The obstruction is defined as a no-slip wall and the other walls at the very bottom and top are free-slip walls. There is an outlet on the right-hand side. The colour scale is chosen to match the later fig. 6.3. Streamlines are also shown.

Figure 6.3 shows the same figure but at the end of the simulation, $t = 4.1$. As can be seen from the matching colour scale, the speed of flow through the constriction is much greater. The maximum speed

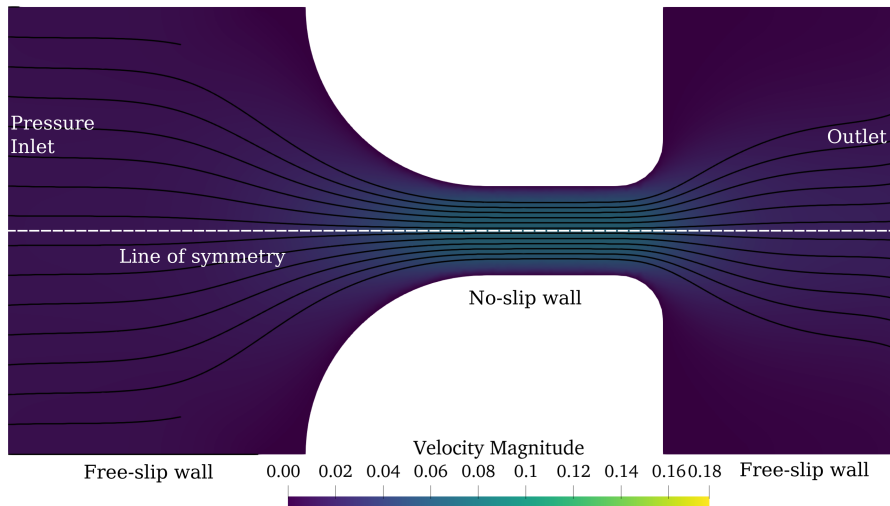


Figure 6.2: Velocity magnitude at $t = 0$, with an isotropic fabric everywhere. Annotations show the boundary conditions: a pressure inlet on the length, a line of symmetry in the centre (so the top half of the simulation is not computed, but a reflection of the bottom), an outlet on the right, no-slip walls to describe the obstruction and free-slip walls elsewhere. The colour scale is chosen to match fig. 6.3

is 2.7 times greater. This can be explained by the fabric. Figures 6.4 and 6.5 show $A_{xx}^{(2)}$ and $A_{yy}^{(2)}$, the components of the second-order orientation tensor in the flow direction and vertically upwards at the final time. As can be seen from figs. 6.4 and 6.5 the c -axes have aligned perpendicular to the flow, so the basal planes are parallel to the flow direction in the constriction and therefore there is less resistance in the constriction, consequently an increased flow rate.

6.2 FUTURE WORK

In this section we will discuss avenues for future work from this thesis, based on both the ongoing work in section 6.1 as well as extending the analysis done in previous chapters.

The first avenue of future work is to continue developing the coupled model. As can be seen from figs. 6.4 and 6.5, further work is needed to validate the model and dimensionalise it so it can be applied to real world conditions, as well as improving its robustness. Martín et al. (2009) ran a simulation for a 2D ice divide with the Static viscosity formulation and the fabric described by $\mathbf{A}^{(2)}$. I believe extending this

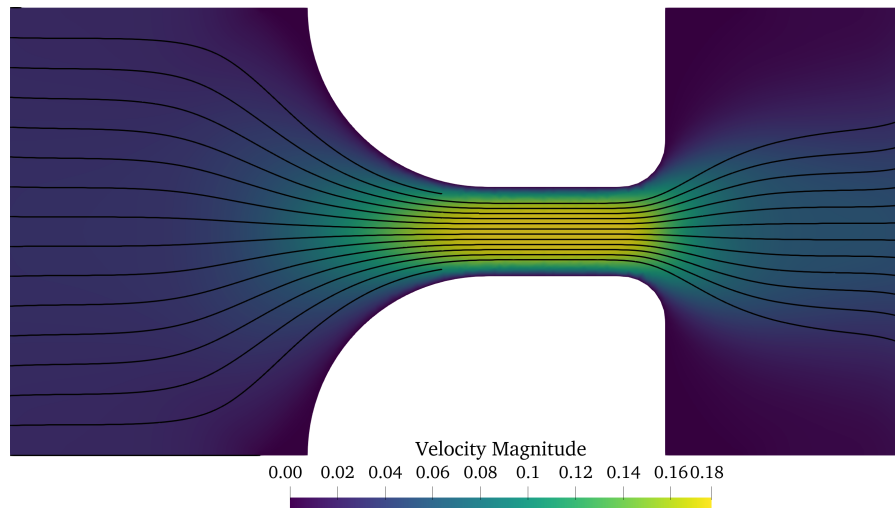


Figure 6.3: Plot of velocity magnitude like fig. 6.2 but at the end of the simulation ($t = 4.1$).

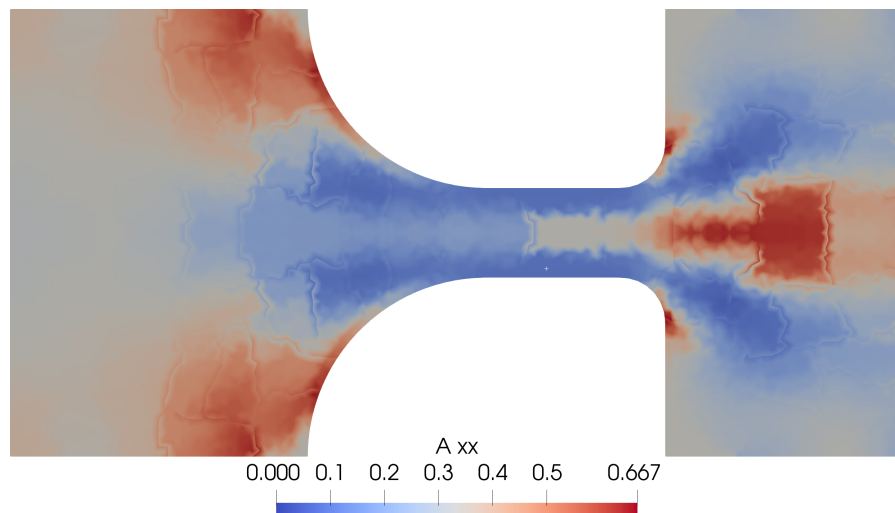


Figure 6.4: Plot of $A_{xx}^{(2)}$, the component of the second-order orientation tensor aligned with the flow direction, at the end of the simulation. At $t = 0$ $A_{xx}^{(2)}$ was $1/3$ (grey) everywhere.

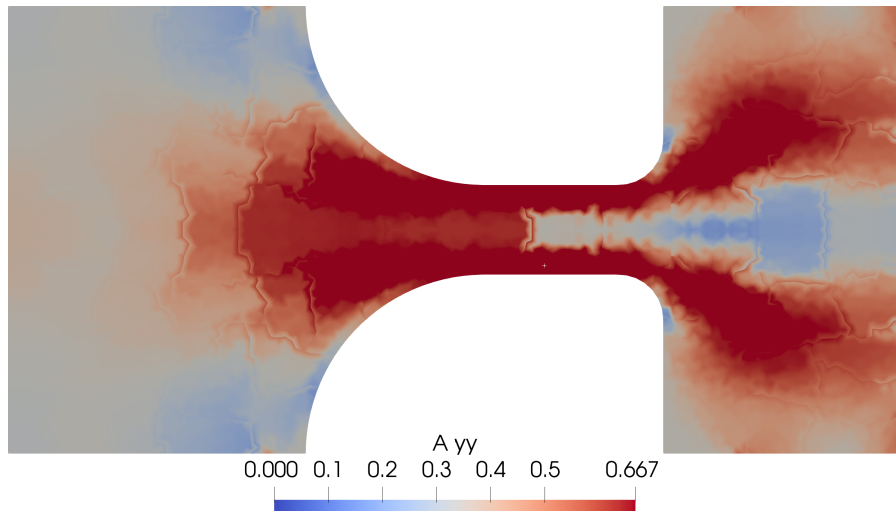


Figure 6.5: Plot of $A_{yy}^{(2)}$ (y is vertically upwards), at the end of the simulation. At $t = 0$ $A_{yy}^{(2)}$ was $1/3$ (grey) everywhere.

result, with the more accurate SpecCAF fabric evolution model and a range of viscosity formulations, offers a first step for both reliably validating the numerical model, and producing publishable work for a case valid to ice sheets. This involves incorporating free-surface evolution which I am in the process of doing.

Once the model is validated, many cases can be run. As can be seen in fig. 6.3, it is possible to use simple cases to constrain enhancement factors used in large-scale ice-sheet models. I can also use the model to simulate other areas where anisotropy may be important, such as ice streams and ice margins.

The modern numerical framework of the model, incorporating both Lagrangian and Eulerian frameworks, allows it to be easily extended to incorporate other key properties which are ‘carried with’ the flow field and affect the viscosity, such as melt-water content and damage. This allows us to take a first step towards a model which incorporates all key processes together for the first time.

Alongside the development of this coupled model, there are also numerous other avenues for future work. One possibility is to extend the analysis in chapter 5 performed at EGRIP to general locations in Greenland and Antarctica. This would enable comparisons with a wide range of ice core locations in different deformation conditions (Thorsteinsson et al., 1997), and also to fabrics inferred from radar and seismics (Booth et al., 2020; Lutz et al., 2020). This would allow investigation and constraint of the strain-rate dependence of the parameters in SpecCAF, by adding more data points to fig. 5.11. The methodology

could also allow the inferring of other ice-sheet properties, such as the level of sliding at the base of the ice sheet, across a wide range of locations.

There is also potential to incorporate SpecCAF into large-scale ice sheet models, such as Elmer/ICE (Gagliardini et al., 2013). Furthermore, the SpecCAF framework could be extended to incorporate other polycrystalline materials, such as olivine fabrics which are key for predicting the flow of the Earth's mantle (Conrad et al., 2007). This will involve incorporating multiple slip systems and crystallographic axes into the model, which could be done by solving multiple coupled equations for different orientation fields.

DISCUSSION AND CONCLUSIONS

7.1 GENERAL DISCUSSION

In chapters 3 to 5 I have developed the first fully calibrated continuum fabric evolution model SpecCAF, which is able to predict fabrics with only temperature and velocity gradient as inputs. I have used SpecCAF to explore general two-dimensional deformations as well as applying it to fabrics from ice cores drilled in an ice stream. The result of this work is improved modelling of ice fabrics, as well as improved understanding of observed fabrics and consequently of other properties in ice sheets. I now discuss the work done in the previous chapters in light of the research questions in section 1.1:

Q1: How can we improve our modelling of ice fabrics, including all key processes while retaining computational efficiency?

For ice fabric evolution, describing the distribution of c -axes, the literature (e.g. Faria et al., 2014) identifies three key processes in deforming ice: basal-slip deformation, migration recrystallization and rotational recrystallization. The approach for fabric evolution used in large-scale ice-sheet models, evolving the second-order orientation tensor (e.g. Gagliardini et al., 2013), is not capable of representing migration recrystallization accurately. As can be seen in fig. 2.3 this is key for producing detailed fabric patterns, which have been observed in experiments (Qi et al., 2019) and ice cores (e.g. Hudleston, 1977).

The SpecCAF model I present in chapter 3 and expand upon in chapters 4 and 5 represents a big step forward for modelling the fabrics of ice. The model allows fabrics to be predicted with only temperature and velocity gradient as inputs, including all the key processes. In comparison to models which represent the microstructure directly, such as Kennedy and Pettit (2015) and Llorens et al. (2016), SpecCAF can more reliably reproduce detailed features such as secondary clusters; for example Llorens et al. (2016) struggles to reproduce a secondary cluster. SpecCAF is also much more computationally efficient, which enables us to perform sweeps through deformation and

temperature space such as in chapter 4, enabling the production of regime diagrams (figs. 4.9 and 4.10) to aid with the interpretation of ice cores.

The computational efficiency of SpecCAF not only enables all the main work in this thesis, such as parameter sweeps and applying the model to ice cores, but also is key to incorporating fabric evolution into large-scale models. This is why to date only evolution for the second-order orientation tensor has so far been included in these models. SpecCAF has excellent computational efficiency for two reasons. Firstly, as laid out by the theory of Faria (2001) and discussed in section 2.2.4.2 the model does not seek to include grain-to-grain representations, but instead models their bulk affect on the distribution function. This is in contrast to Kennedy and Pettit (2015), Llorens et al. (2016), and Piazzolo et al. (2015) which do aim to include grains. This advantage enables SpecCAF to be applied to large-scale problems without having to represent a huge range of length scales, from microstructure to ice sheets. This is analogous to parameterisations for turbulence used extensively in computational fluid dynamics, which mean turbulence does not have to be resolved down to millimetre scale throughout the model. And like with turbulence modelling, there is still a need for these models to improve our parameterisation of the fundamental processes in continuum models like SpecCAF.

The second reason for SpecCAF's computational efficiency is the spectral method, detailed in section 3.3. The fabric evolution equation from Placidi et al. (2010) avoids including grain-to-grain interactions. However it accomplishes this by adding two extra dimensions to the problems: the two spherical angles θ, φ . The advantage of the algorithm described by Montgomery-Smith et al. (2010) is that it reduces the partial differential equation over these two dimensions to a set of ordinary differential equations, while still recovering the full solution as $l \rightarrow \infty$ (eq. (A.1)). Reducing the partial differential equation to a set of ordinary differential equations can also be accomplished by taking moments of eq. (3.3), deriving a similar equation to eq. (2.27) for orientation tensor evolution. The disadvantage of this is that to include migration recrystallization requires a closure approximation for both the $n + 2$ and $n + 4$ th rank tensor. Furthermore, the spectral method in section 3.3 automatically takes advantage of all symmetries so that calculating the solution to high precision is possible. To highlight this, consider that in chapters 3 and 4 I truncate SpecCAF at $L = 12$. I could also take moments of eq. (2.30) to generate an equation for the

12th-order orientation tensor which would give the same accuracy. However this would entail solving an equation for a tensor of rank 12, and finding an accurate approximation for $\mathbf{A}^{(14)}$ and $\mathbf{A}^{(16)}$ in terms of the other tensors.

Q2: How do the processes affecting fabric evolution vary with temperature and strain-rate?

Although, as discussed in section 2.2.4.2, SpecCAF only represents grain-to-grain interactions through parameterising their effect on the bulk c -axis distribution function, therefore they cannot be said to directly correlate to recrystallization processes occurring at the microstructure. The effect of other processes not included in the model, for example, non-basal slip systems, are also parameterised by the values of ι, λ, β . Furthermore, comparing ratios between parameters, such as β/λ cannot be used to state anything about how much migration recrystallization there is relative to rotational recrystallization in the microstructure. Nevertheless, the parameters can provide a leading order estimate of how microstructural processes, and especially their effect on the fabric, vary with temperature and strain-rate.

From fig. 4.5 and table 3.2 I find that the parameterisation of migration recrystallization is primarily and strongly dependent on temperature, increasing by a factor of 6.4 between $T = -30^\circ\text{C}$ and $T = -5^\circ\text{C}$. This broadly agrees with theory (Faria et al., 2014). I also predict a linear dependence with temperature. This linear fit gives good predictions at intermediate values such as $T \approx -20^\circ\text{C}$ where there were limited points for the inversion. However we would intuitively expect the temperate dependence to follow an Arrhenius profile as the dislocation creep which drives these processes has this temperature dependence. Further data points from laboratory experiments would be helpful here, though it may be the case that although migration recrystallization on the microstructural scale follows an Arrhenius temperature dependence, how it affects the orientation distribution function could vary linearly with temperature.

The parameter ι , controlling the effect of basal-slip deformation on the fabric, primarily varies with temperature, increasing by 55% from $T = -30^\circ\text{C}$ to $T = -5^\circ\text{C}$, and is above 1 throughout. As discussed in section 3.5, The temperature dependence of ι could be explained by the increased activity of migration recrystallization producing grains easily orientated for slip along the basal plane. $\iota > 1$ implies the

contribution of basal-slip deformation to fabric development greater than that predicted by the Taylor hypothesis, which is expected as the fabric evolution equations derived from the Taylor hypothesis under-predict fabric evolution (Montagnat et al., 2014b).

Considering both the results in chapter 3 and chapter 5 we can better estimate the strain-rate dependence of ι . The fact that there is no need to change this parameter to give a good fit to results in fig. 5.10, despite the 5 orders of magnitude change in strain-rate gives confidence in my assumption in chapter 3 that this parameter is invariant with strain-rate. The result, that the contribution of basal-slip deformation to the fabric is approximately invariant with strain-rate may also suggest that the relative activity of different slip systems is also invariant with strain-rate. To compare to other work, micro-scale modelling by Castelnau et al. (2008) predicts that the activity of slip-systems does not vary, but they only explore a single order of magnitude change in strain-rate. Unfortunately, as the ice sheet around EGRIP is at around -30°C , for which the effect of migration recrystallization on the fabric is minimal, I cannot yet investigate the strain-rate dependence of the effect of migration recrystallization on the fabric. Future work to answer this would involve reproducing fabrics taken from a warmer region of the ice sheet.

Figure 5.11 predicts that any change in the effect of rotational recrystallisation on the fabric, represented by $\tilde{\lambda}$, can be much better explained by a strain-rate dependence than a temperature dependence. Compared to the other parameters, $\tilde{\lambda}$ is mostly independent of temperature, increasing only by 20% between $T = -30^{\circ}\text{C}$ and $T = -5^{\circ}\text{C}$. The predicted power of 0.082 in fig. 5.11 is in reasonably good agreement to that derived from laboratory experiments in table 3.2 (0.124). In contrast the estimated strain-rate dependence of the other parameters in table 3.2 is much closer to 0. Therefore I suggest that future implementations of SpecCAF include the strain-rate dependence found in fig. 5.11 rather than a temperature dependence. The results suggest that rotational recrystallization on the microstructural level has more of an effect on the fabric as strain-rate increases. However, it is still hard to project down onto the microstructural scale which is not resolved in SpecCAF. This may mean that the relative frequency of small grains - a microstructural measure of rotational recrystallization - directly correlates with this increase. However another explanation could be that the grains undergoing rotational recrystallization increase in relative size as strain-rate increases, so have a larger impact

on the fabric pattern. Work with micro-scale models such as Llorens et al. (2016) is required to properly investigate this.

Q3: Can we explain fabric patterns produced in completely general deformations, both in nature and in laboratory experiments, by taking exclusively deformation by dislocation creep into account?

The work in this thesis represents a step forward towards understanding fabric patterns in general deformation regimes and across the temperature spectrum found in ice sheets. Fabric patterns such as a secondary cluster in simple shear (Qi et al., 2019) or a cone-shape fabric in compression (e.g. Fan et al., 2020) have been well studied. However ice cores continually exhibit complex patterns, such as a girdle fabric in the deepest part of GRIP (Thorsteinsson et al., 1997) or the double-maxima perpendicular to the flow direction at EGRIP (Stoll, 2019).

In section 3.4.1 I am able to explain the common fabric patterns, as shown in Paterson (1999). Furthermore, the ability of the model to turn off or on different mechanisms affecting the fabric allow us to interpret which recrystallization or deformation processes are acting to produce each fabric. In addition, I am able to extend this understanding of fabrics produced by canonical deformation regimes to include for the first time a weak girdle produced by highly-rotational deformation regimes (fig. 5.4) and also generalise it to the continuous space of vorticity number and temperature in chapter 4.

Recent data from ice streams, either from ice cores (Stoll, 2019) or seismics (Booth et al., 2020; Lutz et al., 2020) have shown fabric patterns, such as girdles aligned with the flow direction (Stoll, 2019) or horizontal partial girdles (Lutz et al., 2020) which arise from complex, three-dimensional deformations. These lie outside even the two-dimensional spectrum I consider in chapter 4. These results show that explaining fabric patterns from combinations of deformation regimes like simple or pure shear becomes tricky in three dimensions, where the fabric may be caused by competing combinations of a range of deformation modes, acting in all three dimensions. However, in chapter 5 I am able to use leading order estimates of the deformation from satellite data to reproduce the fabric patterns seen at EGRIP. This shows that, even if it may be hard to explain these fabrics through a combination of deformation modes, they are still accounted for by our current theories for fabric evolution, encapsulated by SpecCAF.

The fact that the model can reproduce fabrics from both experiments and from ice streams suggests that the theory underpinning the model - based on dislocation creep - is valid for these conditions and can be solely used to explain observed fabrics without necessitating extra processes to account for grain boundary sliding. Furthermore, the fact that a stronger fabric is produced at lower strain-rates is contrary to the idea that grain boundary sliding, which if active would produce a weaker fabric (e.g Duval and Montagnat, 2002), contributes to deformation at lower strain-rates. However, as the model only represents the bulk distribution of c -axes, this does not suggest processes such as grain boundary sliding or diffusional creep cannot occur in the microstructure as long as their effect on the fabric and macroscopic deformation is minimal. This investigation could be extended by testing if SpecCAF can reproduce fabrics produced in very low strain-rate regions, such as ice divides.

Q4: How can the developed fabric evolution model be used to improve our understanding of the dynamics of ice sheets?

With confidence in a fabric evolution model, and an understanding of the fabric produced under different conditions we can better use fabrics to infer other physical conditions and processes in the ice sheet. This has commonly been done when ice cores have been drilled, but can also be done using radar and seismics (Matsuoka et al., 2003). This approach is promising as drilling ice cores is very expensive and laborious. Radar and seismics also enables data to be gathered in areas it may be too dangerous to drill in (e.g. Jordan et al., 2020). Jordan et al. (2020) and Thorsteinsson et al. (1997) and others use fabrics to *qualitatively* infer deformation in the ice sheet by comparing the fabric patterns observed elsewhere and in experiments (which are mostly in compression and simple shear). The regime diagrams I present for fabric patterns (figs. 4.9 and 4.10) allow deformations to be inferred in a more precise way, especially if other conditions such as temperature can be estimated. This can allow us to move away from thinking in terms of pure and simple shear towards the continuous spectrum of deformation which occurs in ice sheets.

Furthermore, I also provide a *quantitative* method to infer ice sheet properties from fabric data in chapter 5. By combining the fabric evolution model presented earlier in this thesis with satellite data, which is available for the whole of Antarctica (Mouginot et al., 2019) and

Greenland (Joughin et al., 2018) we can predict fabrics at locations and compare them to ice core or seismic data. The methods used in chapter 5 can be easily generalised to other locations. Using this method, we can use the fabric pattern to infer conditions and processes deep into the ice sheet much more accurately. If the predicted fabric does not agree, this implies the deformation in the ice sheet at this location diverges from the leading order approximation, or the underlying theory for fabric evolution is breaking down: both are interesting results which would suggest further investigation. If the predicted fabric does agree, this method can then be used to infer other properties in the ice sheet, such as the level of slip at the base (this can be inferred without requiring fabrics close to the base), the level of strain heterogeneity and even the value of the flow law parameter n . This method could be combined with more readily available radar data to use ice fabrics to infer conditions in the ice sheet over a much wider area. The work in this thesis thus represents a step forward for using fabrics to infer properties in ice sheets.

Q5: What is needed from a fabric evolution model to simulate viscous anisotropy and have we reached this stage?

Fabric evolution models which represent the microstructure (e.g Llorens et al., 2016) are not capable of being included in ice sheet models because it is not possible to simulate the range of length scales (10^{-4} to 10^6 m) with current computers. The current state of the art for incorporating anisotropy into ice-sheet models is Elmer/Ice. The current fabric evolution model used there is described in eq. (2.28). As discussed in section 2.2.4.1 this is computationally very efficient but incapable of representing detailed fabric patterns and migration recrystallization.

There is still considerable uncertainty over the correct viscosity formulation (described in section 2.2.2) and the parameters to use in the formulation. As shown in section 2.2.2 there are currently 4 candidate viscosity formulations. Furthermore, it is not possible to measure the terms in the viscosity tensor from laboratory experiments: these experiments are only capable of measuring 1 component in the fourth-rank tensor. One possible avenue to constrain the anisotropic viscosity tensor is to use a coupled model to compare the predicted ice flow to real-world scenarios. However in order to do this we must have confidence that the fabric evolution is accurate. Both $\mathbf{A}^{(2)}$ and $\mathbf{A}^{(4)}$

appear in eqs. (2.10), (2.14) and (2.18), so having reliable predictions for these is key.

I have shown that SpecCAF is able to accurately reproduce fabrics, both from experiments in chapter 3 and, perhaps more importantly, from ice cores taken in highly dynamic regions in the Greenland ice sheet in chapter 5. The methodology in chapter 5 can be applied to other locations to further improve the reliability of our fabric evolution models. The model is also able to accommodate changing temperature and strain-rate, which will naturally occur in simulations of an ice sheet. I have taken a first step towards coupling SpecCAF with anisotropic viscosity formulations in section 6.1. The increased confidence we have in fabric predictions gives a first step towards constraining the components of the viscosity tensor and hence reliably predicting the flow of anisotropic viscous ice.

7.2 CONCLUSIONS

The model I develop in this thesis, SpecCAF, is the first complete and fully constrained continuum model for fabric evolution. I do this by solving the fabric evolution equation from Placidi et al. (2010) using a spectral method and constraining the model against experimental results. The model can give predictions as a function of temperature and velocity gradient.

SpecCAF is capable of reproducing all the detailed features seen in observed fabrics, such as secondary clusters and cone angles. The model can also reproduce the strength of fabric as well. This represents a step forward from even microstructural models such as Llorens et al. (2016). In addition, SpecCAF is highly computationally efficient and can be incorporated into large-scale ice-sheet models.

The results from chapter 3 indicate that at high temperatures migration recrystallization has a leading order effect on fabric development, and must be incorporated to accurately predict ice fabrics. I also find that the effect of basal-slip deformation on the fabric is also primarily dependent on temperature, and invariant with strain-rate to leading order. The effect of rotational recrystallization on the fabric is found in chapter 5 to be primarily dependent on strain-rate, with the effect of rotational recrystallization on the fabric increasing as strain-rate increases.

I am able to use SpecCAF to explore fabrics produced across the space of two-dimensional deformations and temperature in chapter 4.

The regime diagram presented is a first for ice fabrics and allows for the systematic interpretation of the deformation regime and temperature conditions a fabric has undergone. Furthermore, I predict for the first time a weak girdle fabric is produced for highly-rotational deformations.

I am also able to use the model to reproduce fabrics from ice cores taken at the highly dynamic [EGRIP](#) region. This is accomplished by combining SpecCAF with satellite data to estimate the upstream velocity gradient. I am able to accurately reproduce the fabrics at [EGRIP](#) by assuming that rotational recrystallization is strain-rate dependent. This work shows our current models of fabric evolution can describe the novel fabrics seen from ice streams.

The fact that the model - based on processes driven by dislocation creep - can reproduce fabrics for both experiments and ice sheets suggests that the production of fabrics is dominated by this mechanism, and that other mechanisms such as grain boundary sliding do not contribute significantly to the fabric itself, even though they may occur in the microstructure.

Using the work in chapters [4](#) and [5](#) I am able to improve our ability to interpret ice cores. Both the regime diagrams shown in chapter [4](#) and the methodology in chapter [5](#) allows us to more accurately interpret the deformation ice fabrics have undergone. Furthermore, the methodology in chapter [5](#) can allow us to infer other properties deep into the ice sheet from fabrics, such as the level of sliding at the base of the ice sheet.

The SpecCAF model is now ready to be incorporated into a coupled model, alongside viscous anisotropy. I present a first step towards this in section [6.1](#). Work is ongoing to couple SpecCAF to representations for the anisotropic viscosity tensor, with a view towards simulating the flow of ice in some simplified conditions such as a 2D divide. With the constrained fabric model presented in this thesis, we will be able to take steps towards constraining the anisotropic viscosity tensor.

Alongside the development of a coupled model, future work could extend the analysis done in chapter [5](#) to any region in Antarctica and Greenland, so it can be compared to other ice core locations (e.g. Thorsteinsson et al., [1997](#)) or fabrics inferred from radar or seismics (Lutz et al., [2020](#)). Furthermore, there is the potential to extend SpecCAF to model other polycrystalline materials, such as olivine in the mantle, and to incorporate it into large-scale ice-sheet models.

SPHERICAL HARMONICS

In this appendix I give an overview of the spherical harmonics and their use for solving partial differential equations over the sphere. This is for use in defining the spectral method used in section 3.3.

For any function which exists over the surface of a sphere, such as the distribution function of c -axis orientations, a natural way to represent it is through the spherical harmonics. In this appendix I describe the spherical harmonics and identities associated with them. Laplace's spherical harmonics are solutions to Laplace's equation ($\nabla^2 f = 0$) over the surface of a sphere. For spherical coordinates with a polar angle θ the solution can be described as:

$$Y_l^m(\theta, \varphi) = N \exp^{im\varphi} P_l^m(\cos \theta), \quad (\text{A.1})$$

where P_l^m is an associated Legendre polynomial, a solution of the general Legendre equation. The above solution is valid for l is an integer ≥ 0 and m is an integer $-l \geq m \geq l$, and N is some normalisation coefficient, which varies depending on the conventions of particular scientific disciplines. In this thesis I use:

$$N = \sqrt{\frac{(2l+1)(l-m)!}{4\pi(l+m)!}}. \quad (\text{A.2})$$

The orthogonality of the spherical harmonics means:

$$\int_{S^2} Y_l^m Y_{l'}^{m'} d\mathbf{n} = \begin{cases} 1 & \text{if } m = m' \text{ and } l = l', \\ 0 & \text{otherwise.} \end{cases} \quad (\text{A.3})$$

Furthermore, the complex conjugate \bar{Y}_l^m obeys the following relation:

$$\bar{Y}_l^m = (-1)^m Y_l^{-m}.$$

Due to their orthogonality, the spherical harmonics form an orthonormal basis, so any function over the surface of a sphere can be written in terms of them:

$$f^*(\theta, \varphi) = \sum_{l=0}^{\infty} \sum_{m=-l}^l \hat{f}_l^m Y_l^m(\theta, \varphi), \quad (\text{A.4})$$

Thus the function can be described by the terms \hat{f}_l^m . These can be obtained by multiplying eq. (A.4) by the complex conjugate \bar{Y}_l^m , integrating over the surface of the sphere S^2 , and using the orthogonality relation in eq. (A.3):

$$\hat{f}_l^m = \int_{S^2} f^*(\theta, \varphi) \bar{Y}_l^m(\theta, \varphi) d\mathbf{n}. \quad (\text{A.5})$$

A.1 USING THE SPHERICAL HARMONICS TO SOLVE PARTIAL DIFFERENTIAL EQUATIONS

The spherical harmonics have advantages for solving partial differential equations on the surface of a sphere. For example, due to the definition of the spherical harmonics as solutions to Laplace's equation on the surface of a sphere, any diffusion term has a linear effect on the spherical harmonics:

$$\nabla^{*2} Y_l^m = -l(l+1) Y_l^m, \quad (\text{A.6})$$

where ∇^* is the gradient operator restricted to the surface of a sphere as defined in eq. (2.31). The above equation transforms a differential operator to a linear operation on a spherical harmonic term, which in this case relates only to the term with the same m and l .

Montgomery-Smith et al. (2010) provide a systematic algorithm for converting a partial differential equation over the surface of a sphere to operations on other terms in the spherical harmonic expansion. In this section I reproduce the mathematical identities used in Montgomery-Smith et al. (2010) to derive this algorithm, as they are used in section 3.3.

Rodrigues' Formula for Legendre polynomials can be used to find the effect of multiplying by n_z , the z component of the unit orientation vector \mathbf{n} , on a spherical harmonic:

$$n_z Y_l^m = \sqrt{\frac{(l+m)(l-m)}{(2l-1)(2l+1)}} Y_{l-1}^m + \sqrt{\frac{(l+m+1)(l-m+1)}{(2l+1)(2l+3)}} Y_{l+1}^m. \quad (\text{A.7})$$

Like with eq. (A.6) I have expressed multiplying by n_z as a sum of linear operations on other spherical harmonic terms. To extend this to account for multiplying by n_x, n_y , as well as differentiation $\frac{\partial}{\partial n_x}, \frac{\partial}{\partial n_y}, \frac{\partial}{\partial n_z}$ I first introduce the angular momentum operator:

$$\mathbf{L} = -i\mathbf{n} \times \nabla^*, \quad (\text{A.8})$$

which split into components gives:

$$\begin{aligned} L_x &= -i\left(n_y \frac{\partial}{\partial n_z} - n_z \frac{\partial}{\partial n_y}\right) \\ L_y &= -i\left(n_z \frac{\partial}{\partial n_x} - n_x \frac{\partial}{\partial n_z}\right) \\ L_z &= -i\left(n_x \frac{\partial}{\partial n_y} - n_y \frac{\partial}{\partial n_x}\right). \end{aligned} \quad (\text{A.9})$$

We note that the effect of the z component of the angular momentum operator on the spherical harmonics is

$$L_z(Y_l^m) = mY_l^m, \quad (\text{A.10})$$

From eq. (A.9) the ladder operators can be defined as:

$$\begin{aligned} L_+ &= L_x + iL_y \\ L_- &= L_x - iL_y. \end{aligned} \quad (\text{A.11})$$

These are called ladder operators because of how they affect the spherical harmonics:

$$\begin{aligned} L_+(Y_l^m) &= \sqrt{(l-m)(l+m+1)}Y_l^{m+1} \\ L_-(Y_l^m) &= \sqrt{(l+m)(l-m+1)}Y_l^{m-1}. \end{aligned} \quad (\text{A.12})$$

With the above, the effect of multiplying by n_x and n_y can be found from the identities:

$$n_x Y_l^m = in_z L_y(Y_l^m) - iL_y(n_z Y_l^m), \quad n_y Y_l^m = -in_z L_x(Y_l^m) + iL_x(n_z Y_l^m). \quad (\text{A.13})$$

Similarly, the components of ∇^* acting on the spherical harmonics can be expressed as:

$$\begin{aligned}\nabla_x^*(Y_l^m) &= n_z i L_y(Y_l^m) - n_y i L_z(Y_l^m) \\ \nabla_y^*(Y_l^m) &= n_x i L_z(Y_l^m) - n_z i L_x(Y_l^m) \\ \nabla_z^*(Y_l^m) &= n_y i L_x(Y_l^m) - n_x i L_y(Y_l^m).\end{aligned}\tag{A.14}$$

The above equations, which I repeat here from Montgomery-Smith et al. (2010) and which are also used in other fields such as quantum mechanics, provide a recipe for converting terms in a partial differential equation over the surface of a sphere into linear operations expressing the change in one term of the spherical harmonic expansion in terms of neighbouring terms.

A.1.1 Relationship between spherical harmonics and orientation tensors

Montgomery-Smith et al. (2010) also provide a formula to calculate any order orientation tensor from the spherical harmonics:

$$\mathbf{A}^{(n)} = \sqrt{4\pi} \sum_{l=0}^n \sum_{m=-l}^l \mathcal{C}_{l,m} \hat{f}_l^m,\tag{A.15}$$

where $\mathbf{A}^{(n)}$ is the n -th order orientation tensor, \hat{f}_l^m are the terms in the spherical harmonic expansion in eq. (A.4), and the terms in $\mathcal{C}_{l,m}$ can be determined using the equations in appendix A.1. From eq. (A.15) it can be seen that the n -th order orientation tensor contains terms in the spherical harmonic expansion only up to $l = n$. Therefore describing fabric evolution by $\mathbf{A}^{(2)}$ is equivalent to retaining terms in a spherical harmonic expansion only up to order 2. This explains why eq. (2.27), describing the evolution of $\mathbf{A}^{(2)}$, cannot reproduce more detailed features in the fabric.

NUMERICS AND CONSTRAINING OF SPECCAF

B.1 NUMBER OF HARMONICS

This section illustrates how by varying L in eq. (3.3), the computational cost and accuracy vary (fig. B.1). Both the error, defined as:

$$\text{error} = \frac{|\lambda_i^L - \lambda_i^{L=50}|}{\lambda_i^{L=50}}, \quad (\text{B.1})$$

where λ_i^L is the i th largest eigenvalue of $\mathbf{A}^{(2)}$ with L spherical harmonics, and pole figures are shown, all at $\gamma = 1$. Setting $L = 2$ gives similar accuracy to solving the evolution equation for $\mathbf{A}^{(2)}$. As can be seen in the figure, above $L = 6$ there is little difference in the pole figures.

B.2 EXPERIMENTAL DATA USED IN COMPARISON

This section gives table B.1, which shows the key data for each experiment used for comparison in fig. 3.4.

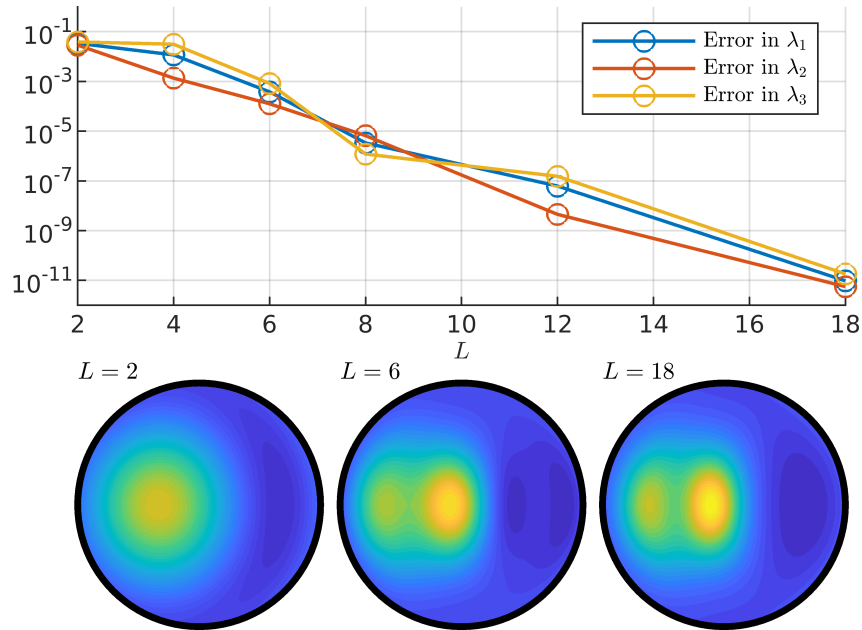


Figure B.1: The error in the eigenvalues of $\mathbf{A}^{(2)}$ and corresponding pole figures for different values of the number of spectral modes L , illustrating the higher resolution arising for large L . The illustrative parameters $\tilde{\lambda} = 0.05, \iota = 1, \tilde{\beta} = 1$ were chosen here. Both the error and the pole figures are shown at an arbitrary strain of $\gamma = 1$. The error is calculated relative to a highly numerically resolved solution with $L = 50$. The plot shows the exponential convergence of the spectral method.

Experiment	Paper	Name	Flow	$T/^\circ\text{C}$	$\dot{\gamma}/\text{s}^{-1}$	γ
1		PIL143		-30.6	1.46×10^{-4}	0.65
2	Qi et al. (2019)	PIL135		-30.5	1.25×10^{-4}	2.6
3		PIL145		-20.1	9.49×10^{-5}	1.1
4		PIL144	Simple shear	-20.4	1.19×10^{-4}	2.2
5		TGI071		-7	1.80×10^{-6}	0.71
6	Journaux et al. (2019)	TGI196		-7	2.10×10^{-6}	1.96
7	Qi et al. (2019)	PIL82		-5.4	7.98×10^{-5}	0.69
8		PIL94		-5.2	1.37×10^{-4}	1.5
9	Craw et al. (2018)	PIL132		-30	2.80×10^{-5}	0.2
10		PIL141		-30	7.20×10^{-6}	0.23
11		13_22		-20.5	2.50×10^{-6}	0.1
12		13_26	Compression	-13.6	1.00×10^{-5}	0.1
13	Piazolo et al. (2013)	MD9		-13.6	2.50×10^{-6}	0.2
14		MD3		-10.7	2.50×10^{-6}	0.2
15		MD22		-10.7	1.00×10^{-5}	0.4

Table B.1: Table showing the experimental data used in fig. 3.4. The first column gives experimental number shown in the plot of $\mathbf{A}^{(2)}$ and beside the experimental pole figures in fig. 3.4. This is followed by the paper the data was published in and the conditions the experiment was run at.

PARAMETER SENSITIVITY STUDY

In this appendix I perform a parameter sensitivity study of the main results chapter 4. From fig. 4.5 I use the 80% confidence intervals to choose parameters to give the strongest and weakest fabrics. For the strongest fabric I use l_{\max} , $\tilde{\beta}_{\max}$, $\tilde{\lambda}_{\min}$ and vice versa. I then reproduce the figures from chapter 4 with these two parameter sets. The discussion of how sensitive the figures are to the changes in parameters is included in both chapter 4 alongside the discussion of the original figures to provide context there, and repeated here for completeness.

Figures C.1 and C.2 show fig. 4.7 reproduced with the upper and lower bound on fabric strength respectively. Figures C.1 and C.2 show that variations in the parameters from fig. 4.5 affect the strength of the primary cluster primarily, but do not affect the variation with vorticity number or the transition from one fabric type to another.

Figures C.3 and C.4 show fig. 4.9 reproduced with the upper and lower bound on fabric strength respectively. These figures show that at low vorticity numbers and temperatures, the angle between the primary cluster and compression axis is slightly sensitive to variations in parameters, but outside of this space the angle is roughly unchanged.

Figures C.5 and C.6 show the upper and lower bound for fig. 4.10. There is little change in the overall picture. The variation with vorticity number is approximately unchanged and boundaries between the regimes shift by roughly $\pm 7^\circ$ C.

Figures C.6 and C.7 show fig. 4.11 with the upper and lower bound on fabric strength respectively. These figures highlight that even if the fabric peak strength varies significantly with the change in parameters, the pattern is much less sensitive to the change in parameters.

Figures C.9 and C.10 show fig. 4.12 with the upper and lower bound on fabric strength respectively. These figures show that the halfway strain is fairly insensitive to changes in the parameters, with the maximum varying by around $\pm 20\%$. The maximum halfway strain remains at $\mathcal{W} = 0.1, T = -30^\circ$ C for both figs. C.9 and C.10. The J index at steady-state is more sensitive to changes in parameters but the general picture of how this variable changes across the T - \mathcal{W} space is similar, with the upper bound showing generally less variation across the parameter space.

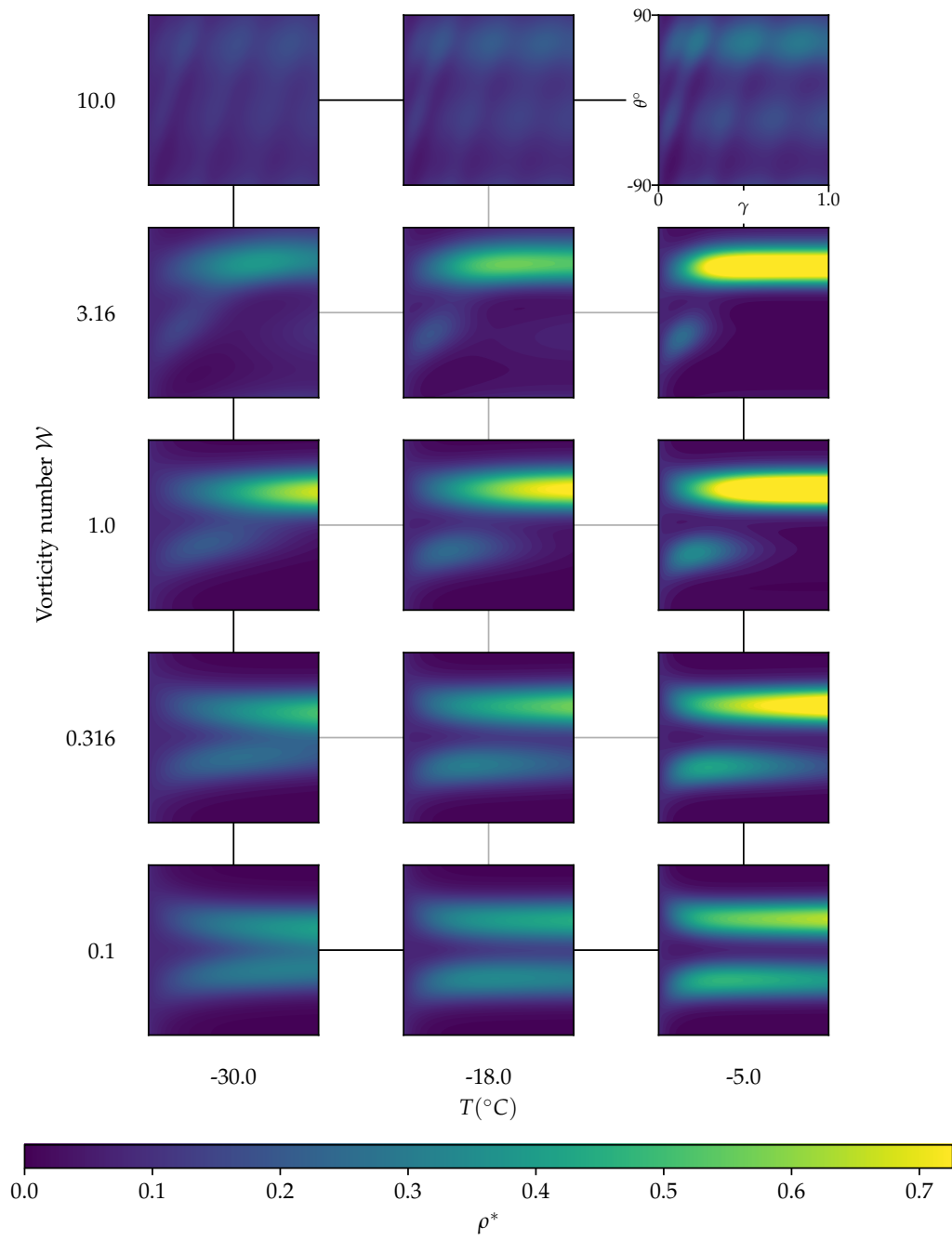


Figure C.1: As fig. 4.7 but with $\iota_{\max}, \tilde{\beta}_{\max}, \tilde{\lambda}_{\min}$, to give the strongest fabric.

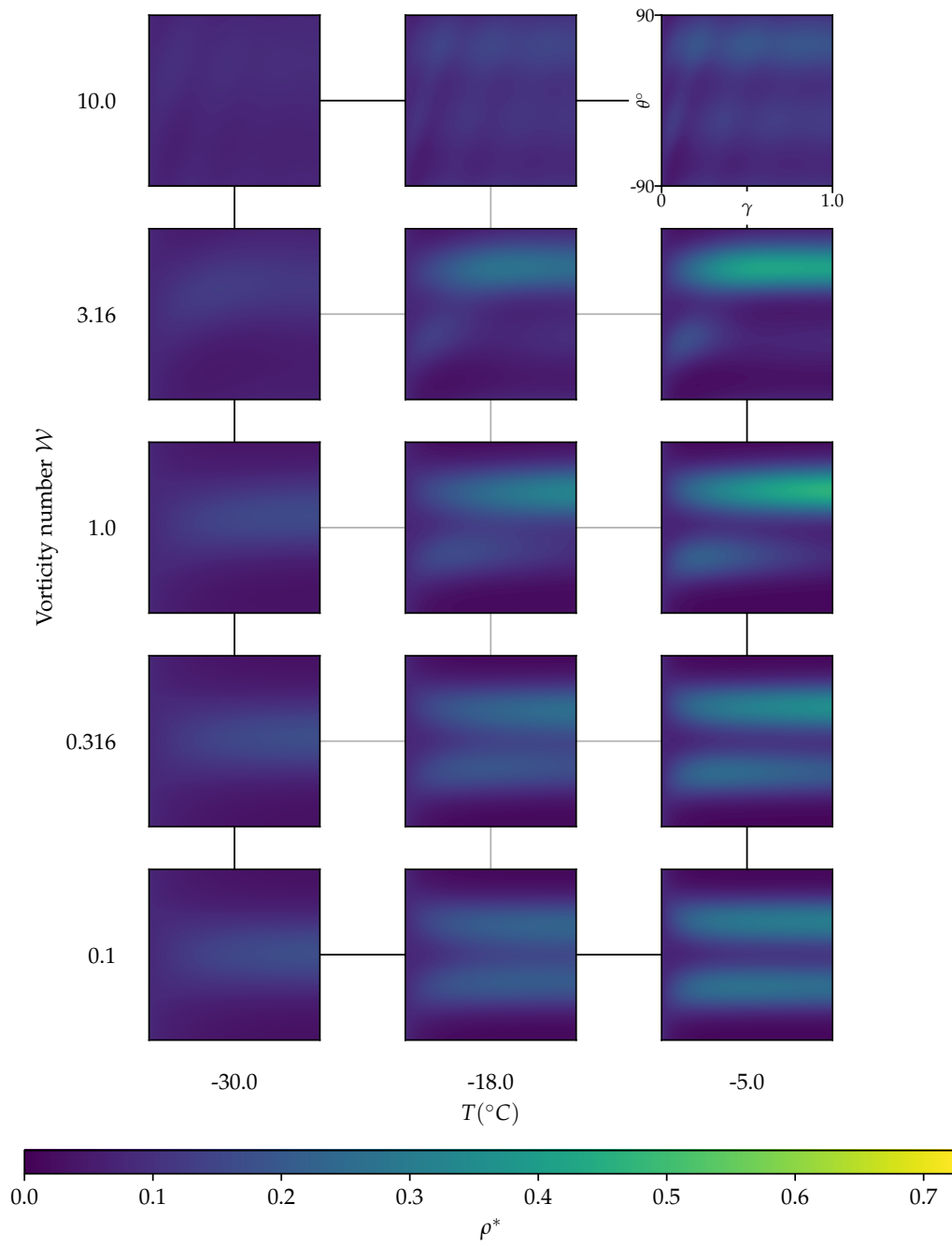


Figure C.2: As fig. 4.7 but with $l_{\min}, \tilde{\beta}_{\min}, \tilde{\lambda}_{\max}$, to give the weakest fabric.

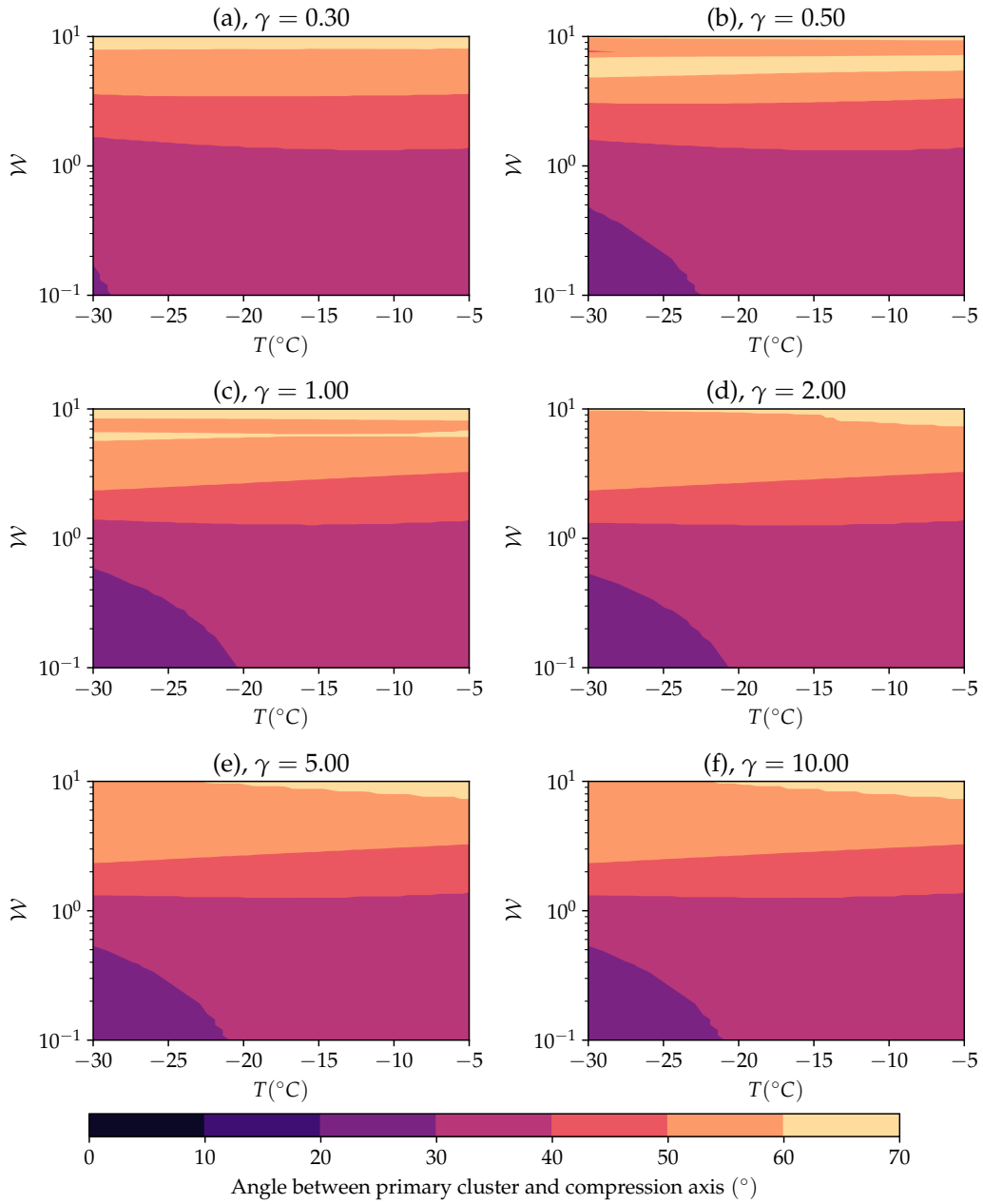


Figure C.3: As fig. 4.9 but with ι_{\max} , $\tilde{\beta}_{\max}$, $\tilde{\lambda}_{\min}$, to give the strongest fabric.

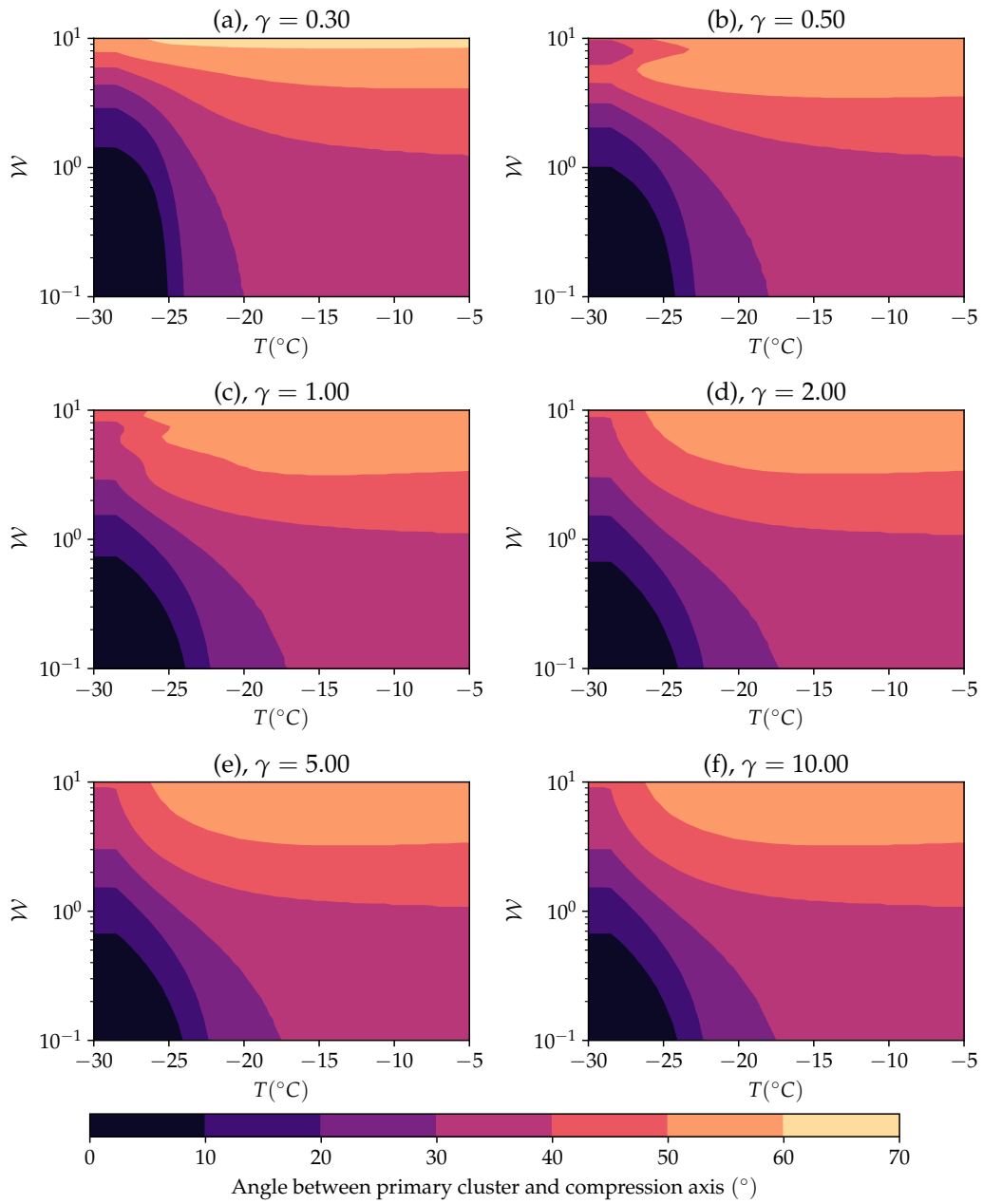


Figure C.4: As fig. 4.9 but with $l_{\min}, \tilde{\beta}_{\min}, \tilde{\lambda}_{\max}$, to give the weakest fabric.

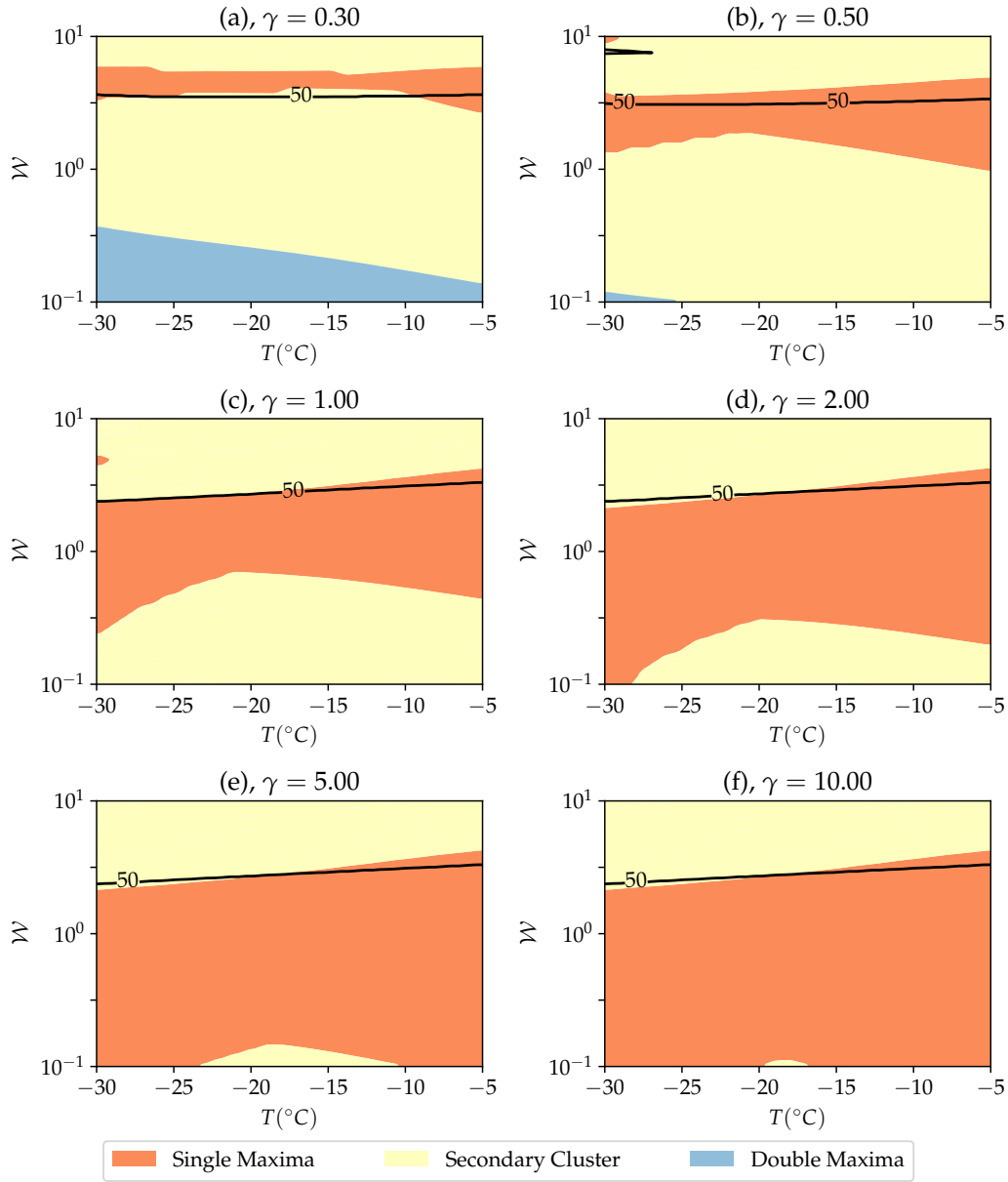


Figure C.5: As fig. 4.10 but with $l_{\max}, \tilde{\beta}_{\max}, \tilde{\lambda}_{\min}$, to give the strongest fabric.

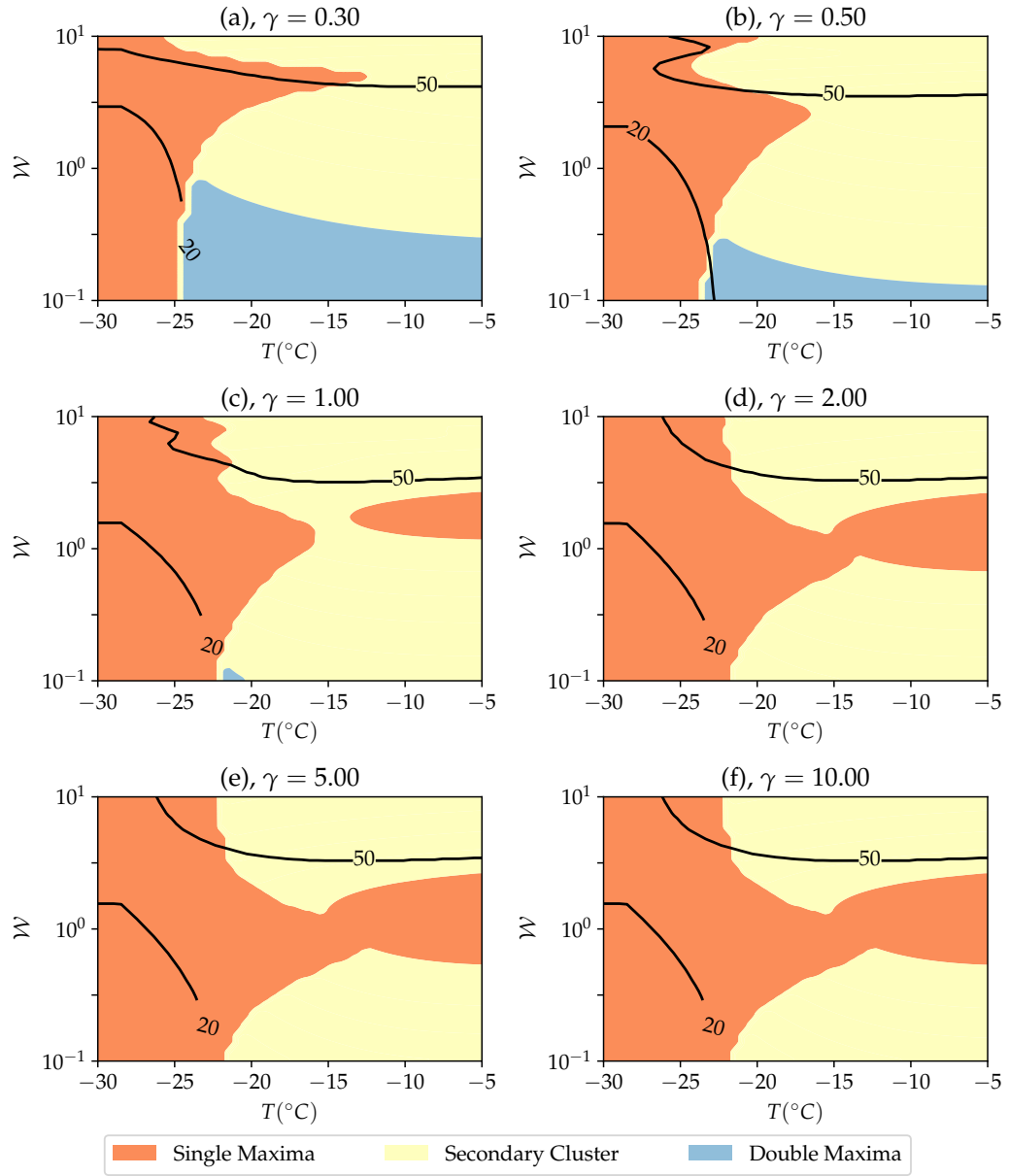


Figure C.6: As fig. 4.10 but with $l_{\min}, \tilde{\beta}_{\min}, \tilde{\lambda}_{\max}$, to give the weakest fabric.

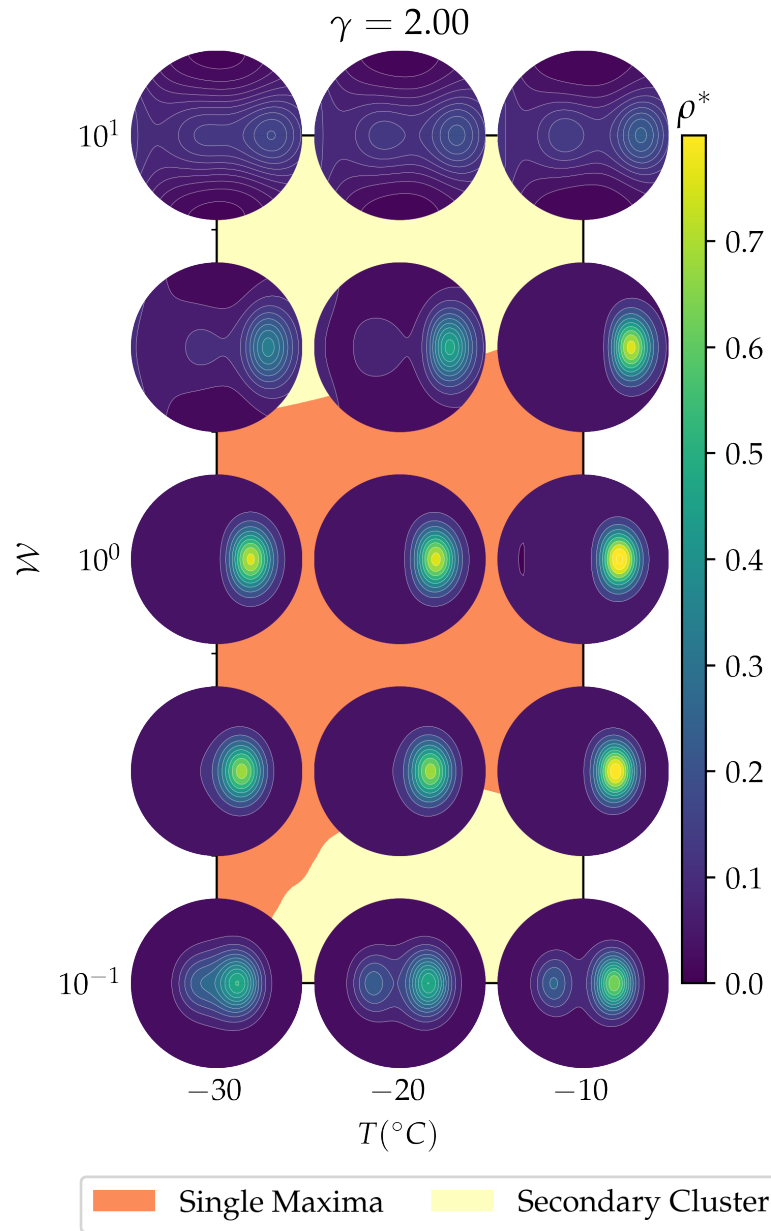


Figure C.7: As fig. 4.11 but with $\iota_{\max}, \tilde{\beta}_{\max}, \tilde{\lambda}_{\min}$, to give the strongest fabric.

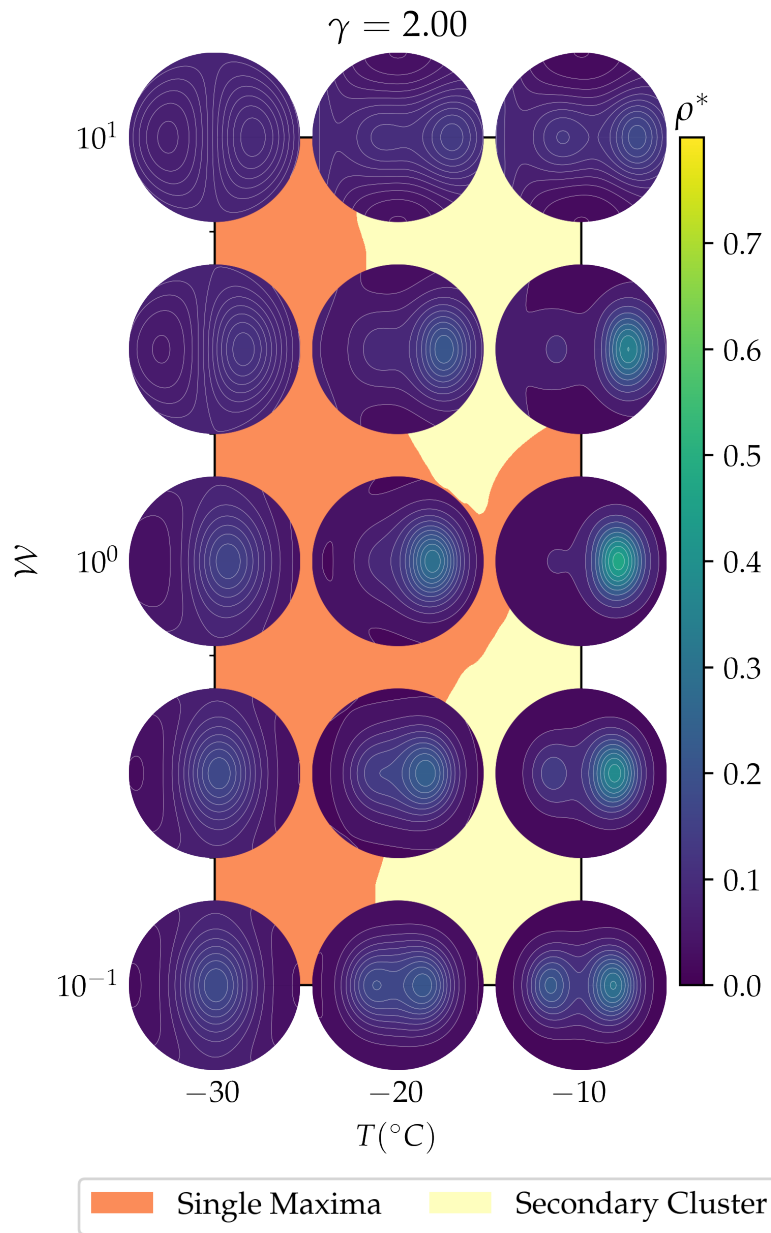


Figure C.8: As fig. 4.11 but with $l_{\min}, \tilde{\beta}_{\min}, \tilde{\lambda}_{\max}$, to give the weakest fabric.

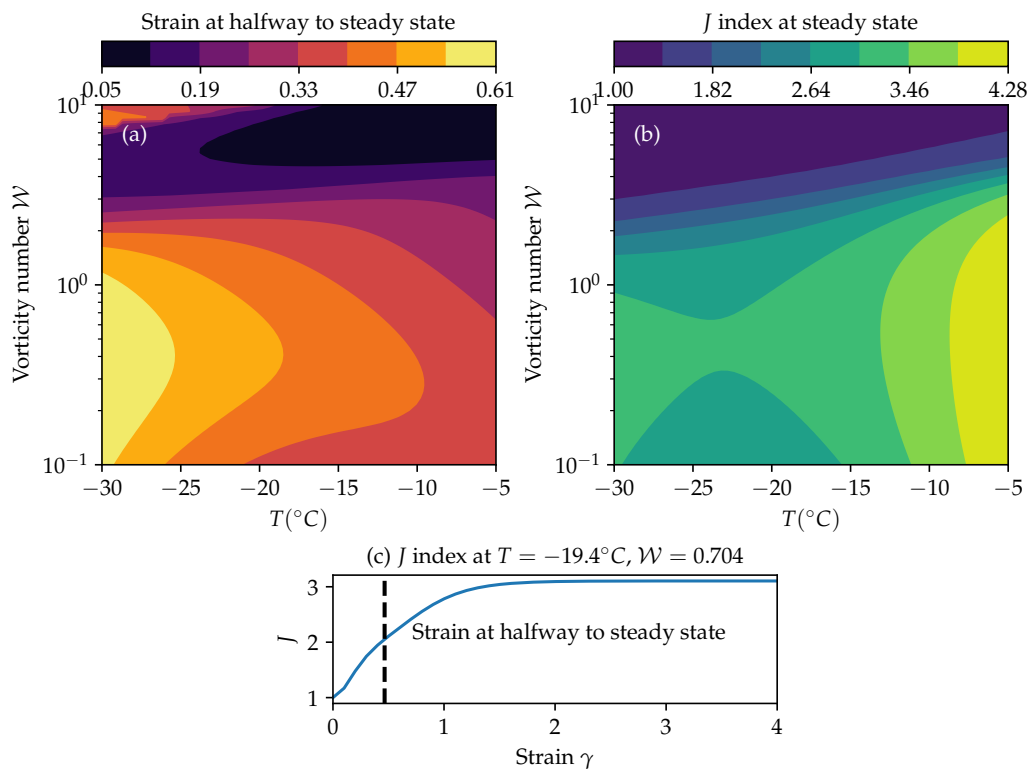


Figure C.9: As fig. 4.12 but with l_{\max} , $\tilde{\beta}_{\max}$, $\tilde{\lambda}_{\min}$, to give the strongest fabric.

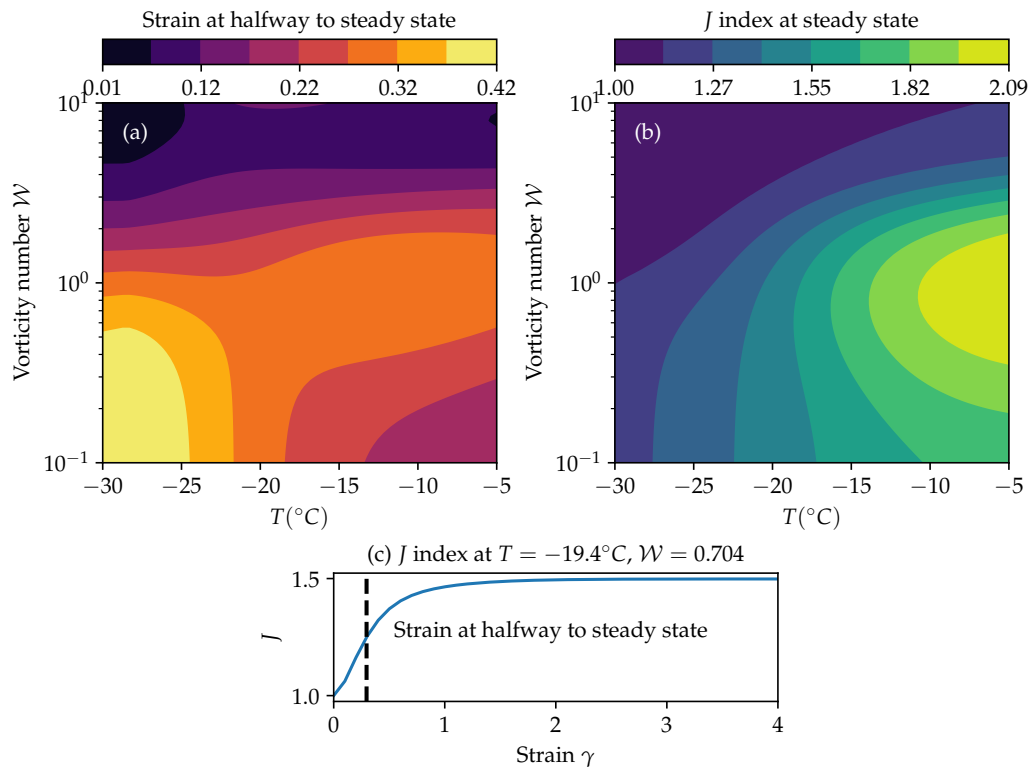


Figure C.10: As fig. 4.12 but with $l_{\min}, \tilde{\beta}_{\min}, \tilde{\lambda}_{\max}$ to give the weakest fabric.

BIBLIOGRAPHY

- Advani, Suresh G. and Charles L. Tucker (Nov. 1987). "The Use of Tensors to Describe and Predict Fiber Orientation in Short Fiber Composites." In: *Journal of Rheology* 31.8, pp. 751–784. ISSN: 0148-6055. DOI: [10.1122/1.549945](https://doi.org/10.1122/1.549945). URL: <https://doi.org/10.1122/1.549945> (visited on 10/17/2018).
- Alley, Richard B. (Apr. 1988). "Fabrics in Polar Ice Sheets: Development and Prediction." In: *Science* 240.4851, p. 493. DOI: [10.1126/science.240.4851.493](https://doi.org/10.1126/science.240.4851.493). URL: <http://science.sciencemag.org/content/240/4851/493.abstract>.
- Altan, M. C. and L. Tang (May 1993). "Orientation tensors in simple flows of dilute suspensions of non-Brownian rigid ellipsoids, comparison of analytical and approximate solutions." In: *Rheologica Acta* 32.3, pp. 227–244. ISSN: 1435-1528. DOI: [10.1007/BF00434187](https://doi.org/10.1007/BF00434187). URL: <https://doi.org/10.1007/BF00434187>.
- Arthern, R., D. P. Winebrenner, and D. Vaughan (2006). "Antarctic snow accumulation mapped using polarization of 4.3-cm wavelength microwave emission." In: *Journal of Geophysical Research* 111, pp. 1–10.
- Azuma, N., Y. Wang, K. Mori, H. Narita, T. Hondoh, H. Shoji, and O. Watanabe (1999). "Textures and fabrics in the Dome F (Antarctica) ice core." In: *Annals of Glaciology* 29. Edition: 2017/09/14 Publisher: Cambridge University Press, pp. 163–168. ISSN: 0260-3055. DOI: [10.3189/172756499781821148](https://doi.org/10.3189/172756499781821148). URL: <https://www.cambridge.org/core/article/textures-and-fabrics-in-the-dome-f-antarctica-ice-core/B020023CC77FC8BF3174D17DA9CAECBB>.
- Azuma, Nobuhiko (Feb. 1995). "A flow law for anisotropic polycrystalline ice under uniaxial compressive deformation." In: *Cold Regions Science and Technology* 23.2, pp. 137–147. ISSN: 0165-232X. DOI: [10.1016/0165-232X\(94\)00011-L](https://doi.org/10.1016/0165-232X(94)00011-L). URL: <https://www.sciencedirect.com/science/article/pii/0165232X9400011L>.
- Azuma, Nobuhiko and Akira Higashi (1984). "Mechanical Properties of Dye 3 Greenland Deep Ice Cores." In: *Annals of Glaciology* 5, pp. 1–8. ISSN: 1727-5644. DOI: [10.3189/1984AoG5-1-1-8](https://doi.org/10.3189/1984AoG5-1-1-8). URL: <https://www.cambridge.org/core/article/mechanical-properties-of-dye-3-greenland-deep-ice-cores/A8DB954AC8D9C074EA299EF5BBADD9E0>.

- Bailey, Christopher M and Eleanor L Eyster (Nov. 2003). "General shear deformation in the Pinaleño Mountains metamorphic core complex, Arizona." In: *Journal of Structural Geology* 25.11, pp. 1883–1892. ISSN: 0191-8141. DOI: [10.1016/S0191-8141\(03\)00044-0](https://doi.org/10.1016/S0191-8141(03)00044-0). URL: <https://www.sciencedirect.com/science/article/pii/S0191814103000440>.
- Bargmann, Swantje, Hakime Seddik, and Ralf Greve (May 2012). "Computational modeling of flow-induced anisotropy of polar ice for the EDML deep drilling site, Antarctica: The effect of rotation recrystallization and grain boundary migration." In: *International Journal for Numerical and Analytical Methods in Geomechanics* 36.7, pp. 892–917. ISSN: 0363-9061. DOI: [10.1002/nag.1034](https://doi.org/10.1002/nag.1034). URL: <https://doi.org/10.1002/nag.1034> (visited on 09/28/2019).
- Bennett, Matthew (June 2003). "Ice streams as the arteries of an ice sheet: Their mechanics, stability and significance." In: *Earth-Science Reviews* 61, pp. 309–339. DOI: [10.1016/S0012-8252\(02\)00130-7](https://doi.org/10.1016/S0012-8252(02)00130-7).
- Boehler, J. P. (1987). "Representations for Isotropic and Anisotropic Non-Polynomial Tensor Functions." In: *Applications of Tensor Functions in Solid Mechanics*. Ed. by J. P. Boehler. Vienna: Springer Vienna, pp. 31–53. ISBN: 978-3-7091-2810-7. DOI: [10.1007/978-3-7091-2810-7_3](https://doi.org/10.1007/978-3-7091-2810-7_3). URL: https://doi.org/10.1007/978-3-7091-2810-7_3.
- Boehler, Reinhard (May 1996). "Melting temperature of the Earth's mantle and core: Earth's thermal structure." In: *Annual Review of Earth and Planetary Sciences* 24.1, pp. 15–40. ISSN: 0084-6597. DOI: [10.1146/annurev.earth.24.1.15](https://doi.org/10.1146/annurev.earth.24.1.15). URL: <https://doi.org/10.1146/annurev.earth.24.1.15> (visited on 05/02/2019).
- Bons, P. D., T. Kleiner, M.-G. Llorens, D. J. Prior, T. Sachau, I. Weikusat, and D. Jansen (July 2018). "Greenland Ice Sheet: Higher Nonlinearity of Ice Flow Significantly Reduces Estimated Basal Motion." In: *Geophysical Research Letters* 45.13. Publisher: John Wiley & Sons, Ltd, pp. 6542–6548. ISSN: 0094-8276. DOI: [10.1029/2018GL078356](https://doi.org/10.1029/2018GL078356). URL: <https://doi.org/10.1029/2018GL078356> (visited on 11/20/2021).
- Booth, Adam D., Poul Christoffersen, Charlotte Schoonman, Andy Clarke, Bryn Hubbard, Robert Law, Samuel H. Doyle, Thomas R. Chudley, and Athena Chalari (July 2020). "Distributed Acoustic Sensing of Seismic Properties in a Borehole Drilled on a Fast-Flowing Greenlandic Outlet Glacier." In: *Geophysical Research Letters* 47.13. Publisher: John Wiley & Sons, Ltd, e2020GL088148. ISSN: 0094-8276. DOI: [10.1029/2020GL088148](https://doi.org/10.1029/2020GL088148). URL: <https://doi.org/10.1029/2020GL088148> (visited on 04/02/2021).

- Budd, W.F. and T.H. Jacka (July 1989). "A review of ice rheology for ice sheet modelling." In: *Cold Regions Science and Technology* 16.2, pp. 107–144. ISSN: 0165-232X. DOI: [10.1016/0165-232X\(89\)90014-1](https://doi.org/10.1016/0165-232X(89)90014-1). URL: <http://www.sciencedirect.com/science/article/pii/0165232X89900141>.
- Budd, William F., Roland C. Warner, T.H. Jacka, Jun Li, and Adam Treverrow (2013). "Ice flow relations for stress and strain-rate components from combined shear and compression laboratory experiments." In: *Journal of Glaciology* 59.214. Edition: 2017/07/10 Publisher: Cambridge University Press, pp. 374–392. ISSN: 0022-1430. DOI: [10.3189/2013JogG12J106](https://doi.org/10.3189/2013JogG12J106).
- Byravan, Sujatha and Sudhir Chella Rajan (2010). "The Ethical Implications of Sea-Level Rise Due to Climate Change." In: *Ethics & International Affairs* 24.3, pp. 239–260. ISSN: 0892-6794. DOI: [10.1111/j.1747-7093.2010.00266.x](https://doi.org/10.1111/j.1747-7093.2010.00266.x). URL: <https://www.cambridge.org/core/article/ethical-implications-of-sealevel-rise-due-to-climate-change/9376244C335EC648C63AA07B0BF36D1C>.
- Carreras, Jordi, John W. Cosgrove, and Elena Druguet (May 2013). "Strain partitioning in banded and/or anisotropic rocks: Implications for inferring tectonic regimes." In: *Deformation localization in rocks* 50, pp. 7–21. ISSN: 0191-8141. DOI: [10.1016/j.jsg.2012.12.003](https://doi.org/10.1016/j.jsg.2012.12.003). URL: <https://www.sciencedirect.com/science/article/pii/S019181411200274X>.
- Castelnau, O., P. Duval, M. Montagnat, and R. Brenner (Nov. 2008). "Elastoviscoplastic micromechanical modeling of the transient creep of ice." In: *Journal of Geophysical Research: Solid Earth* 113.B11. Publisher: John Wiley & Sons, Ltd. ISSN: 0148-0227. DOI: [10.1029/2008JB005751](https://doi.org/10.1029/2008JB005751). URL: <https://doi.org/10.1029/2008JB005751> (visited on 11/26/2021).
- Castelnau, Olivier, Paul Duval, Ricardo A. Lebensohn, and Gilles R. Canova (June 1996). "Viscoplastic modeling of texture development in polycrystalline ice with a self-consistent approach: Comparison with bound estimates." In: *Journal of Geophysical Research: Solid Earth* 101.B6, pp. 13851–13868. ISSN: 0148-0227. DOI: [10.1029/96JB00412](https://doi.org/10.1029/96JB00412). URL: <https://doi.org/10.1029/96JB00412> (visited on 10/24/2018).
- Chauve, T., M. Montagnat, S. Piazzolo, B. Journaux, J. Wheeler, F. Barou, D. Mainprice, and A. Tommasi (Sept. 2017). "Non-basal dislocations should be accounted for in simulating ice mass flow." In: *Earth and Planetary Science Letters* 473, pp. 247–255. ISSN: 0012-821X. DOI:

- 10.1016/j.epsl.2017.06.020. URL: <http://www.sciencedirect.com/science/article/pii/S0012821X17303308>.
- Chung, Du Hwan and Tai Hun Kwon (Jan. 2002). "Invariant-based optimal fitting closure approximation for the numerical prediction of flow-induced fiber orientation." In: *Journal of Rheology* 46.1, pp. 169–194. ISSN: 0148-6055. DOI: [10.1122/1.1423312](https://doi.org/10.1122/1.1423312). URL: <https://doi.org/10.1122/1.1423312> (visited on 08/26/2018).
- Cintra, Joaquim S. and Charles L. Tucker (Nov. 1995). "Orthotropic closure approximations for flow-induced fiber orientation." In: *Journal of Rheology* 39.6, pp. 1095–1122. ISSN: 0148-6055. DOI: [10.1122/1.550630](https://doi.org/10.1122/1.550630). URL: <https://doi.org/10.1122/1.550630> (visited on 07/27/2018).
- Conrad, Clinton P., Mark D. Behn, and Paul G. Silver (July 2007). "Global mantle flow and the development of seismic anisotropy: Differences between the oceanic and continental upper mantle." In: *Journal of Geophysical Research: Solid Earth* 112.B7. Publisher: John Wiley & Sons, Ltd. ISSN: 0148-0227. DOI: [10.1029/2006JB004608](https://doi.org/10.1029/2006JB004608). URL: <https://doi.org/10.1029/2006JB004608> (visited on 11/29/2021).
- Cornford, Stephen L., Daniel F. Martin, Daniel T. Graves, Douglas F. Ranken, Anne M. Le Brocq, Rupert M. Gladstone, Antony J. Payne, Esmond G. Ng, and William H. Lipscomb (Jan. 2013). "Adaptive mesh, finite volume modeling of marine ice sheets." In: *Journal of Computational Physics* 232.1, pp. 529–549. ISSN: 0021-9991. DOI: [10.1016/j.jcp.2012.08.037](http://www.sciencedirect.com/science/article/pii/S0021999112005050). URL: <http://www.sciencedirect.com/science/article/pii/S0021999112005050>.
- Craw, Lisa, Chao Qi, David J. Prior, David L. Goldsby, and Daeyeong Kim (Oct. 2018). "Mechanics and microstructure of deformed natural anisotropic ice." In: *Journal of Structural Geology* 115, pp. 152–166. ISSN: 0191-8141. DOI: [10.1016/j.jsg.2018.07.014](http://www.sciencedirect.com/science/article/pii/S0191814118300646). URL: <http://www.sciencedirect.com/science/article/pii/S0191814118300646>.
- Dansgaard, W. and S. J. Johnsen (1969). "A Flow Model and a Time Scale for the Ice Core from Camp Century, Greenland." In: *Journal of Glaciology* 8.53. Edition: 2017/01/30 Publisher: Cambridge University Press, pp. 215–223. ISSN: 0022-1430. DOI: [10.3189/S0022143000031208](https://doi.org/10.3189/S0022143000031208).
- Dansgaard, W., S.J. Johnsen, J. Møller, and C.C. Langway Jr. (1969). "One thousand centuries of climatic record from Camp Century on the Greenland ice sheet." In: *Science* 166.3903, pp. 377–381. DOI: [10.1126/science.166.3903.377](https://doi.org/10.1126/science.166.3903.377).
- Dmitri Kuzmin, Rainald Lohner, and Stefan Turek (2012). *Flux-Corrected Transport: Principles, Algorithms, and Applications*. Springer. ISBN: 978-

- 94-007-4038-9. URL: <https://link.springer.com/book/10.1007%2F978-94-007-4038-9#about>.
- Drury, M.R., F.J. Humphreys, and S.H. White (Nov. 1985). "Large strain deformation studies using polycrystalline magnesium as a rock analogue. Part II: dynamic recrystallisation mechanisms at high temperatures." In: *Special Issue Experiments in Solid State Physics Relevant to Lithospheric Dynamics* 40.3, pp. 208–222. ISSN: 0031-9201. DOI: [10.1016/0031-9201\(85\)90131-1](https://doi.org/10.1016/0031-9201(85)90131-1). URL: <https://www.sciencedirect.com/science/article/pii/0031920185901311>.
- Drury, M.R. and Janos Urai (Feb. 1990). "Deformation-related recrystallization process." In: *Tectonophysics* 172, pp. 235–253. DOI: [10.1016/0040-1951\(90\)90033-5](https://doi.org/10.1016/0040-1951(90)90033-5).
- Durrant, Dale R. (1999). "Semi-Lagrangian Methods." In: *Numerical Methods for Wave Equations in Geophysical Fluid Dynamics*. Ed. by Dale R. Durrant. New York, NY: Springer New York, pp. 303–333. ISBN: 978-1-4757-3081-4. DOI: [10.1007/978-1-4757-3081-4_6](https://doi.org/10.1007/978-1-4757-3081-4_6). URL: https://doi.org/10.1007/978-1-4757-3081-4_6.
- Duval, P., M. F. Ashby, and I. Anderman (Oct. 1983). "Rate-controlling processes in the creep of polycrystalline ice." In: *The Journal of Physical Chemistry* 87.21, pp. 4066–4074. ISSN: 0022-3654. DOI: [10.1021/j100244a014](https://doi.org/10.1021/j100244a014). URL: <https://doi.org/10.1021/j100244a014>.
- Duval, Paul (1981). "Creep and Fabrics of Polycrystalline Ice Under Shear and Compression." In: *Journal of Glaciology* 27.95. Edition: 2017/01/20 Publisher: Cambridge University Press, pp. 129–140. ISSN: 0022-1430. DOI: [10.3189/S002214300001128X](https://doi.org/10.3189/S002214300001128X).
- Duval, Paul and Maurine Montagnat (Apr. 2002). "Comment on "Superplastic deformation of ice: Experimental observations" by D. L. Goldsby and D. L. Kohlstedt." In: *J. Geophys. Res.* 107.
- Duval, Paul, Maurine Montagnat, Fanny Grennerat, Jerome Weiss, Jacques Meyssonier, and Armelle Philip (2010). "Creep and plasticity of glacier ice: a material science perspective." In: *Journal of Glaciology* 56.200, pp. 1059–1068. ISSN: 0022-1430. DOI: [10.3189/002214311796406185](https://doi.org/10.3189/002214311796406185). URL: <https://www.cambridge.org/core/article/creep-and-plasticity-of-glacier-ice-a-material-science-perspective/34BA86B28CE3026D0AE8FBF63BFFB54C>.
- Ettema, Janneke, Michiel R. van den Broeke, Erik van Meijgaard, Willem Jan van de Berg, Jonathan L. Bamber, Jason E. Box, and Roger C. Bales (June 2009). "Higher surface mass balance of the Greenland ice sheet revealed by high-resolution climate modeling." In: *Geophysical Research Letters* 36.12. Publisher: John Wiley & Sons,

- Ltd. ISSN: 0094-8276. DOI: [10.1029/2009GL038110](https://doi.org/10.1029/2009GL038110). URL: <https://doi.org/10.1029/2009GL038110> (visited on 11/05/2021).
- Fan, S., T. F. Hager, D. J. Prior, A. J. Cross, D. L. Goldsby, C. Qi, M. Negrini, and J. Wheeler (Nov. 2020). "Temperature and strain controls on ice deformation mechanisms: insights from the microstructures of samples deformed to progressively higher strains at -10, -20 and -30°C." In: *The Cryosphere* 14.11. Publisher: Copernicus Publications, pp. 3875–3905. ISSN: 1994-0424. DOI: [10.5194/tc-14-3875-2020](https://doi.org/10.5194/tc-14-3875-2020). URL: <https://tc.copernicus.org/articles/14/3875/2020/>.
- Faria, S.H. (Apr. 2001). "Mixtures with continuous diversity: general theory and application to polymer solutions." In: *Continuum Mechanics and Thermodynamics* 13.2, pp. 91–120. ISSN: 1432-0959. DOI: [10.1007/s001610100043](https://doi.org/10.1007/s001610100043). URL: <https://doi.org/10.1007/s001610100043>.
- Faria, Sérgio H (May 2006). "Creep and recrystallization of large polycrystalline masses. I. General continuum theory." In: *Proceedings of the Royal Society A: Mathematical, Physical and Engineering Science* 462.2069, p. 1493. DOI: [10.1098/rspa.2005.1610](https://doi.org/10.1098/rspa.2005.1610). URL: <http://rspa.royalsocietypublishing.org/content/462/2069/1493.abstract>.
- Faria, Sérgio H, Gilberto M Kremer, and Kolumban Hutter (June 2008). "Reply to Gagliardini's comment on 'Creep and recrystallization of large polycrystalline masses' by Faria and co-authors." In: *Proceedings of the Royal Society A: Mathematical, Physical and Engineering Science* 464. DOI: [10.1098/rspa.2008.0181](https://doi.org/10.1098/rspa.2008.0181). URL: <https://royalsocietypublishing.org/doi/10.1098/rspa.2008.0181>.
- Faria, Sérgio H., Ilka Weikusat, and Nobuhiko Azuma (Apr. 2014). "The microstructure of polar ice. Part II: State of the art." In: *Microdynamics of Ice* 61, pp. 21–49. ISSN: 0191-8141. DOI: [10.1016/j.jsg.2013.11.003](https://doi.org/10.1016/j.jsg.2013.11.003). URL: <http://www.sciencedirect.com/science/article/pii/S0191814113002009>.
- Fossen, Haakon and Basil Tikoff (Mar. 1993). "The deformation matrix for simultaneous simple shearing, pure shearing and volume change, and its application to transpression-transension tectonics." In: *The Geometry of Naturally Deformed Rocks* 15.3, pp. 413–422. ISSN: 0191-8141. DOI: [10.1016/0191-8141\(93\)90137-Y](https://doi.org/10.1016/0191-8141(93)90137-Y). URL: <http://www.sciencedirect.com/science/article/pii/019181419390137Y>.
- Fujita, Shuji, Hideo Maeno, and Kenichi Matsuoka (2006). "Radio-wave depolarization and scattering within ice sheets: a matrix-based model to link radar and ice-core measurements and its application." In: *Journal of Glaciology* 52.178. Edition: 2017/09/08 Publisher: Cam-

- bridge University Press, pp. 407–424. ISSN: 0022-1430. DOI: [10.3189/172756506781828548](https://doi.org/10.3189/172756506781828548).
- Gagliardini, O. et al. (Aug. 2013). “Capabilities and performance of Elmer/Ice, a new-generation ice sheet model.” In: *Geoscientific Model Development* 6, pp. 1299–1318. DOI: [10.5194/gmd-6-1299-2013](https://doi.org/10.5194/gmd-6-1299-2013).
- Gagliardini, Olivier (Feb. 2008). “Comment on the papers ‘Creep and recrystallization of large polycrystalline masses’ by Faria and co-authors.” In: *Proceedings of the Royal Society A: Mathematical, Physical and Engineering Sciences* 464.2090, pp. 289–291. DOI: [10.1098/rspa.2007.0187](https://doi.org/10.1098/rspa.2007.0187). URL: <https://doi.org/10.1098/rspa.2007.0187> (visited on 05/23/2019).
- Gagliardini, Olivier, Fabien Gillet-Chaulet, and Maurine Montagnat (2009). “A Review of Anisotropic Polar Ice Models: from Crystal to Ice-Sheet Flow Models.” In: *Physics of Ice Core Records II* 68. URL: <http://citeseerx.ist.psu.edu/viewdoc/download?doi=10.1.1.496.2886&rep=rep1&type=pdf>.
- Gerber, T. A., C. S. Hvidberg, S. O. Rasmussen, S. Franke, G. Sinnl, A. Grinsted, D. Jansen, and D. Dahl-Jensen (Aug. 2021). “Upstream flow effects revealed in the EastGRIP ice core using Monte Carlo inversion of a two-dimensional ice-flow model.” In: *The Cryosphere* 15.8. Publisher: Copernicus Publications, pp. 3655–3679. ISSN: 1994-0424. DOI: [10.5194/tc-15-3655-2021](https://doi.org/10.5194/tc-15-3655-2021). URL: <https://tc.copernicus.org/articles/15/3655/2021/>.
- Gillet-Chaulet, Fabie, Olivier Gagliardini, Jacques Meyssonier, Maurine Montagnat, and Olivier Castelnau (2005). “A user-friendly anisotropic flow law for ice-sheet modeling.” In: *Journal of Glaciology* 51.172, pp. 3–14. ISSN: 0022-1430. DOI: [10.3189/172756505781829584](https://doi.org/10.3189/172756505781829584). URL: <https://www.cambridge.org/core/journals/journal-of-glaciology/article/userfriendly-anisotropic-flow-law-for-icesheet-modeling/09883516ED5805B13E3D2446B3EC0911>.
- Gillet-Chaulet, Fabien, Olivier Gagliardini, Jacques Meyssonier, Thomas Zwinger, and Juha Ruokolainen (Mar. 2006). “Flow-induced anisotropy in polar ice and related ice-sheet flow modelling.” In: *2nd Annual European Rheology Conference* 134.1, pp. 33–43. ISSN: 0377-0257. DOI: [10.1016/j.jnnfm.2005.11.005](https://doi.org/10.1016/j.jnnfm.2005.11.005). URL: <http://www.sciencedirect.com/science/article/pii/S0377025705002648>.
- Glen, J. W. (1952). “Experiments on the Deformation of Ice.” In: *Journal of Glaciology* 2.12, pp. 111–114. ISSN: 0022-1430. DOI: [10.3189/S0022143000034067](https://doi.org/10.3189/S0022143000034067).

- Glen, J. W. (Feb. 1968). "The effect of hydrogen disorder on dislocation movement and plastic deformation of ice." In: *Physik der kondensierten Materie* 7.1, pp. 43–51. ISSN: 1431-584X. DOI: [10.1007/BF02422799](https://doi.org/10.1007/BF02422799). URL: <https://doi.org/10.1007/BF02422799>.
- Goldsby, D. L. and D. L. Kohlstedt (1997). "Grain boundary sliding in fine-grained ice I." In: *Scripta Materialia* 37.9. ISBN: 1359-6462 Publisher: Citeseer, pp. 1399–1406.
- (June 2001). "Superplastic deformation of ice: Experimental observations." In: *Journal of Geophysical Research: Solid Earth* 106.B6, pp. 11017–11030. ISSN: 0148-0227. DOI: [10.1029/2000JB900336](https://doi.org/10.1029/2000JB900336). URL: <https://doi.org/10.1029/2000JB900336> (visited on 05/23/2019).
- Goodman, D. J., H. J. Frost, and M. F. Ashby (Mar. 1981). "The plasticity of polycrystalline ice." In: *Philosophical Magazine A* 43.3. Publisher: Taylor & Francis, pp. 665–695. ISSN: 0141-8610. DOI: [10.1080/01418618108240401](https://doi.org/10.1080/01418618108240401). URL: <https://doi.org/10.1080/01418618108240401>.
- Gottstein, Gunter and Lasar S. Shvindlerman (1999). *Grain Boundary Migration in Metals: Thermodynamics, Kinetics and Applications*. CRC Press.
- Gow, Anthony Jack (1961). "Deep core studies of the accumulation and densification of snow at Byrd Station and Little America V, Antarctica." In: *CRREL Research Report*. 197th ser. URL: <https://hdl.handle.net/11681/5803>.
- Graham, F. S., M. Morlighem, R. C. Warner, and A. Treverrow (2018). "Implementing an empirical scalar constitutive relation for ice with flow-induced polycrystalline anisotropy in large-scale ice sheet models." In: *The Cryosphere* 12.3, pp. 1047–1067. DOI: [10.5194/tc-12-1047-2018](https://doi.org/10.5194/tc-12-1047-2018). URL: <https://www.the-cryosphere.net/12/1047/2018/>.
- Grinsted, Aslak and Dorthe Dahl-Jensen (2002). "A Monte Carlo-tuned model of the flow in the NorthGRIP area." In: *Annals of Glaciology* 35. Edition: 2017/09/14 Publisher: Cambridge University Press, pp. 527–530. ISSN: 0260-3055. DOI: [10.3189/172756402781817130](https://doi.org/10.3189/172756402781817130).
- Gusmeroli, Alessio, Erin C. Pettit, Joseph H. Kennedy, and Catherine Ritz (Sept. 2012). "The crystal fabric of ice from full-waveform borehole sonic logging." In: *Journal of Geophysical Research: Earth Surface* 117.F3. Publisher: John Wiley & Sons, Ltd. ISSN: 0148-0227. DOI: [10.1029/2012JF002343](https://doi.org/10.1029/2012JF002343). URL: <https://doi.org/10.1029/2012JF002343> (visited on 09/09/2021).
- Gödert, Günter (2003). "A mesoscopic approach for modelling texture evolution of polar ice including recrystallization phenomena." In:

- Annals of Glaciology* 37, pp. 23–28. ISSN: 0260-3055. DOI: [10.3189/172756403781815375](https://doi.org/10.3189/172756403781815375).
- Hindmarsh, Richard C. A. (2004). “Thermoviscous stability of ice-sheet flows.” In: *Journal of Fluid Mechanics* 502, pp. 17–40. ISSN: 1469-7645. DOI: [10.1017/S0022112003007390](https://doi.org/10.1017/S0022112003007390). URL: <https://www.cambridge.org/core/article/thermoviscous-stability-of-icesheet-flows/13E3DB8CEFF97DB4A911E9F174B8E994>.
- Holtzschcher, J. J., G. de Q. Robin, and J. W. Glen (1954). “Depth of Polar Ice Caps.” In: *The Geographical Journal* 120.2. Publisher: [Wiley, Royal Geographical Society (with the Institute of British Geographers)], pp. 193–202. ISSN: 00167398, 14754959. DOI: [10.2307/1791535](https://doi.org/10.2307/1791535). URL: <http://www.jstor.org/stable/1791535> (visited on 03/29/2021).
- Hruby, Kate, Christopher Gerbi, Peter Koons, Seth Campbell, Carlos Martín, and Robert Hawley (2020). “The impact of temperature and crystal orientation fabric on the dynamics of mountain glaciers and ice streams.” In: *Journal of Glaciology*. Edition: 2020/06/29 Publisher: Cambridge University Press, pp. 1–11. ISSN: 0022-1430. DOI: [10.1017/jog.2020.44](https://doi.org/10.1017/jog.2020.44).
- Hudleston, P. Ji (1977). “Progressive deformation and development of fabric across zones of shear in glacial ice.” In: *Energetics of geological processes*. Springer, pp. 121–150.
- Humphreys, F.J. and M. Hatherly (2004). *Recrystallization and Related Annealing Phenomena*. Pergamon, Oxford.
- Jack, D. A. and D. E. Smith (Aug. 2005). “An invariant based fitted closure of the sixth-order orientation tensor for modeling short-fiber suspensions.” In: *Journal of Rheology* 49.5, pp. 1091–1115. ISSN: 0148-6055. DOI: [10.1122/1.2000970](https://doi.org/10.1122/1.2000970). URL: <https://doi.org/10.1122/1.2000970> (visited on 04/12/2019).
- Jacka, T. H. (2000). “Flow rates and crystal orientation fabrics in compression of polycrystalline ice at low temperatures and stresses.” In: *Physics of Ice Core Record*. URL: <https://ci.nii.ac.jp/naid/10015735360/en/>.
- Jacka, T.H. and M. Maccagnan (Mar. 1984). “Ice crystallographic and strain rate changes with strain in compression and extension.” In: *Cold Regions Science and Technology* 8.3, pp. 269–286. ISSN: 0165-232X. DOI: [10.1016/0165-232X\(84\)90058-2](https://doi.org/10.1016/0165-232X(84)90058-2). URL: <http://www.sciencedirect.com/science/article/pii/0165232X84900582>.
- Jiang, Dazhi (Jan. 1994). “Vorticity determination, distribution, partitioning and the heterogeneity and non-steadiness of natural de-

- formations." In: *Journal of Structural Geology* 16.1, pp. 121–130. ISSN: 0191-8141. DOI: [10.1016/0191-8141\(94\)90023-X](https://doi.org/10.1016/0191-8141(94)90023-X). URL: <https://www.sciencedirect.com/science/article/pii/019181419490023X>.
- Johnsen, Sigfus J., Dorthe Dahl-Jensen, Willi Dansgaard, and Niels Gundestrup (Jan. 1995). "Greenland palaeotemperatures derived from GRIP bore hole temperature and ice core isotope profiles." In: *Tellus B: Chemical and Physical Meteorology* 47.5. Publisher: Taylor & Francis, pp. 624–629. ISSN: null. DOI: [10.3402/tellusb.v47i5.16077](https://doi.org/10.3402/tellusb.v47i5.16077). URL: <https://doi.org/10.3402/tellusb.v47i5.16077>.
- Jordan, Thomas M., Dustin M. Schroeder, Cooper W. Elsworth, and Matthew R. Siegfried (2020). "Estimation of ice fabric within Whillans Ice Stream using polarimetric phase-sensitive radar sounding." In: *Annals of Glaciology* 61.81. Edition: 2020/02/03 Publisher: Cambridge University Press, pp. 74–83. ISSN: 0260-3055. DOI: [10.1017/aog.2020.6](https://doi.org/10.1017/aog.2020.6). URL: <https://www.cambridge.org/core/journals/annals-of-glaciology/article/estimation-of-ice-fabric-within-whillans-ice-stream-using-polarimetric-phasesensitive-radar-sounding/F334B5CE907DBED94E7614EFB32E1DAF>.
- Joughin, Ian, Ben E. Smith, and Ian M. Howat (2018). "A complete map of Greenland ice velocity derived from satellite data collected over 20 years." In: *Journal of Glaciology* 64.243. Edition: 2017/11/21 Publisher: Cambridge University Press, pp. 1–11. ISSN: 0022-1430. DOI: [10.1017/jog.2017.73](https://doi.org/10.1017/jog.2017.73). URL: <https://www.cambridge.org/core/article/complete-map-of-greenland-ice-velocity-derived-from-satellite-data-collected-over-20-years/D22454AF22391DF03754BE6DF4C70366>.
- Journaux, B., T. Chauve, M. Montagnat, A. Tommasi, F. Barou, D. Mainprice, and L. Gest (May 2019). "Recrystallization processes, microstructure and crystallographic preferred orientation evolution in polycrystalline ice during high-temperature simple shear." In: *The Cryosphere* 13.5, pp. 1495–1511. ISSN: 1994-0424. DOI: [10.5194/tc-13-1495-2019](https://doi.org/10.5194/tc-13-1495-2019). URL: <https://www.the-cryosphere.net/13/1495/2019/>.
- Jun, Li, T.H Jacka, and W.F. Budd (1996). "Deformation rates in combined compression and shear for ice which is initially isotropic and after the development of strong anisotropy." In: *Annals of Glaciology* 23. Edition: 2017/01/20 Publisher: Cambridge University Press, pp. 247–252. ISSN: 0260-3055. DOI: [10.3189/S0260305500013501](https://doi.org/10.3189/S0260305500013501). URL: <https://www.cambridge.org/core/article/deformation-rates-in-combined-compression-and-shear-for-ice-which-is>

- initially-isotropic-and-after-the-development-of-strong-anisotropy/87ABC4DFAFFA123128C6CA2E883CAE6E.
- Kamb, Barclay (1972). "Experimental Recrystallization of Ice Under Stress." In: *Flow and Fracture of Rocks*. American Geophysical Union (AGU), pp. 211–241. ISBN: 978-1-118-66406-3. DOI: [10.1029/GM016p0211](https://doi.org/10.1029/GM016p0211). URL: <https://agupubs.onlinelibrary.wiley.com/doi/abs/10.1029/GM016p0211>.
- Kamb, W. Barclay (1961). "The Glide Direction in Ice." In: *Journal of Glaciology* 3.30. Edition: 2017/01/30 Publisher: Cambridge University Press, pp. 1097–1106. ISSN: 0022-1430. DOI: [10.3189/S0022143000017500](https://doi.org/10.3189/S0022143000017500). URL: <https://www.cambridge.org/core/article/gleide-direction-in-ice/011C7686746A7C40882BA2902A728595>.
- Kennedy, Joseph H. and Erin C. Pettit (2015). "The response of fabric variations to simple shear and migration recrystallization." In: *Journal of Glaciology* 61.227, pp. 537–550. ISSN: 0022-1430. DOI: [10.3189/2015JoG14J156](https://doi.org/10.3189/2015JoG14J156). URL: <https://www.cambridge.org/core/journals/journal-of-glaciology/article/response-of-fabric-variations-to-simple-shear-and-migration-recrystallization/CFE83A878F70F5F8E7135C28A77FF9C0>.
- Kennedy, Joseph H., Erin C. Pettit, and Carlos L. Di Prinzio (2013). "The evolution of crystal fabric in ice sheets and its link to climate history." In: *Journal of Glaciology* 59.214, pp. 357–373. ISSN: 0022-1430. DOI: [10.3189/2013JoG12J159](https://doi.org/10.3189/2013JoG12J159).
- Kirchner, Nina, Columban Hutter, Martin Jakobsson, and Richard Gyllencreutz (Dec. 2011). "Capabilities and limitations of numerical ice sheet models: A discussion for Earth-scientists and modelers." In: *Quaternary Science Reviews - QUATERNARY SCI REV* 30. DOI: [10.1016/j.quascirev.2011.09.012](https://doi.org/10.1016/j.quascirev.2011.09.012).
- Kluskiwicz, Dan, EDWIN WADDINGTON, Sridhar Anandakrishnan, Donald Voigt, Kenny Matsuoka, and MICHAEL McCARTHY (Apr. 2017). "Sonic methods for measuring crystal orientation fabric in ice, and results from the West Antarctic ice sheet (WAIS) Divide." In: *Journal of Glaciology* 63, pp. 1–15. DOI: [10.1017/jog.2017.20](https://doi.org/10.1017/jog.2017.20).
- Kronenberg, Andreas K., Stephen H. Kirby, and John Pinkston (Nov. 1990). "Basal slip and mechanical anisotropy of biotite." In: *Journal of Geophysical Research: Solid Earth* 95.B12. Publisher: John Wiley & Sons, Ltd, pp. 19257–19278. ISSN: 0148-0227. DOI: [10.1029/JB095iB12p19257](https://doi.org/10.1029/JB095iB12p19257). URL: <https://doi.org/10.1029/JB095iB12p19257> (visited on 05/07/2020).

- Larour, E, H Seroussi, M Morlighem, and E Rignot (2012). "Continental scale, high order, high spatial resolution, ice sheet modeling using the Ice Sheet System Model (ISSM)." In: *Journal of Geophysical Research: Earth Surface* 117.F1. DOI: [10.1029/2011JF002140](https://doi.org/10.1029/2011JF002140). URL: <https://agupubs.onlinelibrary.wiley.com/doi/abs/10.1029/2011JF002140>.
- Lilien, David A., Nicholas M. Rathmann, Christine S. Hvidberg, and Dorthe Dahl-Jensen (Sept. 2021). "Modeling Ice-Crystal Fabric as a Proxy for Ice-Stream Stability." In: *Journal of Geophysical Research: Earth Surface* 126.9. Publisher: John Wiley & Sons, Ltd, e2021JF006306. ISSN: 2169-9003. DOI: [10.1029/2021JF006306](https://doi.org/10.1029/2021JF006306). URL: <https://doi.org/10.1029/2021JF006306> (visited on 11/10/2021).
- Lipscomb, W. et al. (July 2018). "Description and Evaluation of the Community Ice Sheet Model (CISM) v2.1." In: *Geoscientific Model Development Discussions*, pp. 1–65. DOI: [10.5194/gmd-2018-151](https://doi.org/10.5194/gmd-2018-151).
- Llorens, Maria-Gema, Albert Griera, Paul D. Bons, Ricardo A. Lebensohn, Lynn A. Evans, Daniela Jansen, and Ilka Weikusat (Sept. 2016). "Full-field predictions of ice dynamic recrystallisation under simple shear conditions." In: *Earth and Planetary Science Letters* 450, pp. 233–242. ISSN: 0012-821X. DOI: [10.1016/j.epsl.2016.06.045](https://doi.org/10.1016/j.epsl.2016.06.045). URL: <http://www.sciencedirect.com/science/article/pii/S0012821X16303326>.
- Lutz, Franz et al. (Sept. 2020). "Constraining Ice Shelf Anisotropy Using Shear Wave Splitting Measurements from Active-Source Borehole Seismics." In: *Journal of Geophysical Research: Earth Surface* 125.9. Publisher: John Wiley & Sons, Ltd, e2020JF005707. ISSN: 2169-9003. DOI: [10.1029/2020JF005707](https://doi.org/10.1029/2020JF005707). URL: <https://doi.org/10.1029/2020JF005707> (visited on 01/14/2021).
- Ma, Ying, Olivier Gagliardini, Catherine Ritz, Fabien Gillet-Chaulet, Gaël Durand, and Maurine Montagnat (2010). "Enhancement factors for grounded ice and ice shelves inferred from an anisotropic ice-flow model." In: *Journal of Glaciology* 56.199. Edition: 2017/09/08. Publisher: Cambridge University Press, pp. 805–812. ISSN: 0022-1430. DOI: [10.3189/002214310794457209](https://doi.org/10.3189/002214310794457209).
- Maljaars, Jakob M., Chris N. Richardson, and Nathan Sime (Jan. 2021). "LEoPart: A particle library for FEniCS." In: *Development and Application of Open-source Software for Problems with Numerical PDEs* 81, pp. 289–315. ISSN: 0898-1221. DOI: [10.1016/j.camwa.2020.04.023](https://doi.org/10.1016/j.camwa.2020.04.023). URL: <https://www.sciencedirect.com/science/article/pii/S089812212030170X>.

- Martin Alnæs et al. (2015). "The FEniCS Project Version 1.5." In: *Archive of Numerical Software* 3.100, pp. 9–23. DOI: [10.11588/ans.2015.100.20553](https://doi.org/10.11588/ans.2015.100.20553).
- Martín, Carlos, G. Hilmar Gudmundsson, Hamish D. Pritchard, and Olivier Gagliardini (Dec. 2009). "On the effects of anisotropic rheology on ice flow, internal structure, and the age-depth relationship at ice divides." In: *Journal of Geophysical Research: Earth Surface* 114.F4. Publisher: John Wiley & Sons, Ltd. ISSN: 0148-0227. DOI: [10.1029/2008JF001204](https://doi.org/10.1029/2008JF001204). URL: <https://doi.org/10.1029/2008JF001204> (visited on 03/19/2021).
- Matsuoka, Kenichi, Teruo Furukawa, Shuji Fujita, Hideo Maeno, Seiho Uratsuka, Renji Naruse, and Okitsugu Watanabe (Oct. 2003). "Crystal orientation fabrics within the Antarctic ice sheet revealed by a multipolarization plane and dual-frequency radar survey." In: *Journal of Geophysical Research: Solid Earth* 108.B10. Publisher: John Wiley & Sons, Ltd. ISSN: 0148-0227. DOI: [10.1029/2003JB002425](https://doi.org/10.1029/2003JB002425). URL: <https://doi.org/10.1029/2003JB002425> (visited on 03/30/2021).
- Meyssonier, Jacques and Armelle Philip (1996). "A model for the tangent viscous behaviour of anisotropic polar ice." In: *Annals of Glaciology* 23, pp. 253–261. ISSN: 0260-3055. DOI: [10.3189/S0260305500013513](https://doi.org/10.3189/S0260305500013513). URL: <https://www.cambridge.org/core/journals/annals-of-glaciology/article/model-for-the-tangent-viscous-behaviour-of-anisotropic-polar-ice/40BF287CD2E42F440BAC0835E3EB3E87>.
- Milani, Lisa, Mark S. Kulie, Daniele Casella, Stefano Dietrich, Tristan S. L'Ecuyer, Giulia Panegrossi, Federico Porcù, Paolo Sandò, and Norman B. Wood (Nov. 2018). "CloudSat snowfall estimates over Antarctica and the Southern Ocean: An assessment of independent retrieval methodologies and multi-year snowfall analysis." In: *Atmospheric Research* 213, pp. 121–135. ISSN: 0169-8095. DOI: [10.1016/j.atmosres.2018.05.015](https://doi.org/10.1016/j.atmosres.2018.05.015). URL: <https://www.sciencedirect.com/science/article/pii/S0169809517310682>.
- Minchew, Brent, Colin Meyer, Alexander Robel, Gudmundur Gudmundsson, and Mark Simons (June 2018). "Processes controlling the downstream evolution of ice rheology in glacier shear margins: case study on Rutford Ice Stream, West Antarctica." In: *Journal of Glaciology* 64, pp. 1–12. DOI: [10.1017/jog.2018.47](https://doi.org/10.1017/jog.2018.47).
- Montagnat, M., D. Buiron, L. Arnaud, A. Broquet, P. Schlitz, R. Jacob, and S. Kipfstuhl (Dec. 2012). "Measurements and numerical simulation of fabric evolution along the Talos Dome ice core, Antarctica." In: *Earth and Planetary Science Letters* 357–358, pp. 168–178. ISSN:

- 0012-821X. DOI: [10.1016/j.epsl.2012.09.025](https://doi.org/10.1016/j.epsl.2012.09.025). URL: <https://www.sciencedirect.com/science/article/pii/S0012821X12005213>.
- Montagnat, M. et al. (2014a). “Fabric along the NEEM ice core, Greenland, and its comparison with GRIP and NGRIP ice cores.” In: *The Cryosphere* 8.4, pp. 1129–1138. DOI: [10.5194/tc-8-1129-2014](https://doi.org/10.5194/tc-8-1129-2014). URL: <https://www.the-cryosphere.net/8/1129/2014/>.
- Montagnat, M. et al. (Apr. 2014b). “Multiscale modeling of ice deformation behavior.” In: *Microdynamics of Ice* 61, pp. 78–108. ISSN: 0191-8141. DOI: [10.1016/j.jsg.2013.05.002](https://doi.org/10.1016/j.jsg.2013.05.002). URL: <http://www.sciencedirect.com/science/article/pii/S0191814113000837>.
- Montagnat, Maurine, Thomas Chauve, Fabrice Barou, Andrea Tommasi, Benoît Beausir, and Claude Fressengeas (2015). “Analysis of Dynamic Recrystallization of Ice from EBSD Orientation Mapping.” In: *Frontiers in Earth Science* 3, p. 81. ISSN: 2296-6463. DOI: [10.3389/feart.2015.00081](https://doi.org/10.3389/feart.2015.00081). URL: <https://www.frontiersin.org/article/10.3389/feart.2015.00081>.
- Montagnat, Maurine, Henning Löwe, Neige Calonne, Martin Schneebeli, Margret Matzl, and Matthias Jaggi (Sept. 2020). “On the Birth of Structural and Crystallographic Fabric Signals in Polar Snow: A Case Study From the EastGRIP Snowpack.” In: *Frontiers in Earth Science* 8, p. 365. DOI: [10.3389/feart.2020.00365](https://doi.org/10.3389/feart.2020.00365).
- Montgomery-Smith, S., David A. Jack, and Douglas E. Smith (July 2010). “A systematic approach to obtaining numerical solutions of Jeffery’s type equations using Spherical Harmonics.” In: *Composites Part A: Applied Science and Manufacturing* 41.7, pp. 827–835. ISSN: 1359-835X. DOI: [10.1016/j.compositesa.2010.02.010](https://doi.org/10.1016/j.compositesa.2010.02.010). URL: <http://www.sciencedirect.com/science/article/pii/S1359835X10000679>.
- Morlighem, M. et al. (Nov. 2017). “BedMachine v3: Complete Bed Topography and Ocean Bathymetry Mapping of Greenland From Multibeam Echo Sounding Combined With Mass Conservation.” In: *Geophysical Research Letters* 44.21. Publisher: John Wiley & Sons, Ltd, pp. 11,051–11,061. ISSN: 0094-8276. DOI: [10.1002/2017GL074954](https://doi.org/10.1002/2017GL074954). URL: <https://doi.org/10.1002/2017GL074954> (visited on 11/05/2021).
- Mouginot, J., E. Rignot, and B. Scheuchl (Aug. 2019). “Continent-Wide, Interferometric SAR Phase, Mapping of Antarctic Ice Velocity.” In: *Geophysical Research Letters* 46.16. Publisher: John Wiley & Sons, Ltd, pp. 9710–9718. ISSN: 0094-8276. DOI: [10.1029/2019GL083826](https://doi.org/10.1029/2019GL083826). URL: <https://doi.org/10.1029/2019GL083826> (visited on 11/24/2020).

- Nicolas, Adolphe and Nikolas I. Christensen (1987). "Formation of Anisotropy in Upper Mantle Peridotites - A Review." In: *Composition, Structure and Dynamics of the Lithosphere-Asthenosphere System*. American Geophysical Union (AGU), pp. 111–123. ISBN: 978-1-118-67041-5. URL: <https://agupubs.onlinelibrary.wiley.com/doi/abs/10.1029/GD016p0111>.
- Ossipyan, Yu.A. and Victor Petrenko (Jan. 1988). "The Physics of Ice." In: *Europhysics News* 19, pp. 61–64. DOI: [10.1051/epn/19881905061](https://doi.org/10.1051/epn/19881905061).
- Passchier, C.W (Jan. 1991). "The classification of dilatant flow types." In: *Journal of Structural Geology* 13.1, pp. 101–104. ISSN: 0191-8141. DOI: [10.1016/0191-8141\(91\)90105-R](https://doi.org/10.1016/0191-8141(91)90105-R). URL: <http://www.sciencedirect.com/science/article/pii/019181419190105R>.
- Paterson, W. S. B. (Sept. 1999). *The Physics of Glaciers*. 3rd. Pergamon, Oxford. ISBN: 978-0-7506-4742-7. (Visited on 11/08/2019).
- Pattyn, F. et al. (Aug. 2008). "Benchmark experiments for higher-order and full-Stokes ice sheet models (ISMIP–HOM)." In: *The Cryosphere* 2.2. Publisher: Copernicus Publications, pp. 95–108. ISSN: 1994-0424. DOI: [10.5194/tc-2-95-2008](https://doi.org/10.5194/tc-2-95-2008). URL: <https://www.the-cryosphere.net/2/95/2008/>.
- Petrenko, Victor F. and Robert W. Whitworth (2002). *Physics of Ice*. eng. Oxford: Oxford University Press. ISBN: 978-0-19-851894-5. DOI: [10.1093/acprof:oso/9780198518945.001.0001](https://doi.org/10.1093/acprof:oso/9780198518945.001.0001). URL: <https://oxford.universitypressscholarship.com/10.1093/acprof:oso/9780198518945.001.0001/acprof-9780198518945>.
- Piazolo, S., M. W. Jessell, D. J. Prior, and P. D. Bons (Mar. 2004). "The integration of experimental in-situ EBSD observations and numerical simulations: a novel technique of microstructural process analysis." In: *Journal of Microscopy* 213.3. Publisher: John Wiley & Sons, Ltd, pp. 273–284. ISSN: 0022-2720. DOI: [10.1111/j.0022-2720.2004.01304.x](https://doi.org/10.1111/j.0022-2720.2004.01304.x). URL: <https://doi.org/10.1111/j.0022-2720.2004.01304.x> (visited on 02/04/2021).
- Piazolo, S., M. Montagnat, F. Grennerat, H. Moulinec, and J. Wheeler (May 2015). "Effect of local stress heterogeneities on dislocation fields." In: *examples from transient creep in polycrystalline ice* 90, pp. 303–309. ISSN: 1359-6454. DOI: [10.1016/j.actamat.2015.02.046](https://doi.org/10.1016/j.actamat.2015.02.046). URL: <http://www.scopus.com/inward/record.url?scp=84925256590&partnerID=8YFLogxK>.
- Piazolo, Sandra, P.D Bons, and C.W Passchier (July 2002). "The influence of matrix rheology and vorticity on fabric development of populations of rigid objects during plane strain deformation." In: *Tectono-*

physics 351.4, pp. 315–329. ISSN: 0040-1951. DOI: [10.1016/S0040-1951\(02\)00220-2](https://doi.org/10.1016/S0040-1951(02)00220-2). URL: <https://www.sciencedirect.com/science/article/pii/S0040195102002202>.

Piazolo, Sandra, Christopher J. L. Wilson, Vladimir Luzin, Christophe Brouzet, and Mark Peterzell (Oct. 2013). “Dynamics of ice mass deformation: Linking processes to rheology, texture, and microstructure.” In: *Geochemistry, Geophysics, Geosystems* 14.10, pp. 4185–4194. ISSN: 1525-2027. DOI: [10.1002/ggge.20246](https://doi.org/10.1002/ggge.20246). URL: <https://doi.org/10.1002/ggge.20246> (visited on 01/17/2020).

Pimienta, Pierre and Paul Duval (Jan. 1987). “Mechanical behavior of anisotropic polar ice.” In: *The Physical Basis of Ice Sheet Modelling* 170.

Placidi, Luca (Oct. 2005). “Thermodynamically Consistent Formulation of Induced Anisotropy in Polar Ice Accounting for Grain Rotation, Grain-size Evolution and Recrystallization.” PhD Thesis. Darmstadt: Technische Universität. URL: <http://tuprints.ulb.tu-darmstadt.de/614/>.

Placidi, Luca, Ralf Greve, Hakime Seddik, and Sérgio H. Faria (Mar. 2010). “Continuum-mechanical, Anisotropic Flow model for polar ice masses, based on an anisotropic Flow Enhancement factor.” In: *Continuum Mechanics and Thermodynamics* 22.3, pp. 221–237. ISSN: 1432-0959. DOI: [10.1007/s00161-009-0126-0](https://doi.org/10.1007/s00161-009-0126-0). URL: <https://doi.org/10.1007/s00161-009-0126-0>.

Prior-Jones, Michael R. et al. (2021). “Cryoegg: development and field trials of a wireless subglacial probe for deep, fast-moving ice.” In: *Journal of Glaciology*. Edition: 2021/03/09 Publisher: Cambridge University Press, pp. 1–14. ISSN: 0022-1430. DOI: [10.1017/jog.2021.16](https://doi.org/10.1017/jog.2021.16).

Qi, C., D. J. Prior, L. Craw, S. Fan, M.-G. Llorens, A. Griera, M. Negrini, P. D. Bons, and D. L. Goldsby (Feb. 2019). “Crystallographic preferred orientations of ice deformed in direct-shear experiments at low temperatures.” In: *The Cryosphere* 13.1, pp. 351–371. ISSN: 1994-0424. DOI: [10.5194/tc-13-351-2019](https://doi.org/10.5194/tc-13-351-2019). URL: <https://www.the-cryosphere.net/13/351/2019/>.

Qi, Chao, David L. Goldsby, and David J. Prior (Aug. 2017). “The down-stress transition from cluster to cone fabrics in experimentally deformed ice.” In: *Earth and Planetary Science Letters* 471, pp. 136–147. ISSN: 0012-821X. DOI: [10.1016/j.epsl.2017.05.008](https://doi.org/10.1016/j.epsl.2017.05.008). URL: <http://www.sciencedirect.com/science/article/pii/S0012821X17302625>.

Richards, Daniel H. M., Samuel S. Pegler, and Sandra Piazolo (Apr. 2021a). “Ice fabrics in natural flows: beyond pure and simple shear.”

- In: *The Cryosphere Discuss.* 2021. Publisher: Copernicus Publications, pp. 1–26. ISSN: 1994-0440. DOI: [10.5194/tc-2021-118](https://doi.org/10.5194/tc-2021-118). URL: <https://tc.copernicus.org/preprints/tc-2021-118/>.
- Richards, Daniel H. M., Samuel S. Pegler, Sandra Piazzolo, and Oliver G. Harlen (Feb. 2021b). “The evolution of ice fabrics: A continuum modelling approach validated against laboratory experiments.” In: *Earth and Planetary Science Letters* 556, p. 116718. ISSN: 0012-821X. DOI: [10.1016/j.epsl.2020.116718](https://doi.org/10.1016/j.epsl.2020.116718). URL: <http://www.sciencedirect.com/science/article/pii/S0012821X20306622>.
- Sachs, G. (1929). “Zur Ableitung einer Fließbedingung.” In: *Mitteilungen der deutschen Materialprüfungsanstalten*. Berlin, Heidelberg: Springer Berlin Heidelberg, pp. 94–97. ISBN: 978-3-642-92045-5. DOI: [10.1007/978-3-642-92045-5_12](https://doi.org/10.1007/978-3-642-92045-5_12). URL: https://doi.org/10.1007/978-3-642-92045-5_12.
- Schmid, S. M. and M. Casey (1986). “Complete Fabric Analysis of Some Commonly Observed Quartz C-Axis Patterns.” In: *Mineral and Rock Deformation*. American Geophysical Union (AGU), pp. 263–286. ISBN: 978-1-118-66435-3. URL: <https://agupubs.onlinelibrary.wiley.com/doi/abs/10.1029/GM036p0263>.
- Schytt, Valter (1958). “Snow and ice studies in Antarctica.” eng. In: *Norwegian-British-Swedish antarctic expedition, 1949-52. Scientific results* 4.A-C. Number Of Volumes: Vol. 4. A-C Place: Oslo Publisher: Norsk Polarsinstitutt, S. 9–148, 3 pl.–bl., 6, 8 pl.–s., 1 diagr.–bl. URL: <http://urn.kb.se/resolve?urn=urn:nbn:se:diva-75505> (visited on 04/20/2012).
- Seddik, H., R. Greve, T. Zwinger, and L. Placidi (2011). “A full Stokes ice flow model for the vicinity of Dome Fuji, Antarctica, with induced anisotropy and fabric evolution.” In: *The Cryosphere* 5.2, pp. 495–508. DOI: [10.5194/tc-5-495-2011](https://doi.org/10.5194/tc-5-495-2011). URL: <https://www.the-cryosphere.net/5/495/2011/>.
- Seddik, Hakime, Ralf Greve, Luca Placidi, Ilka Hamann, and Olivier Gagliardini (2008). “Application of a continuum-mechanical model for the flow of anisotropic polar ice to the EDML core, Antarctica.” In: *Journal of Glaciology* 54.187, pp. 631–642. ISSN: 0022-1430. DOI: [10.3189/002214308786570755](https://doi.org/10.3189/002214308786570755).
- Shepherd, Andrew et al. (June 2018). “Mass balance of the Antarctic Ice Sheet from 1992 to 2017.” In: *Nature* 558.7709, pp. 219–222. ISSN: 1476-4687. DOI: [10.1038/s41586-018-0179-y](https://doi.org/10.1038/s41586-018-0179-y). URL: <https://doi.org/10.1038/s41586-018-0179-y>.

- Stoll, Nicolas (2019). "A first glimpse into the EGRIP ice core: An analysis of the influence of deformation and recrystallisation on fabric and microstructures of the Northeast Greenland Ice Stream." PhD thesis. Bremen: University of Bremen.
- Ten Grotenhuis, Saskia M., Sandra Piazzolo, T. Pakula, Cees W. Passchier, and Paul D. Bons (May 2002). "Are polymers suitable rock analogs?" In: *Tectonophysics* 350.1, pp. 35–47. ISSN: 0040-1951. DOI: [10.1016/S0040-1951\(02\)00080-X](https://doi.org/10.1016/S0040-1951(02)00080-X). URL: <https://www.sciencedirect.com/science/article/pii/S004019510200080X>.
- Thorsteinsson, Thorsteinn, Josef Kipfstuhl, and Heinz Miller (Nov. 1997). "Textures and fabrics in the GRIP ice core." In: *Journal of Geophysical Research: Oceans* 102.C12. Publisher: John Wiley & Sons, Ltd, pp. 26583–26599. ISSN: 0148-0227. DOI: [10.1029/97JC00161](https://doi.org/10.1029/97JC00161). URL: <https://doi.org/10.1029/97JC00161> (visited on 09/14/2020).
- Tikoff, Basil and Haakon Fossen (Dec. 1995). "The limitations of three-dimensional kinematic vorticity analysis." In: *Journal of Structural Geology* 17.12, pp. 1771–1784. ISSN: 0191-8141. DOI: [10.1016/0191-8141\(95\)00069-P](https://doi.org/10.1016/0191-8141(95)00069-P). URL: <http://www.sciencedirect.com/science/article/pii/019181419500069P>.
- Tommasi, Andréa, Mickael Knoll, Alain Vauchez, Javier W. Signorelli, Catherine Thoraval, and Roland Logé (June 2009). "Structural reactivation in plate tectonics controlled by olivine crystal anisotropy." In: *Nature Geoscience* 2.6, pp. 423–427. ISSN: 1752-0908. DOI: [10.1038/ngeo528](https://doi.org/10.1038/ngeo528). URL: <https://doi.org/10.1038/ngeo528>.
- Treverrow, Adam, Roland C. Warner, William F. Budd, and Mike Craven (2010). "Meteoric and marine ice crystal orientation fabrics from the Amery Ice Shelf, East Antarctica." In: *Journal of Glaciology* 56.199, pp. 877–890. ISSN: 1727-5652. DOI: [10.3189/002214310794457353](https://doi.org/10.3189/002214310794457353). URL: <https://www.cambridge.org/core/article/meteoric-and-marine-ice-crystal-orientation-fabrics-from-the-amery-ice-shelf-east-antarctica/65BE624208F39BEAF47F947520B45DAA>.
- Van der Veen, C.J. and I.M. Whillans (Jan. 1994). "Development of fabric in ice." In: *Cold Regions Science and Technology* 22.2, pp. 171–195. ISSN: 0165-232X. DOI: [10.1016/0165-232X\(94\)90027-2](https://doi.org/10.1016/0165-232X(94)90027-2). URL: <http://www.sciencedirect.com/science/article/pii/0165232X94900272>.
- Vaughan, M. J., D. J. Prior, M. Jefferd, N. Brantut, T. M. Mitchell, and M. Seidemann (Sept. 2017). "Insights into anisotropy development and weakening of ice from in situ P wave velocity monitoring during laboratory creep." In: *Journal of Geophysical Research: Solid Earth* 122.9,

- pp. 7076–7089. ISSN: 2169-9313. DOI: [10.1002/2017JB013964](https://doi.org/10.1002/2017JB013964). URL: <https://doi.org/10.1002/2017JB013964> (visited on 01/28/2020).
- Weertman, Johannes and Julia R. Weertman (1992). *Elementary Dislocation Theory*. New York: Oxford University Press. ISBN: 978-0-19-506900-6.
- Westhoff, Julien, Nicolas Stoll, Steven Franke, Ilka Weikusat, Paul Bons, Johanna Kerch, Daniela Jansen, Sepp Kipfstuhl, and Dorthe Dahl-Jensen (2020). “A stratigraphy-based method for reconstructing ice core orientation.” In: *Annals of Glaciology*. Edition: 2020/11/11 Publisher: Cambridge University Press, pp. 1–12. ISSN: 0260-3055. DOI: [10.1017/aog.2020.76](https://doi.org/10.1017/aog.2020.76).
- Wilson, Christopher J. L. (Jan. 2000). “Experimental work on the effect of pre-existing anisotropy on fabric development in glaciers.” In: *Geological Society, London, Special Publications* 176.1, p. 97. DOI: [10.1144/GSL.SP.2000.176.01.08](https://doi.org/10.1144/GSL.SP.2000.176.01.08). URL: <http://sp.lyellcollection.org/content/176/1/97.abstract>.
- Wilson, Christopher J.L. and Mark Peternell (2012). “Ice deformed in compression and simple shear: control of temperature and initial fabric.” In: *Journal of Glaciology* 58.207, pp. 11–22. ISSN: 0022-1430. DOI: [10.3189/2012JogG11J065](https://doi.org/10.3189/2012JogG11J065).
- Wilson, Christopher, Nicholas Hunter, Vladimir Luzin, Mark Peternell, and Sandra Piazzolo (2019). “The influence of strain rate and presence of dispersed second phases on the deformation behaviour of polycrystalline D₂O ice.” In: *Journal of Glaciology* 65.249, pp. 101–122. ISSN: 0022-1430. DOI: [10.1017/jog.2018.100](https://doi.org/10.1017/jog.2018.100). URL: <https://www.cambridge.org/core/article/influence-of-strain-rate-and-presence-of-dispersed-second-phases-on-the-deformation-behaviour-of-polycrystalline-d2o-ice/9B203C0528AB0A658E3760D3FA94B663>.
- Wilson, Christopher, Mark Peternell, S. Piazzolo, and Vladimir Luzin (Apr. 2014). “Microstructure and fabric development in ice: Lessons learned from in situ experiments and implications for understanding rock evolution.” In: *Journal of Structural Geology* 61, pp. 50–77. DOI: [10.1016/j.jsg.2013.05.006](https://doi.org/10.1016/j.jsg.2013.05.006).
- Winkelmann, R., M. A. Martin, M. Haseloff, T. Albrecht, E. Bueler, C. Khroulev, and A. Levermann (2011). “The Potsdam Parallel Ice Sheet Model (PISM-PIK) – Part 1: Model description.” In: *The Cryosphere* 5.3, pp. 715–726. DOI: [10.5194/tc-5-715-2011](https://doi.org/10.5194/tc-5-715-2011). URL: <https://www.the-cryosphere.net/5/715/2011/>.

Zhang, Y., B. E. Hobbs, and M. W. Jessell (Sept. 1994). "The effect of grain-boundary sliding on fabric development in polycrystalline aggregates." In: *Journal of Structural Geology* 16, pp. 1315–1325. ISSN: 0191-8141. DOI: [10.1016/0191-8141\(94\)90072-8](https://doi.org/10.1016/0191-8141(94)90072-8). URL: <https://ui.adsabs.harvard.edu/abs/1994JSG....16.1315Z>.

Daniel Harry Mark Richards

Modelling ice fabric evolution and its effect on viscous anisotropy